



Universität
zu Köln

Characterization of Segmented Large Volume, High Purity Germanium Detectors



Bart Bruyneel
Institut für Kernphysik, Köln

Characterization of Segmented Large Volume, High Purity Germanium Detectors

Inaugural-Dissertation
zur
Erlangung des Doktorgrades
der Mathematisch-Naturwissenschaftlichen Fakultät
der Universität zu Köln

vorgelegt von
Bart Bruyneel
aus Geraardsbergen, Belgien

Köln 2006

Berichterstatter:

Prof. Dr. Peter Reiter
Prof. Dr. Jan Jolie

Tag der letzten mündlichen Prüfung: Juni 2006

Abstract

γ -ray tracking in future HPGe arrays like AGATA will rely on pulse shape analysis (PSA) of multiple γ -interactions. For this purpose, a simple and fast procedure was developed which enabled the first full characterization of a segmented large volume HPGe detector.

An analytical model for the hole mobility in a Ge crystal lattice was developed to describe the hole drift anisotropy with experimental velocity values along the crystal axis as parameters. The new model is based on the drifted Maxwellian hole distribution in Ge. It is verified by reproducing successfully experimental longitudinal hole anisotropy data. A comparison between electron and hole mobility shows large differences for the longitudinal and tangential velocity anisotropy as a function of the electrical field orientation.

Measurements on a 12 fold segmented, n-type, large volume, irregular shaped HPGe detector were performed in order to determine the parameters of anisotropic mobility for electrons and holes as charge carriers created by γ -ray interactions. To characterize the electron mobility the complete outer detector surface was scanned in small steps employing photopeak interactions at 60 keV. A precise measurement of the hole drift anisotropy was performed with 356 keV rays. The drift velocity anisotropy and crystal geometry cause considerable rise time differences in pulse shapes depending on the position of the spatial charge carrier creation. Pulse shapes of direct and transient signals are reproduced by weighting potential calculations with high precision. The measured angular dependence of rise times is caused by the anisotropic mobility, crystal geometry, changing field strength and space charge effects. Preamplified signals were processed employing digital spectroscopy electronics. Response functions, crosstalk contributions and averaging procedures were taken into account implying novel methods due to the segmentation of the Ge-crystal and the digital electronics. The results are relevant for the future γ -ray tracking detectors where high precision of position information of single γ -ray interactions is required.

The high accuracy in simulation enabled very high position resolution using PSA. The first application of this technique in a real experiment aimed at the correction for crystal bending imperfections in a Bragg-spectrometer. A position resolution of $\sigma_x = 1.4$ mm was achieved with 184 keV γ -rays employing the fully characterized detector. By careful characterization of the electronic noise, this result is expected to improve further upon use of optimized filters.

Zusammenfassung

In zukünftigen HPGe-Anordnungen wie AGATA wird die Spurenanalyse von γ -Strahlen auf der Pulsformanalyse für Mehrfachwechselwirkungen von γ -Quanten beruhen. Aus diesem Grunde wurde ein einfaches, zugleich aber schnelles Verfahren entwickelt, das erstmalig eine vollständige Charakterisierung segmentierter, großvolumiger HPGe-Detektoren ermöglicht.

Es wurde ein analytisches Modell für die Löcherbeweglichkeit in einem Germaniumkristall entwickelt, um die Anisotropie der Löcherdrift mit experimentellen Geschwindigkeitswerten entlang der Kristallachse als Parametern zu beschreiben. Dieses neue Modell beruht auf der verschobenen Maxwellverteilung der Löcher im Germanium. Es konnte durch die erfolgreiche Reproduktion von experimentellen Ergebnissen der longitudinalen Löcheranisotropie verifiziert werden. Ein Vergleich der Elektronen- mit der Löcherbeweglichkeit zeigt große Unterschiede für longitudinale und tangential Geschwindigkeitsanisotropien als Funktion der Orientierung des elektrischen Feldes.

Es wurden Messungen an einem 12-fach segmentierten, großvolumigen und ungleichmäßig geformten n-Typ HPGe-Detektor durchgeführt, um die Parameter für anisotrope Beweglichkeit für Elektronen und Löcher zu bestimmen. Um die Elektronenbeweglichkeit zu charakterisieren, wurde die gesamte äußere Oberfläche des Detektors in kleinen Schritten mit 60 keV γ -Quanten gescannt, die durch den Photoeffekt wechselwirken. Eine präzise Messung der Löcherdriftanisotropie wurde mit 356 keV-Quanten durchgeführt. Die Anisotropie in der Driftgeschwindigkeit und die Kristallgeometrie verursachen beträchtliche Unterschiede der Anstiegszeiten in der Pulsform abhängig von der Position der räumlichen Ladungsträgerbildung. Die Pulsform direkter und transienter Signale wird mit Hilfe von Berechnungen gewichteter Potentiale sehr präzise wiedergegeben. Die gemessene Winkelverteilung der Anstiegszeiten wird durch anisotrope Mobilität, Kristallgeometrie, wechselnde Feldstärken und Raumladungseffekte hervorgerufen.

Die Vorverstärkersignale wurden mit digitaler Elektronik weiterverarbeitet. Übertragungsfunktionen, Crosstalk-Verteilungen und Mittelungsprozeduren wurden berücksichtigt, indem neuartige Methoden aufgrund der Segmentierung des Germanium-Kristalls und digitaler Elektronik einbezogen wurden. Diese Ergebnisse sind für zukünftige Detektoren zur Spurenanalyse der γ -Strahlen relevant, in denen eine sehr genaue Ortsinformation für einzelne γ -Quantenwechselwirkungen benötigt wird.

Die hohe Genauigkeit der Simulation ermöglicht mit Hilfe der Pulsformanalyse

eine sehr gute Ortsauflösung. Das Ziel der ersten Anwendung dieses Verfahrens in einem Experiment war die Korrektur von Fehlstellen der Kristall-Krümmung in einem Bragg-Spektrometer. Am vollständig charakterisierten Detektor wurde mit γ -Quanten der Energie $E_\gamma = 184\text{ keV}$ eine Ortsauflösung von $\sigma_x = 1.4\text{ mm}$ erzielt. Sorgfältige Untersuchungen des elektronischen Rauschens lassen erwarten, dass dieses Ergebnis durch optimierte Filter noch stark verbessert werden kann.

Contents

Abstract	iv
Zusammenfassung	v
1 Introduction – Motivation	1
1.1 AGATA	1
1.1.1 The concept of AGATA	1
1.1.2 Tracking	3
1.1.3 Pulse Shape Analysis	3
1.1.4 Characterization	4
2 MINIBALL	7
2.1 Construction of a MINIBALL detector	7
2.2 The MINIBALL detector crystal	9
2.3 The MINIBALL front-end electronics	10
3 About weighting potentials	13
3.0.1 The quasi-steady state approximation	13
3.1 The Shockley-Ramo theorem	14
3.1.1 Weighting potentials for the detector	17
3.2 Pulse formation	17
3.2.1 The nature of single interaction events	17
3.3 A two-dimensional playground	19
3.3.1 Coaxial weighting potentials	19
3.3.2 Locating the electrons	20
3.3.3 Limitations of the method	22
4 The detector-preamplifier connection	24
4.1 Small signal equivalent for the detector	24
4.2 The detector-preamplifier interface	26
4.3 General solution	27
4.4 The transfer function	29
4.5 Back in time(-domain)	29

5	Response Functions	32
5.1	The Analog Front-end Response	32
5.2	Averaging routine	34
5.3	Crosstalk	35
5.3.1	Proportional Crosstalk	36
5.3.2	Derivative Crosstalk	37
6	Introduction to Mobilities	43
6.1	A Poisson Solver	43
6.2	Modeling the Mobility	44
7	Electron Mobility Model	50
7.1	Layout of the model	50
7.2	Parametrization of the model	51
8	The Hole Mobility Model	55
8.1	Layout of the model	55
8.2	Theoretical results on the hole model	57
8.3	A practical approximation	59
8.4	Comparison with the electron mobility model	61
9	Electron Mobility Results	66
9.1	The Measurement	66
9.2	Rise Time Fit Functions	67
9.3	Rise Time Profiles	68
9.4	Electron Mobility Parameters	71
9.5	Timing Measurement	75
10	Hole Mobility Results	80
10.1	The Measurement	80
10.2	Rise Time Profiles	81
10.3	Anisotropy Enhanced Space Charge Effects	84
11	Pulse Shape Analysis	88
11.1	Steepest Slope & Asymmetry	88
11.2	Doppler correction with MINIBALL	89
11.3	Future methods	90
11.4	A simple PSA method	91
11.4.1	Single interactions	91
11.4.2	Multiple interactions	93
12	Gamma ray diffraction at GAMS5	95
12.1	GAMS5	95
12.1.1	About the spectrometer	95
12.1.2	Setup of the experiment	96

12.2	Obtained position resolution	96
12.2.1	Noise Analysis	98
12.2.2	Image of a single slit aperture	100
12.2.3	Analysis of the observed collimator line width	100
12.3	Results	104
13	Conclusion	107
A	Position Resolution	109
A.1	The Multivariate Normal Distribution	109
A.1.1	Shape of the distribution	109
A.1.2	Parameter Estimation	109
A.2	Measured noise properties	110
A.3	General Least Square Estimation	112
A.4	Position sensitivity	114
A.5	Improved Figure of Merit	114
	Bibliography	124
	Thank you!	125

List of Figures

1.1	AGATA: The 4π , 180 detector configuration.	2
1.2	World map representation to illustrate the tracking concept. .	4
2.1	Layout of a modern MINIBALL detector.	8
2.2	A 12-fold segmented encapsulated MINIBALL crystal.	9
2.3	Measures of the MINIBALL detector geometry.	9
2.4	MINIBALL electronics: FET motherboards and preamplifier.	11
2.5	Overview of the front-end electronics.	12
3.1	Weighting potential for a segment.	20
3.2	An illustration of the procedure to trace electrons.	21
3.3	The electron path inside the germanium crystal.	23
4.1	The small signal equivalent scheme of a segmented detector. .	25
4.2	A schematic layout of detector and preamplifiers.	27
4.3	AC equivalent of the detector.	28
4.4	Comparison of the time dependence of crosstalk.	30
4.5	Crosstalk in segments as function of the decoupling capacity.	31
5.1	Response functions: Theory versus measurement.	33
5.2	Comparison of raw 60 keV data with its average.	34
5.3	Empirical rule on observed crosstalk.	36
5.4	Measured core-to-segment proportional crosstalk.	38
5.5	Additional segment-to-segment proportional crosstalk.	38
5.6	Illustration of a novel method to extract crosstalk.	39
5.7	The crosstalk detection method in action.	40
5.8	Crosstalk correction checksum.	41
5.9	Comparison between measured response functions.	42
6.2	The diamond lattice structure of germanium.	44
6.1	Electrical field and potential in the detector.	48
6.3	The germanium band structure.	49
7.1	The conduction band minima.	50
7.2	Conduction band valley population versus impurity.	53

7.3	The angular dependence of the electron velocity.	54
8.1	The maximum in the heavy hole valence band.	55
8.2	Λ and Ω as function of k_0	61
8.3	Verification of the hole mobility model.	62
8.4	k_0 as function of the field strength.	63
8.5	Angular dependence of the hole velocity.	64
8.6	Tangential anisotropy: Holes versus electrons.	65
9.1	Positions measured for the electron mobility characterization.	66
9.2	Origin of the characteristic rise time profiles.	68
9.3	10% – 90% rise times of the electron mobility.	70
9.4	Core partial rise time profiles.	72
9.5	Segment partial rise time profiles.	73
9.6	Measured versus simulated electron charge pulses.	76
9.7	Deviation between simulation and experiment.	76
9.8	Relative time delays of hit segments.	77
9.9	Depth dependency of the delays.	78
9.10	Angular dependency of the delays.	79
10.1	Collimator setup for hole mobility characterization.	81
10.2	Rise time measurements at 7 cm depth.	82
10.3	Measured versus simulated hole charge pulses.	83
10.4	Rise time measurements at 2.1 cm depth.	85
10.5	Simulated hole trajectories at 2.1 cm depth.	86
10.6	Simulated hole trajectories at 2.2 cm depth.	87
10.7	Simulated hole current density at 2.2 cm depth.	87
11.1	Position reconstruction using steepest slope and asymmetry.	89
11.2	A simple grid search method.	92
11.3	Illustration of a multidimensional minimum search.	93
12.1	Schematic overview of the setup at GAMS5.	97
12.2	Typical core signal acquired in the experiment.	98
12.3	Noise levels measured at ILL.	99
12.4	A detector image of a single slit.	101
12.5	The single Compton scattered position distribution.	102
12.6	Probability for finding the energy-weighted barycenter.	103
12.7	Analysis of the obtained position resolution.	105
12.8	Correction of the diffraction crystals surface.	106
A.1	A measured covariance matrix	111

Chapter 1

Introduction – Motivation

Since germanium detectors became available in the 1960's, they have taken in a key position in the field of nuclear spectroscopy. These detectors combine excellent energy resolution with good timing resolution in the energy range relevant for nuclear spectroscopy. The present state-of-the-art is represented by the EUROBALL and Gammasphere spectrometers. This role will be taken over in the future by the Advanced GAMMA-ray Tracking Array (AGATA) [1] and the Gamma Ray Energy Tracking Array GRETA [2] which are now under development. The AGATA project is supported by over 40 European institutes and is developed – to some extent – in collaboration with the American GRETA project [3, 4]. The work presented here deals with the development of highly segmented, large volume HPGe detectors which will be employed to localize individual γ -ray interactions as basic information for a γ -ray tracking spectrometer. In one word, it deals with the characterization problem of such detectors. The motivation for the work is shortly introduced in this chapter.

1.1 AGATA

1.1.1 The concept of AGATA

The AGATA spectrometer is mainly intended for high-resolution γ -ray spectroscopy with exotic beams at future European accelerator facilities providing heavy ion beams of unstable rare isotopes. The project is aiming for the construction of the first real 4π gamma-ray spectrometer solely built from germanium detectors. In its final stage, AGATA will comprise 180 highly segmented High-Purity Germanium (HPGe) detectors, which will be concentrated around the target providing optimal conditions for a wide range of nuclear structure experiments (see Fig. 1.1). Coupled to a high intensity radioactive beam facility, this project will enable the investigation of the nuclear landscape at its very limits.

The design of the AGATA spectrometer requires the optimization of

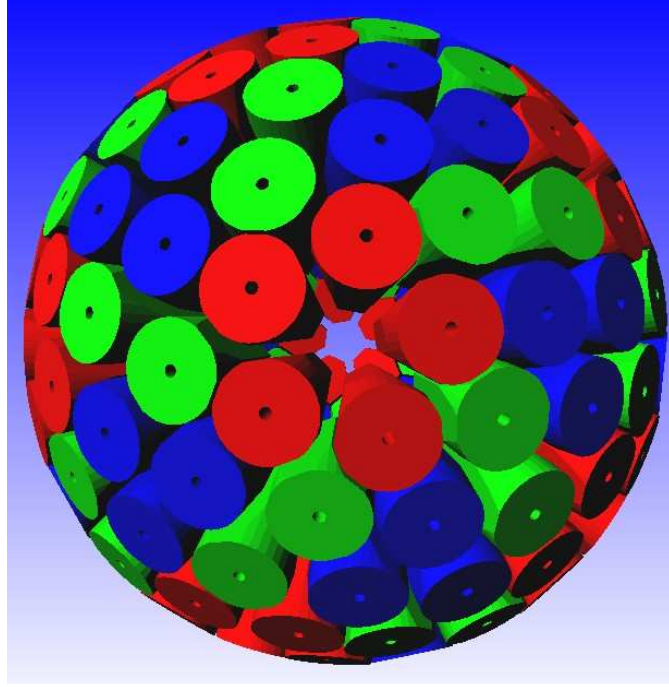


Figure 1.1: AGATA: The 4π , 180 detector configuration. The germanium shell is covered with three types of semi-hexagonal, asymmetric shaped diodes (colored red, green and blue in the picture). each cluster detector will contain one diode of each type of asymmetry (Picture taken from [5]).

several, partially conflicting properties simultaneously: A 4π , 9 cm thick germanium shell will provide the highest photopeak efficiency for energies up to 10 MeV. This will enable to study the weakest exotic reaction channels. Such exotic beams are often contaminated by more abundant but less exotic elements and therefore require high count rate capability and photo peak efficiency.

A high peak-to-total ratio (the ratio between the photopeak efficiency and the total interaction efficiency) is essential for any spectrometer in order to provide high quality spectra. Presently, the most powerful spectrometers, EUROBALL [6] and Gammasphere [7], rely on anti-Compton shields to achieve a high peak-to-total ratio. This always presents a trade-off between efficiency and acceptance.

To be able to resolve high multiplicity gamma ray cascades, a large segmentation of the germanium shell is necessary in order to minimize summing effects. High angular segmentation is also required when dealing with fast radioactive beams ($v/c \geq 10\%$) as a good angular resolution in the first interaction of Doppler broadened γ -quanta is mandatory. This enables Doppler correction which restores the line width and hence the spectrometers resolving power. On the other hand, a high fragmentation of the germanium

shell combined with high gamma multiplicities increases the identification problem due to Compton events scattered into different segments.

1.1.2 Tracking

The key in solving these problems lies in the introduction of a new concept called gamma ray tracking. This technique will exploit fully the high position sensitivity of these detector arrays and is expected to improve substantially on the resolving power. Especially when high multiplicity γ -ray cascades are observed, where improvements of more than two orders of magnitude over existing detector arrays are estimated (the probability of detecting a multiplicity n event scales with the n -th power of the efficiency).

The method will evaluate the spatial correlation between the time coincident γ interactions in the germanium shell using the Compton relation and taking into account the possibility of pair production. This will allow to reconstruct the path of the emitted γ -rays. The peak-to-total ratio and the γ multiplicity therefore are depending on the correct sorting of the individual observed γ interactions into clusters. This idea is illustrated in Fig. 1.2. Each cluster should finally contain all interaction positions caused by an individual γ -ray track. The credibility of a proposed cluster is maximized by an optimization of the probability assigned with the anticipated γ -ray track. Several such tracking schemes have been developed [8, 9], and the realization of fast online tracking algorithms is still an ongoing subject of research.

Doppler correction depends on the right assignment of the first interaction position in each cluster (Marked blue in Fig. 1.2). This problem is inferior to the solution of the full γ -ray track and hence it is implicitly solved by the latter.

1.1.3 Pulse Shape Analysis

The spatial localization of the interaction positions will rely completely on detailed pulse shape analysis. In order to achieve a good tracking efficiency, position information with an accuracy of a few millimeter is required.

The position information will be obtained from raw detector pulses by comparing the pulse shapes to simulated detector responses. This requires a detailed library of simulated traces including positions mapping the whole detector volume. Such method is described in detail in chapter 11.

The final position resolution obtainable through pulse shape analysis will be restricted by the realism of the simulated library. Therefore, a detailed understanding of the principles behind the origin of the detectors pulse shape is crucial.

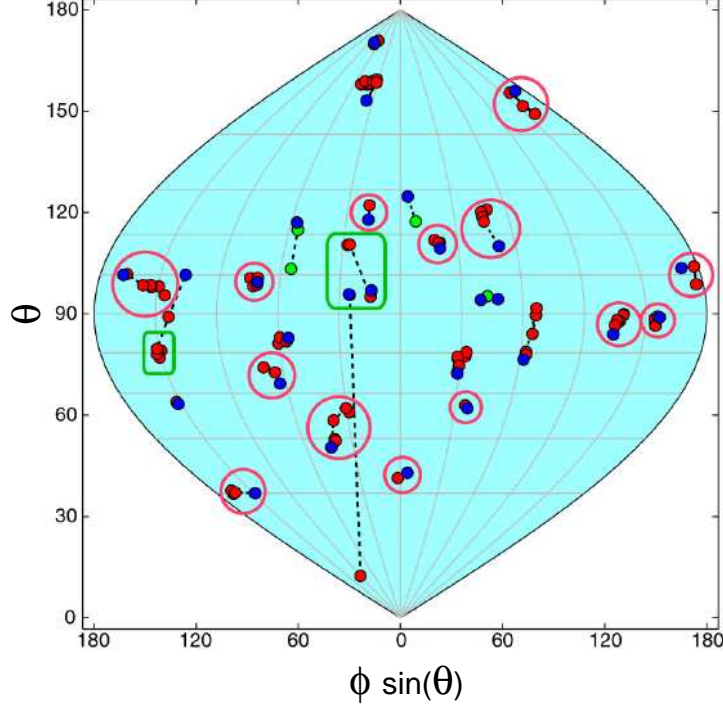


Figure 1.2: World map representation of an $E_\gamma = 1.0$ MeV, multiplicity 30 event for illustration of the tracking concept. Correct reconstructed γ -rays are shown as red clusters. Wrongly reconstructed γ -rays are represented as green clusters. The picture was taken from [10].

1.1.4 Characterization

Along with the demand for precise position information comes the complexity in preparation of these newly developed detector types. The fact that from these detectors also position information is demanded invokes that each detector, besides the traditional energy calibration, now also needs a calibration for the position space. Consequently, detailed characterization of the detector is mandatory. Unfortunately, no simple position calibration procedure is available yet.

The characterization of a large volume segmented Ge detector should lead to the detailed knowledge on how the detector and the acquisition system will respond to an interaction at any point in the detector. One way to obtain the needed detector single interaction response information is based on a Compton scattering technique [11, 12, 13, 14, 15]. This method requires heavy collimation and coincidence detection of rare Compton scattering processes. Therefore the scanning rate becomes extremely slow (up to a few days per point) for interactions deep inside the detector volume. Hence,

a more time-efficient characterization technique was developed within this project which relies on procedures to extract realistic input for detector response simulation. A short introduction will be given on how the detector response can be calculated with the purpose to identify which parameters are needed for a detailed detector response simulation.

For a good agreement between a detector's calculated and its true experimental response, a principal requirement is a detailed knowledge on the amount of mirror charge that is induced in a specific electrode due to a charge present at any point inside the detector. This question is answered by the notion of the *weighting potential* in the Shockley-Ramo theorem, which is extensively described in chapter 3.

Secondly, the dynamics of the charges created in the detector has to be understood and exact data on the *mobility* of the electrons and hole clouds on their path towards their collecting electrode are mandatory. This allows to simulate the electron and hole paths in the detector as function of the time elapsed during their collection process. The resulting induced charge in a specific electrode is calculated by evaluating the corresponding weighting potential at the time dependent position of electrons and holes.

Finally, the analog frontend electronic circuitry deforms the signals produced in the charge collection process. These *response functions* have to be determined. The calculated charge signals are convoluted with the appropriate response functions. Also crosstalk has to be taken into account. A special technique for crosstalk determination in segmented detectors was developed and applied in chapter 5.

A detector becomes fully characterized by specifying the ingredients needed for a detailed detector response simulation: charge carrier mobilities and the behavior of crosstalk and response functions.

In this way, one obtains a pragmatic definition for the term *characterization*. The amount of parameters that need to be specified for a full characterization can become quite elaborate. This set of parameters can be sorted into two categories. One category of parameters characterizes the detector crystal. It comprises specification of the crystal orientation, space charge, electron mobility and hole mobility. The second category characterizes the influence of the analog front end electronics. It includes response functions and crosstalk.

Theoretically both sets of parameters are independent, however in reality information on the mobility cannot be obtained without a proper knowledge on the influence of the measuring circuitry. A good implementation in the simulation of the properties of the analog front-end electronics is therefore essential to derive meaningful conclusions on the detector crystal properties.

The new developed techniques regarding mobility and crosstalk detection described in this work made it possible that for the first time a full characterization of a segmented HPGe detector was established. All data for a full characterization was experimentally determined for a 12 fold segmented MINIBALL detector. In the near future, these procedures will be applied to the first AGATA detectors now becoming available.

Chapter 2

MINIBALL

The precision and effectiveness of the new characterization method was developed for and is demonstrated on a 12-fold segmented HPGe MINIBALL detector [16, 17] because no AGATA detector existed yet at the time. It goes without saying that any characterization procedure developed in this work can be equally well applied to 36-fold segmented AGATA detectors.

2.1 Construction of a MINIBALL detector

The MINIBALL detector array is optimized for low γ -multiplicity experiments. It consists of six-fold angular segmented Ge detectors which allow for the localization of the direction of the emitted γ -rays.

The mechanical construction of the detector is shown in Fig. 2.1. The figure shows a modern MINIBALL detector as it was used in the characterization procedure. A single encapsulated germanium crystal was mounted on a cold finger which brings it in thermal contact with the liquid nitrogen dewar. The dewar is constructed to maintain the Ge detector operational for 12 hours. The temperature of the crystal is monitored over a PT100 [18].

The good vacuum (in the lower 10^{-6} mbar) inside the detector construction guarantees the thermal isolation of the detector crystal from the outer detector mantle at room temperature [19]. The vacuum is maintained over a long period using three molecular getters. These chemical getter materials trap all restgas atoms when cooled at liquid nitrogen. A carbon getter is build into the dewar itself. Zeolite is used between dewar and cold finger. Finally, palladium is used as a hydrogen catcher. For maintenance, a Cad-dock (a power resistor) can be used to accelerate the warming up of the detector, or to heat out the cryostat assembly.

Care is taken to minimize the thermal contact of the mechanical support of the cold inner part with the outer part at room temperature. The cold finger is centered using triangular shaped plastic parts at both ends of the

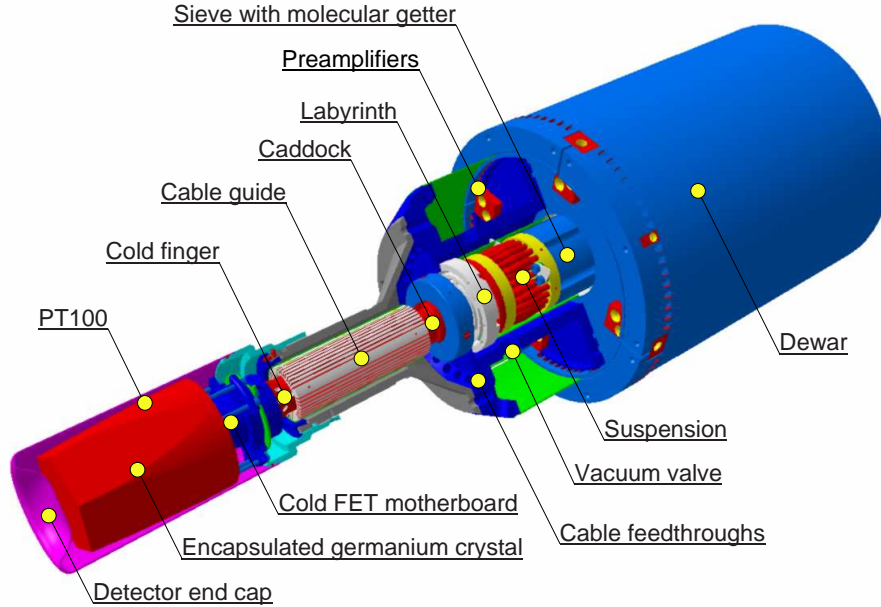


Figure 2.1: Layout of a modern MINIBALL detector. See text for description.

cold finger and a labyrinth-shaped connection made out of PTFCE¹. This special teflon material has very low thermal conductivity. The shape of this material serves two purposes. First, it elongates the connection between cold and warm and thus decreases the thermal conductivity. Secondly, it keeps the system shock resistive. The dewar is also flexibly connected with the cold finger using thick wire-like copper strands. This provides a buffer against thermal expansion of the system and decouples the detector vibrationally from the dewar and thus reduces the effect of microphonics.

The motherboard including the cold FET's (see Fig. 2.4A) is connected directly on the crystals encapsulation to decrease the signal path between detector and preamplifier. The electronic cabling (HV, ground and cold FET signals) is guided along the cold finger to the feedthroughs where the connection is made with the warm part of the preamplifiers (Fig. 2.4B). To reduce thermal conductivity, the connection with the feedthroughs is made with very thin wires. The preamplifiers are closely packed together in a separate box, electromagnetically shielded from the outside.

¹abbreviation for polytrifluorchlorethylene

2.2 The MINIBALL detector crystal

Different to the standard MINIBALL detector, the detector studied here has a six fold angular segmentation of the outer contact and a single segmentation line in depth (see Fig. 2.3). The detector thus fulfills the minimum requirement for giving full 3D information on the position of an interaction. This extra segmentation line is positioned at a depth of 26 mm, dividing the crystal's length in two unequal parts of which the smallest, the six front segments, have just halve the length in depth of their six back neighbors. The detector has inherited the semi-hexagonal cut encapsulated crystal from the Euroball detectors, which allows for close packing into cluster detectors.

A picture of a 12-fold segmented MINIBALL diode is shown in Fig. 2.2. The twelve segments are connected to 12 terminals distributed over three feedthroughs. The core electrode is connected to the central contact, which is strongly isolated as it has to withstand high voltages up to 5000 V.



Figure 2.2: Picture of a 12-fold segmented encapsulated MINIBALL crystal.

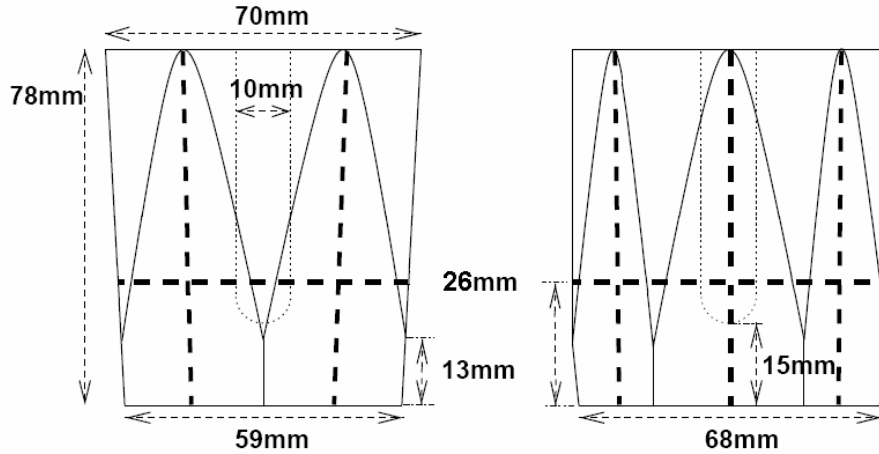


Figure 2.3: Measures of the 12-fold segmented MINIBALL diode geometry.

2.3 The MINIBALL front-end electronics

The core as well as the 12 segments are equipped with HeKo² preamplifiers [16, 20] which were specially designed for MINIBALL. The front-end of the HeKo preamps is cooled down to about -150° for optimum noise performance. The printed circuit boards (PCB) containing the cooled electronics (one FET and one RC-feed back loop pro channel) are shown in Fig. 2.4A. The coupling between detector and the cold PCB's will be described in detail in chapter 4.

The HeKo preamplifier (Fig. 2.4B) is designed with two stages. The first stage consists of a current integrator build around an operational amplifier (OpAmp) with single-ended input and an open loop gain of $2 \cdot 10^4$. Since low noise is of extreme importance here, best results up to date are still achieved building the first amplifier stage out of discrete components. This first stage is based on a cascode amplifier. Its amplification factor depends among others on the drain current through the FET, which can be adjusted with a potentiometer. The band width and consequently the rise time of this stage can be tuned with a variable capacity to prevent oscillation. This first stage realizes a charge to voltage conversion of 52 mV/MeV.

At the output of the first stage, the voltage signals have an exponential decay time τ determined by the feed back impedance: $\tau = R_{fb}C_{fb} \cong 1$ ms. In the second stage of the preamplifier, this is converted into a signal with a 50 μ s decay time which prevents pile-up. This is realized by a pole-zero cancelation network buffered between two OpAmps. The second stage only realizes a total amplification of 4 but it provides also the necessary 50 Ω output impedance and allows the DC output level to be adjusted.

A more detailed explanation on the operation of a classical preamplifier can be obtained in [21, 22]. The HeKo preamplifier, briefly described here, is treated in more detail in [23, p.141].

The twelve segment signals plus the core signal were read out using four DGF-4C ADC's [24] (see Fig. 2.5). Such modules have each 4 channels providing 12 bit precision at 40 MHz sampling rate. One module was reserved for the core signal. This module was configured as master and was triggering the other modules receiving the segment signals.

²A preamplifier originated from a collaboration between the universities Heidelberg and Köln (HeKo). More precisely, the commercially available PSC823 version build by Eurisys was used, which has a slightly worse rise time performance than the original.

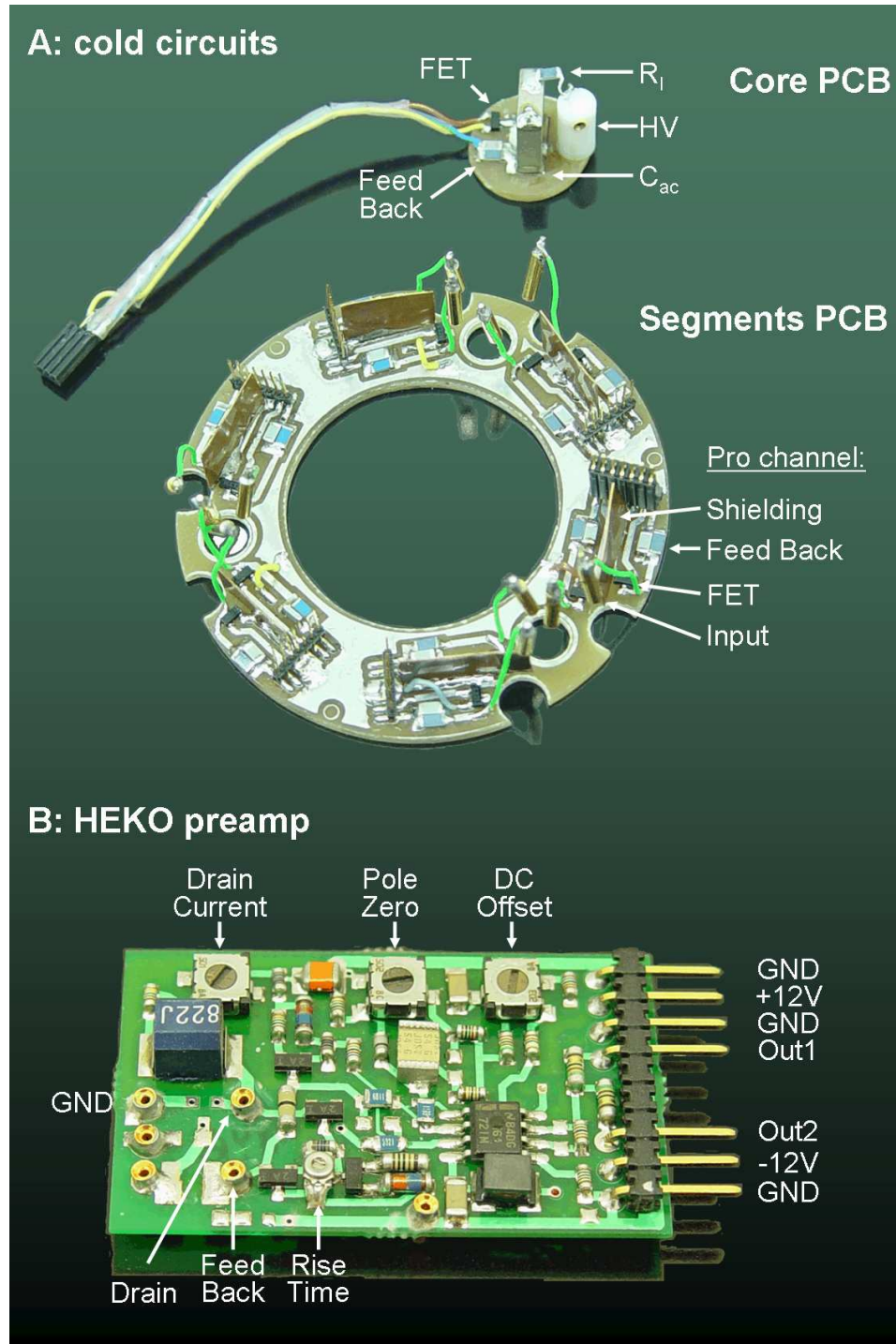


Figure 2.4: Electronics build into a MINIBALL Ge detector. A: The cold FET motherboards for core and segments. B: A one-channel MINIBALL preamplifier. Potentiometers are used to adjust individually: drain current, pole zero and DC offset. Connections for the cold PCB's (GND, Drain and Feed back) are indicated. The bandwidth can be modified by changing a variable capacity (Rise time).

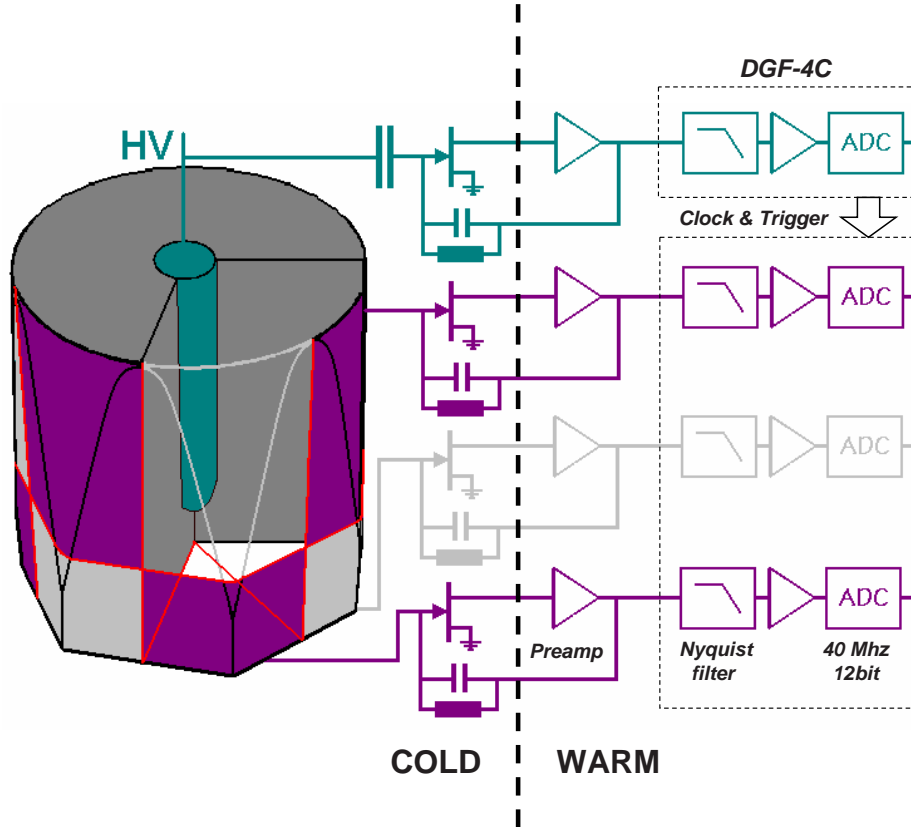


Figure 2.5: A schematic overview of the front-end electronics as used in this work to operate the 12-fold segmented MINIBALL detector. The preamplifiers are equipped with cold FET's. Their signals are digitized into 12 bit using four DGF-4C ADC's. In this process, frequencies above half the sampling frequency need to be suppressed by a Nyquist filter. All modules are operated with common clock (40 Mhz) and react upon common core triggers.

Chapter 3

About weighting potentials

In this chapter, it is described in detail how the pulses at each terminal of the segmented electrodes are related to the movement of the charge carriers inside the bulk of the detector. The nature of this problem is quite universal. In fact the theorem which Shockley [25] and Ramo [26] discovered independently, was developed to describe the behavior of vacuum tubes. In time, several extensions to the theorem were developed. Among others, it was proven [27] that the theorem still holds under the presence of space charge in the device. For a recent review on the subject, check out [28, 29, 30].

3.0.1 The quasi-steady state approximation

The problem consists in the detection of a small charge q at position $\vec{x}_0(t)$ that moves under influence of field \vec{E} , between an arrangement of electrodes with surfaces S_j , $j = 1 \dots n$ and held at fixed potentials V_j . The important question – since it is related to the sole observable quantity – is then: how much current is the movement of the q producing on a specific electrode i ? The answer to this forms the key to a correct evaluation of the observed mirror charges and makes it possible to distillate information on $\vec{x}_0(t = 0)$, which remains the leading question.

We will investigate this problem in the quasi-steady state approximation: we suppose that the movement of the charge is slow enough to assume that the momentary fields can be well approximated as being in electrostatic equilibrium. This can be easily verified by comparing the velocities involved. The speed of light in germanium is $750 \cdot 10^7$ cm/s (germanium has a refraction index of 4.0) while the mobility of electrons and holes in germanium is less or comparable to $1 \cdot 10^7$ cm/s. Further, it is assumed that the influence of the charge q on the field \vec{E} is small enough such that its motion is not influenced under the small changes in \vec{E} .

Under these approximations, we can decouple the problem: The field \vec{E} is calculated neglecting the presence of q . When the dependence of the drift

velocity of the charge q on the field strength is known, we can predict its path between the electrodes. The description of the mobility of electrons and holes as function of the field is far from trivial and will be extensively studied in chapters 6,7,8. The remaining problem, to reconstruct the time dependence of the charge signal induced on each electrode, is therefore reduced to:

Problem 3.0.1 *Find the surplus of charge that is induced in electrode i by the presence of charge q at any position \vec{x}_0 along its trajectory.*

As we only refer to this problem in the quasi-steady state approximation, we can omit here the time dependence of \vec{x}_0 .

In the specific case of our segmented detector, we have the following situation: The detector has the core electrode biased at high voltage and the segments virtually grounded such that the detector is fully depleted. The ionized impurities present at fixed positions in the germanium crystal lattice form a stationary space charge density $\rho(\vec{x})$ [31, p.369], which has a strong influence¹ on the electrical field strength. Finally, we are only interested in the image charges created by the free charge carriers q created in the bulk of the germanium material by ionizing radiation.

3.1 The Shockley-Ramo theorem

The total charge Q_i induced on an electrode i with surface S_i can be calculated by integration of the normal component of the electrical field \vec{E} outside this surface (see Gauss's law [32, p.688],[33, p.32]):

$$Q_i = \oint_{S_i} \epsilon \vec{E} \cdot d\vec{S}_i \quad (3.1)$$

in which ϵ represents the dielectric constant of the medium ($16 \cdot \epsilon_0$ for germanium).

The total field $\vec{E}(\vec{x}) = -\nabla\phi(\vec{x})$ is obtained through solution of the Poisson equation with Dirichlet boundary conditions:

$$\nabla^2\phi(\vec{x}) = -[\rho(\vec{x}) + q\delta(\vec{x} - \vec{x}_0)]/\epsilon \quad \phi|_{S_j} = V_j$$

The linearity of the Poisson equation and the applied boundary conditions allow us to separate the total potential $\phi(\vec{x})$ into the contributions from the steady state potentials $\phi_0(\vec{x})$ created by the applied voltages and the

¹In the worst case, its influence could cause that the detector is not fully depleted.

space charge and the quasi-steady state potential $\phi_q(\vec{x})$ created by the point charge at position \vec{x}_0 :

$$\begin{aligned} \phi(\vec{x}) &= \phi_0(\vec{x}) + \phi_q(\vec{x}) && \text{with} \\ \nabla^2 \phi_0(\vec{x}) &= -\rho(\vec{x})/\epsilon && \phi|_{S_j} = V_j \\ \nabla^2 \phi_q(\vec{x}) &= -q\delta(\vec{x} - \vec{x}_0)/\epsilon && \phi|_{S_j} = 0 \end{aligned} \quad (3.2)$$

The separation of potentials invokes an analogous separation of the total electrical field into the parts: $\vec{E}(\vec{x}) = \vec{E}_0(\vec{x}) + \vec{E}_q(\vec{x})$. Applying formula 3.1 then yields

$$\begin{aligned} Q_i &= Q_{0i} + Q_{qi} && \text{with} \\ Q_{0i} &= \oint_{S_i} \epsilon \vec{E}_0 \cdot d\vec{S}_i \\ Q_{qi} &= \oint_{S_i} \epsilon \vec{E}_q \cdot d\vec{S}_i \end{aligned} \quad (3.3)$$

The fractions Q_{0i} are time-independent and are related to the capacity between the electrodes. The fraction of interest is the extra charge Q_{qi} created on the electrode i by the point charge q . The quasi-steady state requires that $Q_{qi} \ll Q_{0i}$. Observe that in For. 3.2, 3.3 the potentials V_i and the space charge $\rho(\vec{x})$ do not show up. From this, we can state that:

Corollary 3.1.1 *The charges induced by charge q do not depend on the applied potentials nor on the space charge in between electrodes.*

Unfortunately the independence on space charge has been questioned in the past by several authors. Although their criticism was unjustified [34, 35], this has added to the mystification of the subject such that even in standard work on radiation detection², violations against this theorem have subsisted.

For moving charges, Gauss's law (For. 3.3) is not very useful as it would require to calculate the potential ϕ_q again when the position of q has changed. Luckily, there exist a very elegant way to work around this problem:

²In Knoll [31, p.423], a space charge dependent model for the induced charges is derived although the author is obviously aware of the correct version, see [31, Appendix D].

The Schockley-Ramo theorem 3.1.1 *The induced charge Q_{qi} on electrode i by a point charge q located at \vec{x}_0 is given by*

$$Q_{qi} = -q \cdot \psi_i(\vec{x}_0) \quad (3.4)$$

with ψ_i defined by:

$$\nabla^2 \psi_i(\vec{x}) = 0 \quad \phi|_{S_j} = \delta_{i,j} \quad (3.5)$$

The momentary current I_{qi} induced by the movement of q is:

$$I_{qi}(t) = q \vec{E}_{\psi_i}(\vec{x}_0(t)) \cdot \vec{v}(t) \quad (3.6)$$

with $\vec{v}(t)$ the momentary drift velocity of q .

ψ_i is called the *weighting potential* related to electrode i and $\vec{E}_{\psi_i} = -\nabla \psi_i$ is the corresponding *weighting field*. The advantage compared to For. 3.3 is clear: the weighting potentials need to be calculated only once. Statement 3.6 follows directly from For. 3.5 by taking the time derivative of the latter and using the chain rule: $\frac{d}{dt} = \frac{\partial}{\partial x} \frac{dx}{dt} + \frac{\partial}{\partial y} \frac{dy}{dt} + \frac{\partial}{\partial z} \frac{dz}{dt}$. An elegant way to prove For. 3.5 is by making use of Green's second identity:

Greens second identity 3.1.1 *Between two arbitrary scalar fields Φ, Ψ and for an arbitrary volume V bounded by surface S , the following identity holds:*

$$\int_V \Phi \Delta \Psi - \Psi \Delta \Phi dV = \oint_S \Phi \frac{\partial \Psi}{\partial n} - \Psi \frac{\partial \Phi}{\partial n} dA \quad (3.7)$$

Let us now take as a special case $\Phi = \phi_q$ as defined by For. 3.2 and $\Psi = \psi_i$ as defined by For. 3.5. Further select the volume V as the volume excluding any electrode interior (The volume is bounded by and includes the electrode surfaces). For this special case, we thus obtain:

$$(\Phi|_{S_j}, \Delta \Phi, \frac{\partial \Phi}{\partial n}|_{S_j}) = (0, -q\delta(\vec{x} - \vec{x}_0)/\epsilon, -\sigma_{q,j}/\epsilon) \quad (3.8)$$

$$(\Psi|_{S_j}, \Delta \Psi, \frac{\partial \Psi}{\partial n}|_{S_j}) = (\delta_{i,j}, 0, -\sigma_{i,j}/\epsilon) \quad (3.9)$$

With $\sigma_{q,j}$, $\sigma_{i,j}$ the surface charge distributions on electrode j due to the potentials ϕ_q and ψ_i , respectively. With this result, we obtain for Greens second identity:

$$\int_V \psi_i \cdot q\delta(\vec{x} - \vec{x}_0) dV = - \sum_j \oint_{S_i} \delta_{i,j} \cdot \sigma_{q,j} dA$$

Which leads immediately to statement 3.5.

3.1.1 Weighting potentials for the detector

For our detector, the twelve electrodes are fully covering the front and the side surface of the detector. The gap between segments – the segmentation line – is only about $100\ \mu\text{m}$ thick. The backside of the detector is covered with a passivated layer, which acts as an electrostatic mirror. The active volume of the detector therefore behaves as if it was fully surrounded by the segment electrodes, the core electrode and their mirrored images.

If we make the surface of this enclosed volume an equipotential surface, the resulting potential throughout the volume will be constant. The sum $\Psi = \sum_i \psi_i$ of all the weighting potentials has this property as is easily verified using eq. 3.5. Therefore, we obtain that:

Corollary 3.1.1 *For a set of electrodes S_i which completely enclose the active volume V , we have that:*

$$\Psi(\vec{x}) = \sum_i \psi_i(\vec{x}) = 1 \quad \forall \vec{x} \in V \quad (3.10)$$

$$I_{tot}(t) = \sum_i I_i(t) = -q \nabla \Psi \cdot \vec{v}(t) = 0 \quad \forall t \quad (3.11)$$

$$Q_{tot}(t) = \sum_i Q_i(t) = 0 \quad \forall t \quad (3.12)$$

Eq. 3.12 states that the core will always register the same as observed by the segment sum, only inverted.

3.2 Pulse formation

3.2.1 The nature of single interaction events

In an event, we usually have more than one interaction instantaneously created in the detector. True events are most of the time linear superpositions of single interaction events. Such superpositions create charge signals with a complex time dependency. The time dependency of charge signals from single interactions on the other hand, is fixed by the momentary position \vec{x}_e of the electron cloud with charge $-q$ and the position \vec{x}_h of the hole cloud with charge $+q$ ³. The time dependent charge signal induced in segment i

³The amount of holes created always equals the amount of electrons created. In the case of neutron damage, this balance can be destroyed during the collection process and time dependent charge distributions might be more appropriate. However, according to [36, 37], such effects are unimportant for position spectroscopy

can then be written according to For. 3.4 as:

$$Q_{qi}(t) = q[\psi_i(\vec{x}_e(t)) - \psi_i(\vec{x}_h(t))] \quad (3.13)$$

At the time t_0 when the interaction took place, $\vec{x}_e(t_0) = \vec{x}_h(t_0)$ and therefore $Q_{qi}(t_0) = 0$. The next few hundred nanoseconds, these charges are separated and travel in opposite directions towards their collecting electrodes. For our detector, the electrons will travel towards the positively biased core electrode, while the holes will be collected by one of the segments.

When such a charge cloud has reached its collecting electrode, these charges will recombine with their mirror charges. At that moment a discontinuity in the current signals occurs. The charge signals however never show a discontinuity, as these signals are the result of an integration of the current flowing to the electrodes. To correctly describe the observed charge signals, we have to extend Eq. 3.4 and assume that:

Corollary 3.2.1 *The charge Q_{qj} after collection of charge q by electrode i and as registered by electrode j is observed as*

$$Q_{qj} = -q\delta_{i,j} \quad (3.14)$$

This means that the charge q is virtually staying at electrode i . This assumption is necessary to secure that the calculated charge signals after collection of the free charges are constant⁴ and proportional to the total charge collected by the individual electrodes. For an n-type detector, hit segments will therefore always deliver negative charge signals as they collect positive charges (see e.g. Knoll [31, p.409]), while the core will produce positive signals. Segments that are not hit will only show *transient charge signals*, which are only non-zero as long as the charge collection process takes place.

The drop in current that occurs when a charge carrier is recombined at an electrode can be calculated from Eq. 3.6, evaluated at the position where the charge is collected. This discontinuity in the current signals will show up as a kink in the slope of the charge signals. In particular for the core electrode, this kink is expected to be more pronounced when electrons are collected than when an equal amount of holes are collected. This is mainly because of the cylindrical geometry of the core weighting field (see Eq. 3.16) which weight is r_{max}/r_{min} times less when holes are being collected compared to when electrons are being collected.

⁴In this statement, the $50\mu s$ decay time of the signals characteristic for these preamplifiers used was neglected. At the time window of interest for position resolution, this is a safe approximation.

For single interaction events, the time between the biggest kink in the core signal and the event trigger time thus corresponds to the electrons time-of-flight. This time interval is a measure for the radial distance at which the ionization took place. This principle is exploited by the *steepest slope method* [23, p.87] (see also chapter 11.1). The total number of kinks in the core or hit segment signals – as far as they all can be resolved – are an indication for the total number of interactions that happened in the detector or segment, respectively. Pulse shape analysis based on this idea has also been investigated [38].

3.3 A two-dimensional playground

It is now tried to put some of the theory described so far in praxis. The illustration presented in the next few sections formed the first step in the direction of the precise detector characterization techniques which will be presented later. Its purpose was originally intended to obtain direct information on the mobility of the charge carriers. Although the method is outdated, it works very instructive as it gives a clear insight in the mechanism behind pulse generation.

To investigate the feasibility of some of the ideas on characterization, existing data on a 6-fold segmented MINIBALL detector was used. This detector has no segmentation in depth, such that the weighting potentials in the coaxial part of the detector can be well approximated by a two-dimensional system.

The presented experimental data was taken by Weißhaar [20, 10] using a collimated ^{137}Cs source. Sorted and averaged data on detector responses were provided corresponding to known (x, y) coordinates in the coaxial part of the detector.

3.3.1 Coaxial weighting potentials

The weighting potentials in the coaxial part of the detector have the advantage that they have a relative simple mathematical description. The weighting potential corresponding to a segment is shown in Fig. 3.1 and can be expanded in cylindrical harmonics⁵ as:

$$\begin{aligned} \psi_1(r, \theta) &= \frac{\ln(r/r_{min})}{6 \ln(r_{max}/r_{min})} + \sum_{n=1}^{\infty} B_n \left[\left(\frac{r_{min}}{r} \right)^n - \left(\frac{r}{r_{min}} \right)^n \right] \cos(n\theta) \\ \text{with } B_n &= \frac{2 \sin(n\pi/6)}{n\pi \left[\left(\frac{r_{min}}{r_{max}} \right)^n - \left(\frac{r_{max}}{r_{min}} \right)^n \right]} \end{aligned} \quad (3.15)$$

⁵To prove this, use e.g. the general solution, expressed in cylindrical harmonics as given in [39] and determine the coefficients to match the boundary conditions given by definition 3.5.

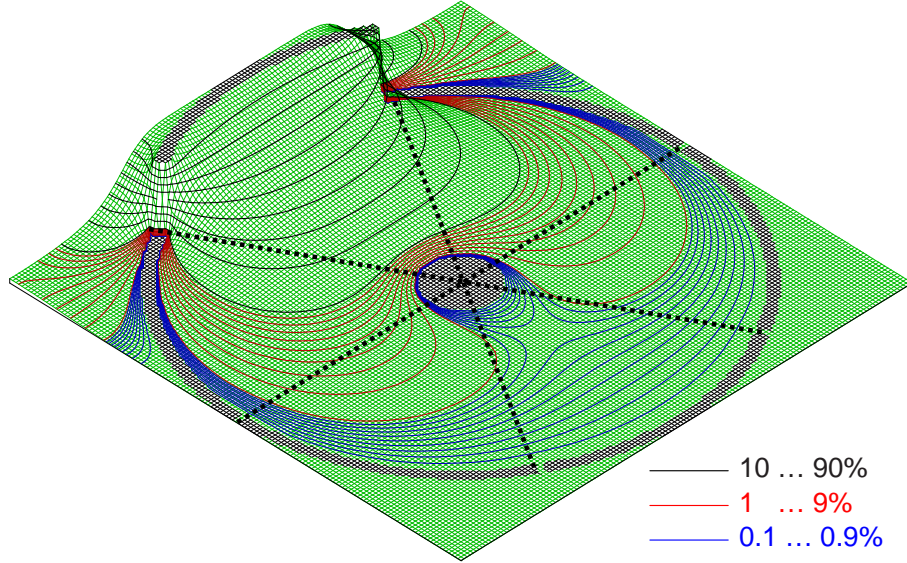


Figure 3.1: Weighting potential ψ_1 for a segment of a 6-fold segmented MINIBALL detector in the coaxial region of the detector.

The constants r_{min} and r_{max} represent radius of respectively the core and the segment electrodes. The weighting potential of the neighboring segments is just a rotated copy of ψ_1 : $\psi_j(r, \theta) = \psi_1(r, \theta + (j - 1)\pi/3)$. The core weighting potential ψ_0 is independent on θ and is given by

$$\psi_0(r) = 1 - \ln(r/r_{min})/\ln(r_{max}/r_{min}) \quad (3.16)$$

3.3.2 Locating the electrons

For our two-dimensional system, For. 3.13 gives us for a specific time a set of seven nonlinear equations (one for each segment plus the core) to solve for the position of only 4 coordinates $\vec{x}_e(r, \theta)$ and $\vec{x}_h(t)(r, \theta)$. However, for single interactions, only three segments really provide useful independent information: According to For. 3.12, the core signal can be constructed from the segment signals and only the hit segment and its two closest neighbors provide us with signals of a reasonably amplitude. We therefore do not have enough information to triangulate both the position of the electron and the hole cloud simultaneously. However, if one of the charge carriers is collected, we do have enough information to track down the position of the remaining free charge carrier, and so, to measure its velocity.

We will demonstrate this principle by taking averaged trace data on responses originating from collimated positions close to segment 4. In this case the holes will be immediately collected and the shape of the charge sig-

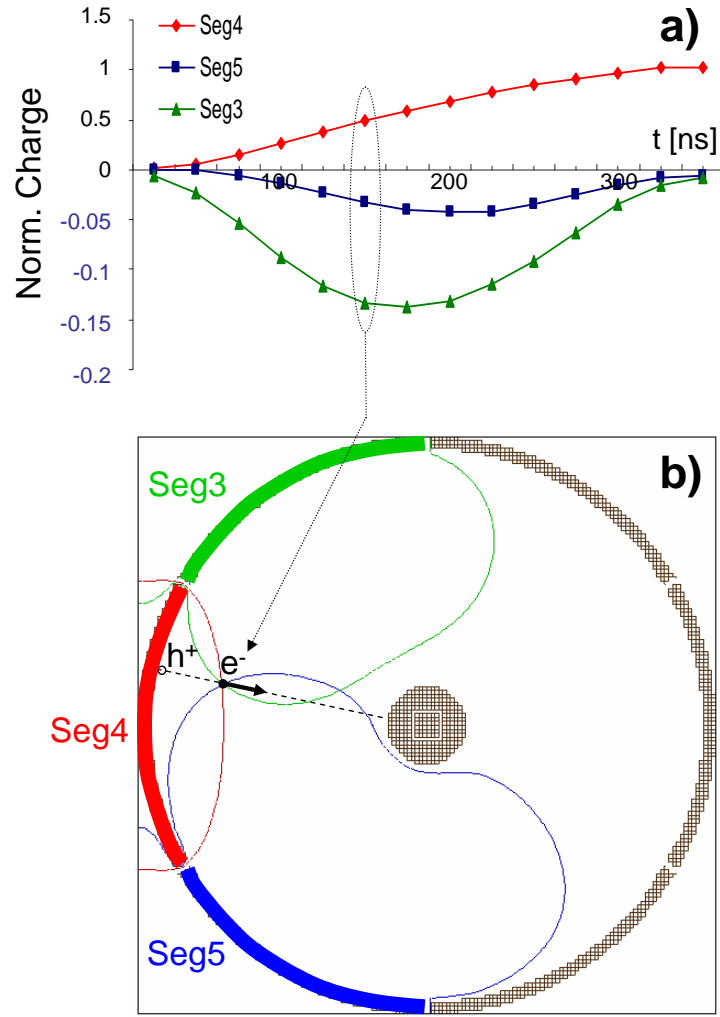


Figure 3.2: An illustration of the procedure to trace electrons in the bulk of the germanium crystal. a): Observed charge signals in segment 4 and its neighbors for a single event close to segment 4. b): The electrons temporary position deduced from the traces in a) by combining information of segments 3,4,5.

nals is only depending on the path the electrons follow as they are traveling towards the core electrode. The corresponding normalized charge signals of segment 4 and the transients in the neighboring segments 3 and 5 are shown in Fig. 3.2a). Remark that the y-scale for the negative transients is blown up by a factor of 10 compared to the positive scale. The different channels were sampled synchronously every 25 ns. Assuming the holes are collected, the momentary coordinate of the electron cloud will be given for a specific time sample t by

$$Q_{qi}(t)/q + \delta_{i,4} = \psi_i(\vec{x}_e(t)) \quad i = 3, 4, 5 \quad (3.17)$$

According to this formula, we find the momentary position of the electrons at the crossing of three weighting-equipotential lines. The weighting potentials are used here in a fashion as if they were distance measures to a specific electrode. In this way, the electron path can be reconstructed as illustrated in Fig. 3.2b).

In this way, the path of the electrons was calculated for several collimator positions. These paths, together with the corresponding collimator positions (marked with a black full square) are shown in Fig. 3.3. The background used in this picture was taken from [20, p.33] and reveals the position of core and segment electrodes. It was obtained by measuring the time-normalized amount of observed single interactions as function of the collimator position.

3.3.3 Limitations of the method

The derived trajectories agree well with the true collimator positions. However, the analysis leading to the results shown in Fig. 3.3 up to now has been deliberately presented in a simplified way. To obtain these results, effects of real electronic measuring equipment had to be taken into account. Doing so, it turned out that a phenomenon called *crosstalk*, the fact that signals of different segments can be influenced by each other, plays an important role. In the next chapter, the origin of this effect is explained.

Another important effect is caused by the finite reaction time of the electronics: Any measurable signal has a finite rise time. This causes that sharp details in the traces, such as the beginning and ending of the traces shown in Fig. 3.2a, are blurred. How one can deal with these effects is discussed in chapter 5. For these reasons, the characterization methods discussed in chapters 5, 9 and 10 offer a more elegant way to derive information on mobilities.

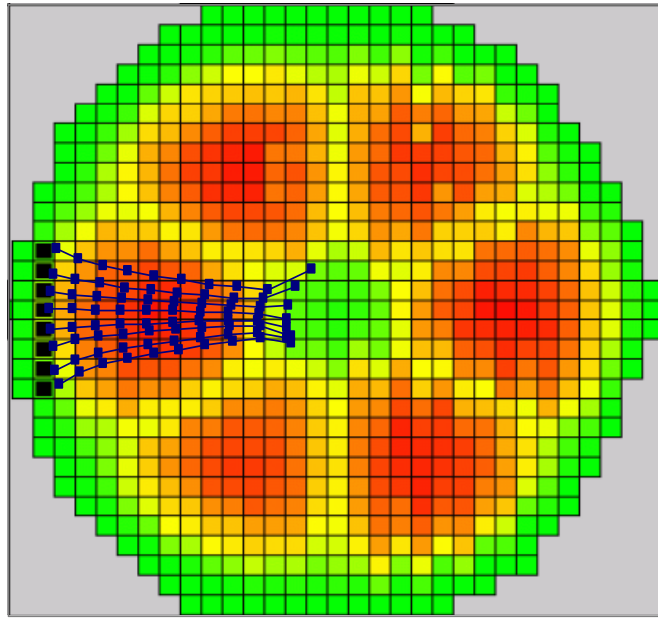


Figure 3.3: The electron path in the bulk of the germanium crystal. The resulting trajectories are shown with open squares. (the time between points is fixed at 25 ns). The collimator position assigned with the obtained trajectories are indicated with full squares. The background was taken from [20, p.33] and reveals the location of the electrodes: It shows the time-normalized amount of observed single interactions as function of the collimator position.

Chapter 4

The detector-preamplifier connection

The need for low noise, high amplification of the detector signals over a broad bandwidth in the high frequency domain has created a big challenge for the construction of charge sensitive preamplifiers suited for position sensitive HPGe detectors. Combined with the spatial limitations caused by the high segmentation of these detectors, severe construction challenges were created for the wiring of these preamplifiers with the crosstalk, shortly introduced in the previous chapter, as consequence. However, crosstalk is not necessarily the result of construction errors. In fact, it will be shown here that there exist a theoretical limit upon which crosstalk cannot be improved on.

4.1 Small signal equivalent for the detector

In the description of electronic devices, the signals can often be regarded as a superposition of a small AC signal, carrying the actual information, superposed on time invariant DC currents and potentials. The DC components are only necessary to bring the electronic components in the wanted working point. An example is the DC bias potential that is applied on a detector diode, such that the diode becomes fully depleted.

If only the small, time dependent variations in currents and potential are of interest, it is advantageous to make a small signal equivalent scheme (or AC equivalent scheme) of the true circuit. For this, the DC potential and currents are disregarded and all components are replaced by a suitable substitute, describing the behavior of that particular component near the working point as defined by the DC currents and potentials. The AC equivalent scheme is then able to describe the information of interest, but loses any information on DC components.

A small signal equivalent circuitry for a detector, without the presence of the preamplifier is shown in Fig. 4.1. For simplicity, we assumed only two

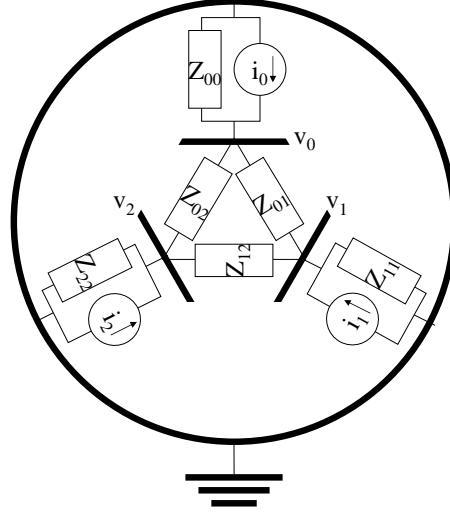


Figure 4.1: The small signal equivalent scheme of a segmented detector.

segment electrodes labeled 1,2. The core electrode is indicated with label 0. As discussed, the bias potential to deplete the detector is disregarded in such schemes. The electrodes are surrounded by the encapsulating material which is at ground potential.

As documented by Gatti et al. [40], in the AC equivalent scheme, the depleted detector can be described by a network of capacities: Each electrode i is coupled to ground by the capacity C_{ii} and to each of the other electrodes j by a capacity C_{ij} which is typically of the order of a few pF. These capacities are resulting from the crystal geometry and the encapsulation. The current induced on electrode i by movement of free charge carriers inside the detector is given by For. 3.6 and is incorporated in the model by an AC current source i_i generated between ground and electrode i . These currents cause that the electrode potentials differ from ground and will take on the value v_i . The relation between these voltages and the currents is given by Kirchhoff's law:

$$\begin{aligned} i_0 &= v_0/Z_{00} + (v_0 - v_1)/Z_{01} + (v_0 - v_2)/Z_{02} \\ i_1 &= v_1/Z_{11} + (v_1 - v_0)/Z_{01} + (v_1 - v_2)/Z_{12} \\ i_2 &= v_2/Z_{22} + (v_2 - v_0)/Z_{02} + (v_2 - v_1)/Z_{12} \end{aligned}$$

with impedance $Z_{ij} = sC_{ij}^{-1}$ as written in Laplace¹ transformed space.

¹Use the substitution $s = i\omega$ if the Fourier transformed space is preferred.

This can be more elegantly casted into a matrix form:

$$\vec{i} = \begin{pmatrix} i_0 \\ i_1 \\ i_2 \end{pmatrix} = \begin{pmatrix} \sum_i Z_{0i}^{-1} & -Z_{01}^{-1} & -Z_{02}^{-1} \\ -Z_{01}^{-1} & \sum_i Z_{1i}^{-1} & -Z_{12}^{-1} \\ -Z_{02}^{-1} & -Z_{12}^{-1} & \sum_i Z_{2i}^{-1} \end{pmatrix} \cdot \begin{pmatrix} v_0 \\ v_1 \\ v_2 \end{pmatrix} = \mathbf{Z}^{-1} \cdot \vec{v} \quad (4.1)$$

The non-diagonal matrix elements of \mathbf{Z}^{-1} couple the potentials to currents induced on other electrodes. These elements are thus responsible for the appearance of crosstalk. Their influence can only be reduced by decreasing the segment to ground impedances, such that off-diagonal elements become negligible. This has to be realized in the interface between detector and preamplifier.

4.2 The detector-preamplifier interface

When the detector is coupled to the preamplifiers, For. 4.1 remains valid, provided we adapt the impedances accordingly. In reality, the detector is connected to the preamplifiers as shown in Fig. 4.2. This picture differs from Fig. 2.5 in the point that the cold FET is not explicitly shown as it is principally a part of the amplifier. The detector is biased over the load resistor R_l . The core is AC coupled to its preamplifier using a large capacity C_{ac} , while the segments are DC coupled.

The AC equivalent circuits for the calculation of the impedances in For. 4.1 are shown in Fig. 4.3. The capacities C_{ii} and C_{FET} are normally matched in order to optimize on the preamplifiers noise performance (see [21, 41], [22, p.72]). Therefore they are both in the lower pF range. For our detector, the following values are realized:

$$\begin{aligned} R_l &= R_{fb} = 1.2 \text{ G}\Omega \\ C_{ii} \approx C_{FET} &\ll C_{ac} = 1200 \text{ pF} < AC_{fb} \approx 20 \text{ nF} \end{aligned}$$

In both AC and DC schemes, the feedback loop has been replaced by their Miller² equivalents. For the DC coupled segments (see Fig. 4.3b.), this causes that the detectors intrinsic capacity C_{ii} between segment i and ground and the FET input capacity C_{FET} is quasi short connected by the much larger Miller capacity AC_{fb} . We therefore identified that

$$\forall i > 0, Z_{ii} = Z_{fb} = [sAC_{fb} + A/R_{fb}]^{-1} \quad (4.2)$$

For the AC coupled core electrode (Fig. 4.3a.), the situation is slightly more complicated. The impedances R_{fb} and $1/sC_{00}$ are effectively short connected

²For a comprehensive introduction to the Miller effect, see [42], which also includes the original paper.

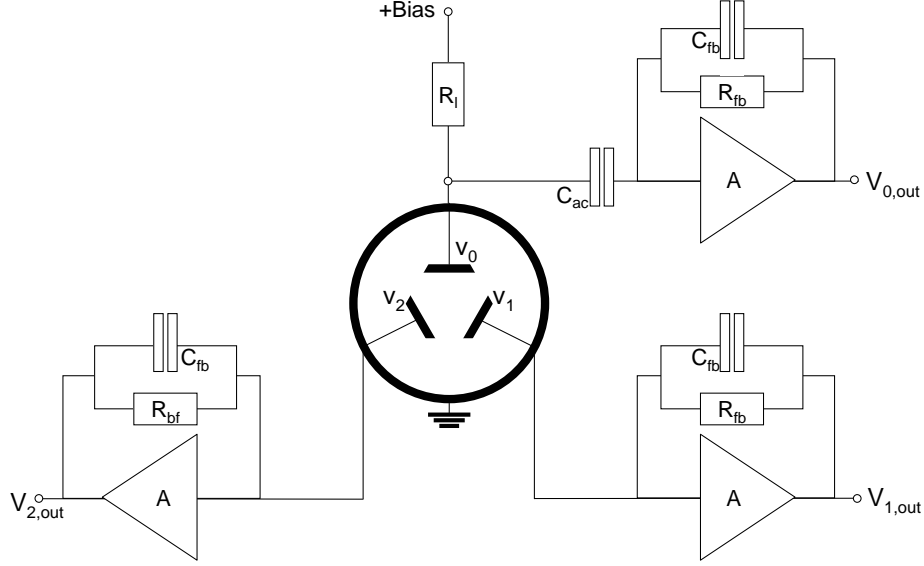


Figure 4.2: A schematic layout of the coupling between detector and preamplifiers.

by the series circuit of C_{ac} with Z_{fb} . The capacity C_{FET} can again be neglected with respect to AC_{fb} . The impedance between core and ground therefore becomes

$$Z_{00} = 1/sC_{ac} + Z_{fb} \quad (4.3)$$

Since typically $C_{ac} < AC_{fb}$, $Z_{00} \approx 1/sC_{ac}$ and thus the core is less effectively coupled to ground than the segments, for which we have $Z_{fb} \approx 1/sAC_{fb}$. This will cause that an AC connected preamplifier is more contributing to crosstalk than a DC connected preamplifier.

The impedances between electrodes are not affected by the coupling with the preamplifiers. Summarizing for our twofold segmented detector model, we can therefore in good approximation write:

$$\mathbf{Z}^{-1} = \begin{pmatrix} Z_{00}^{-1} & -sC_{01} & -sC_{02} \\ -sC_{01} & Z_{fb}^{-1} & -sC_{12} \\ -sC_{02} & -sC_{12} & Z_{fb}^{-1} \end{pmatrix} \quad (4.4)$$

4.3 General solution

To calculate the potentials $\vec{v} = \mathbf{Z} \cdot \vec{i}$ on the electrodes, we need a method to invert the matrix \mathbf{Z}^{-1} for the general case. We have that the diagonal matrix elements in \mathbf{Z}^{-1} are big compared to the off-diagonal elements, as we expect only a small crosstalk. On top, this matrix is symmetric, which

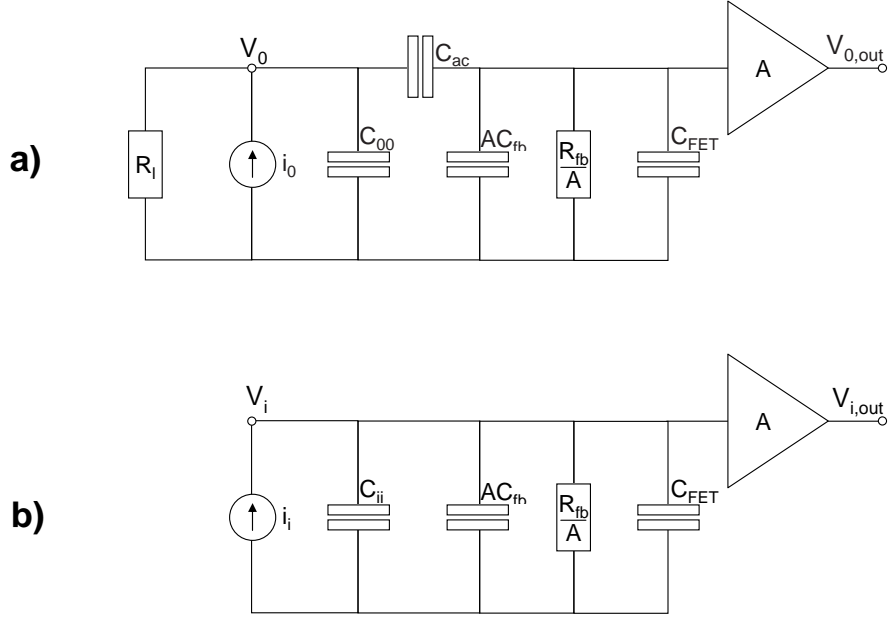


Figure 4.3: AC equivalent of the coupling between detector and preamplifier. a). AC equivalent for an AC coupled amplifier. b). AC equivalent for a DC coupled amplifier.

makes that its inverse \mathbf{Z} will also be symmetric: Observed at the electrodes, the crosstalk from segment i to j is equal to the crosstalk from segment j to i . The off diagonal matrix elements of \mathbf{Z} will again be small compared to its diagonal elements. We can therefore write that

$$\begin{aligned}\mathbf{Z}^{-1} &= \mathbf{Z}_d^{-1} + \epsilon \\ \mathbf{Z} &= \mathbf{Z}_d + \delta \\ \mathbf{Z}^{-1} \cdot \mathbf{Z} &= \mathbf{1} + \epsilon \cdot \mathbf{Z}_d + \mathbf{Z}_d^{-1} \cdot \delta + \epsilon \cdot \delta\end{aligned}\quad (4.5)$$

Such that the matrix \mathbf{Z}_d^{-1} only contains the relatively big diagonal matrix elements of \mathbf{Z}^{-1} and has the simple (diagonal) inverse \mathbf{Z}_d . The term $\epsilon \cdot \delta$ in For. 4.5 is of second order compared to the other terms, and can therefore be neglected. We thus obtain a simple formula for δ :

$$\delta = -\mathbf{Z}_d \cdot \epsilon \cdot \mathbf{Z}_d$$

Since \mathbf{Z}_d is diagonal, the matrix multiplication turns out to be of a very elementary form:

$$\delta_{ij} = -\mathbf{Z}_{dii} \epsilon_{ij} \mathbf{Z}_{djj}$$

For a general quasi-diagonal system, therefore the simple inverse is obtained:

$$\mathbf{Z} = \begin{pmatrix} Z_{00} & -\frac{Z_{00}Z_{11}}{Z_{01}} & -\frac{Z_{00}Z_{22}}{Z_{02}} & \dots \\ -\frac{Z_{00}Z_{11}}{Z_{01}} & Z_{11} & -\frac{Z_{11}Z_{22}}{Z_{12}} & \dots \\ -\frac{Z_{00}Z_{22}}{Z_{02}} & -\frac{Z_{11}Z_{22}}{Z_{12}} & Z_{22} & \dots \\ \vdots & \vdots & \vdots & \ddots \end{pmatrix} \quad (4.6)$$

4.4 The transfer function

For the DC coupled segment i , the voltage at the preamplifier output, according to the AC equivalent scheme Fig. 4.3b, is simply $v_{outi} = Av_i$. For the AC coupled core, the voltage is reduced by a voltage divider. The correct relation is therefore $v_{out0} = AZ_{fb}v_0/Z_{00}$. The relation between \vec{v}_{out} and \vec{v} can therefore be written as:

$$\vec{v}_{out} = A \cdot \begin{pmatrix} \frac{Z_{fb}}{Z_{00}} & 0 & 0 \\ 0 & 1 & 0 \\ 0 & 0 & 1 \end{pmatrix} \cdot \vec{v}$$

Combined with For.4.6, we obtain a transfer function for the detector-preamplifier system:

$$\vec{v}_{out} = AZ_{fb} \cdot \begin{pmatrix} 1 & -sC_{01}Z_{fb} & -sC_{02}Z_{fb} \\ -sC_{01}Z_{00} & 1 & -sC_{12}Z_{fb} \\ -sC_{02}Z_{00} & -sC_{12}Z_{fb} & 1 \end{pmatrix} \cdot \vec{i} \quad (4.7)$$

Remark that the transfer matrix is no longer symmetric. The total registered charge is therefore different from zero. All channels will suffer from baseline shifts as soon as any segment is hit. The amplitude of these shifts will depend on the specific hit pattern of the event. Consequently, a simple calibration for a segmented detector can become rather complex when looked at in detail.

4.5 Back in time(-domain)

The diagonal elements of matrix 4.7 describe a charge integration. This is easily verified using the inverse laplace transform \mathcal{L}^{-1} [43],[44, p.1019]. In the time domain, $AZ_{fb} \cdot \vec{i}$ becomes a convolution of $\vec{i}(t)$ with the transfer function $\mathcal{L}^{-1}(AZ_{fb})$:

$$\mathcal{L}^{-1}(AZ_{fb}) = \begin{cases} \frac{1}{C_{fb}} e^{-t/\tau} & \text{if } (t \geq 0) \\ 0 & \text{elsewhere} \end{cases} \quad (4.8)$$

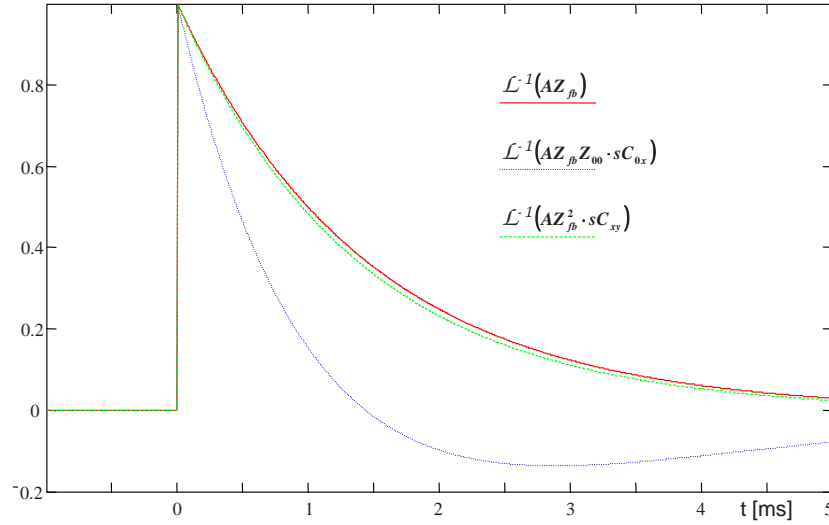


Figure 4.4: Comparison of the time dependence of crosstalk, equations 4.9 and 4.10 to the main response, Eq. 4.8. The signals were normalized at $t = 0$. For Eq. 4.9, a ratio $C_{01}/AC_{fb} = 20$ was used.

The exponential decay has a time constant $\tau = R_{fb}C_{fb} \cong 1$ ms. This corresponds to the characteristic decay time of the first stage of the preamplifier (see chapter 2.3).

The biggest crosstalk components are caused by the off-diagonal elements $sC_{0i}Z_{00} \approx C_{0i}/C_{ac}$. This causes crosstalk on the promille level in the segment signals, of which the shape is proportional to the core signal. More exact, by back transformation we obtain the response function:

$$\mathcal{L}^{-1}(AZ_{fb}sC_{0i}Z_{00}) = \left[\frac{C_{0i}}{C_{ac}} + \frac{C_{0i}}{AC_{fb}}(1 - t/\tau) \right] \cdot \mathcal{L}^{-1}(AZ_{fb}) \quad (4.9)$$

The crosstalk induced by segments is given by the off-diagonal terms $sC_{ij}Z_{fb} \approx C_{ij}/AC_{fb}$. These amplitudes are typically below the promille level. The exact line shape of segment-to-segments induced crosstalk is predicted as:

$$\mathcal{L}^{-1}(AZ_{fb}^2 sC_{ij}) = \frac{C_{ij}}{AC_{fb}}(1 - t/\tau) \cdot \mathcal{L}^{-1}(AZ_{fb}) \quad (4.10)$$

The time dependency of the induced crosstalk is summarized in Fig. 4.4. Since the amplitudes of these functions is evaluated in the lower μ s range ($t \ll \tau$), the differences in line shape will not be observed.

The effect the core decoupling capacity has on the crosstalk was experimentally verified by Weißhaar [45]. The results are shown in Fig. 4.5. The effect of crosstalk was analyzed by observation of the energy shifts it causes

on the segment sum of multiply hit segments with respect to single hits. The observed shifts clearly show an inverse proportional behavior as expected from For. 4.9. Similar crosstalk measurements were recently performed on an AGATA detector. The obtained data shows remarkable resemblance with the model [46]. It demonstrated that (proportional³) crosstalk can be controlled down to the promille level such that first order effects as described by this model become visible.

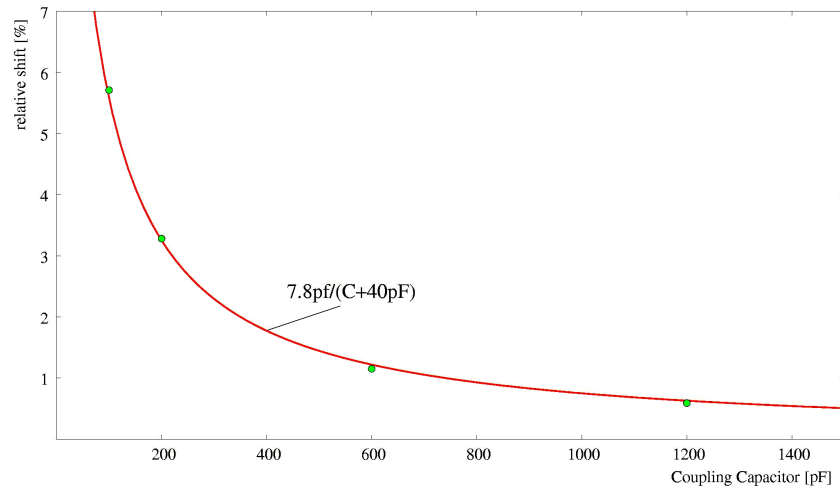


Figure 4.5: Crosstalk observed in segments as function of the decoupling capacity (Figure taken from [45]).

³see next chapter

Chapter 5

Response Functions

Looking at the schematic overview in Fig. 2.5 of the front-end electronics, one realizes that the signals digitized in the ADC's differ considerably from the current signals produced in the detector. Using an appropriate description of the charge dynamics and weighting potentials, the charge signals are calculated as they appear on the electrode surfaces of our detector (see chapter 3). To compare these calculations with the signals as registered by the ADC's, one has two options. The simulation either has to be convoluted with the response functions of the preamplifier, the Nyquist filter and the amplifier stage in the DGF, or the measurement needs to be deconvoluted with these responses. Since the second option is a mathematical ill-posed problem, the first option is preferred.

5.1 The Analog Front-end Response

The straight forward way to measure these responses is to use a pulse generator. Unfortunately, in the cryostat of the detector under measurement (as well as in all MINIBALL's detector cryostats) there is no test input available. Therefore the response of the detector/preamplifier stage was simulated with a PB-4 Pulse Generator with 50 ns (measured 46.5-49 ns) rise time and 50 μ s fall time, values very close to the real transfer function of the PSC823 charge sensitive preamplifier. This pulser signal $P(t)$ was fed directly into the DGF's. The derivative of the pulser signal as recorded by the DGF can then be taken as the combined response function of preamplifier and DGF.

Since in the final characterization method an averaging procedure is applied to the traces, also the influence of this procedure in the simulation has to be taken into account. A simple way to deal with this is by absorbing the effect of the averaging procedure in the response function. Therefore about a thousand of these pulser signals were recorded for each channel of the DGF's. The average of these traces was taken analogously to the procedures the real data analysis is submitted to. In this way, the influence of

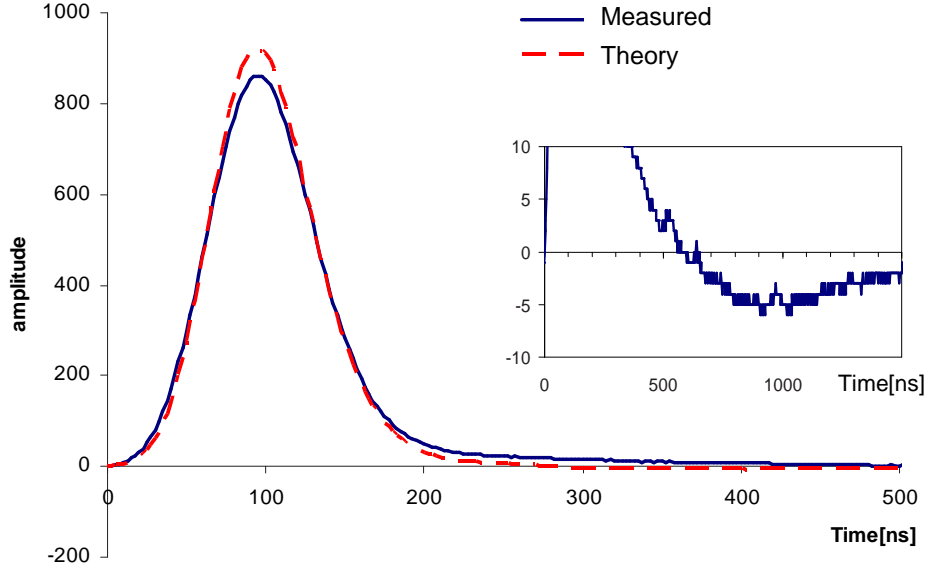


Figure 5.1: Comparison between the theoretical (equation 5.1) and a measured response function. The integrals of the responses were normalized to an arbitrary number. The insert shows a zoom on the long tail observed in the measured response.

the averaging procedure is passed onto the response function.

The averaged response functions were found to be in good agreement with theoretical expectations for the electronics shown in Fig. 2.5. The theoretical model for the response function $R(t)$ consist of the derivative of the pulser signal $P(t)$, as measured by a high quality oscilloscope, four times convoluted with the response of a first order Nyquist filter to obtain the forth order anti-aliasing filter present in the DGF's (corner frequency $F_c = 20$ MHz) and finally convoluted with the response of the averaging procedure. The latter is shown in the next section to correspond to a symmetrical triangular function $C(t; T_s)$ of which the FWHM value equals the sampling period $T_s = 25$ ns. The theoretical expression for the response function $R(t)$ therefore becomes:

$$R(t) = \frac{dP(t)}{dt} \otimes C(t; T_s) \otimes \begin{cases} (1 - 2\pi F_c t)^3 e^{-2\pi F_c t} & \text{if } (t \geq 0) \\ 0 & \text{elsewhere} \end{cases} \quad (5.1)$$

This function is compared in Fig. 5.1 with a typical response obtained using a pulse generator. Its $FWHM = 80$ ns is in good agreement with the measured width. However, the measured traces show a long tail, which has a small negative part as seen in the insert in Fig. 5.1. This part causes an overshoot in the measured traces and therefore demonstrates the necessity for the implementation of measured response functions in the simulation

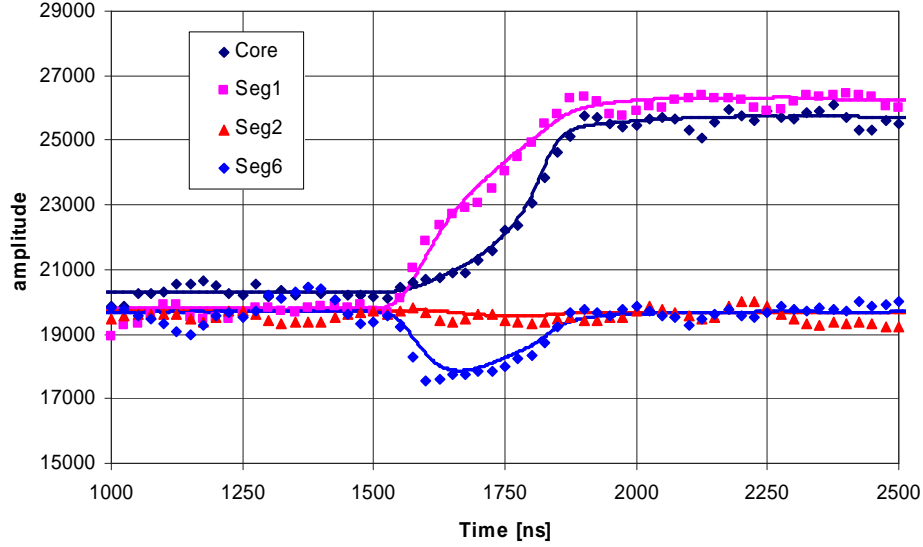


Figure 5.2: Comparison of raw 60 keV data (sampled at 40 MHz) with its average. The picture shows an event at 1 cm depth, near the segmentation line between segment 1 and 6 (for labeling of segments see Fig. 5.3)

rather than to rely on theoretical models. Response functions with a time basis longer than $1.5 \mu\text{s}$ were employed to account for the observed effect.

5.2 Averaging routine

Single events usually contain too much noise to extract qualitative mobility data and therefore the noise has to be averaged out. It is evident that the influence of this averaging procedure has to be accounted for and the inclusion of its effect in the total response function is very attractive because of its simplicity. Averaging becomes necessary particularly when working with low energy γ -rays as is the case in the characterization of the electron mobility (chapter 9). An example of a single 60 keV event is shown in Fig. 5.2. Without averaging, the noise in such events would dominate the traces fine structure. However, the noise reduction is not the only motivation for the averaging procedure. Using a collimator setup, the region in which the crystal interacts with the collimated beam cannot be infinitesimally small. In cases where the influence of this finite volume is not negligible, the averaging produces an event which is a statistically better defined representative for the selected volume. This property is especially of use for the hole mobility characterization as will be discussed in chapter 10.

As the digital electronics is based on a 40 MHz sampling frequency, averaging has to take into account that all the pulses are distributed along

wide 25 ns intervals in time and a time alignment is needed. The averaging routine runs a single time through the data set and systematically updates the average when it finds an acceptable event. For the update, the core or the active segment is fitted with the average in order to obtain the best possible time alignment of this segment before this event is absorbed into the average. In this procedure, the time shift is not limited to be a multiple of a 25 ns DGF time tick. A linear interpolation is used to transform the shifted sampling of the event to time ticks that are coincident with the average $T_{av}(t)$.

The influence of the average procedure can now be understood as follows. A single event only possesses information on the ideally measured trace $T(t)$ sampled at distinct intervals $\Delta T (= 25 \text{ ns})$. Suppose that the last sample point before time t lies a distance y before this time t . The value $T(t)$ is then approximated using a linear interpolation of the samples $T(t - y)$ and $T(t - y + \Delta T)$. The trace $T(t)$ can be measured several times independently. Each new event will give a different y . Statistically, these time shifts y are homogeneously distributed in the interval $[0 \cdots \Delta T]$ and the statistic average T_{av} becomes

$$T_{av}(t) = \frac{1}{\Delta T} \int_0^{\Delta T} T(t - y) + \frac{y}{\Delta T} (T(t - y + \Delta T) - T(t - y)) dy \quad (5.2)$$

This expression can be rewritten in the form of a convolution¹:

$$T_{av}(t) = C(t) \otimes T(t) \quad (5.3)$$

$$C(t) = \begin{cases} 1 + t/\Delta T & \text{if } -\Delta T \leq t \leq 0 \\ 1 - t/\Delta T & \text{if } 0 \leq t \leq \Delta T \\ 0 & \text{elsewhere} \end{cases} \quad (5.4)$$

in which $C(t)$ has a triangular symmetric shape and contains the influence of the sampling period ΔT . In this way the average $T_{av}(t)$ is not restricted to the sampling rate, but the signal can be reconstructed at any time t . The averages that were built and shown e.g. in Fig. 5.2 are built at an equivalent sampling rate of 400 MHz rather than the original 40 MHz.

5.3 Crosstalk

Crosstalk is another component of the signal deformation which has to be described precisely and corrections for its existence need performed. Some crosstalk is inherently connected with the use of an AC coupled core preamplifier as pointed out in chapter 4. However, the existence of other types

¹The penalty of the extra convolution could in principle be reduced by using a histogramming procedure of the shifts y instead of the interpolation. Such procedure however would need much more statistics and turned out more complicated to realize in practice.

of crosstalk is not excluded. For these highly segmented detectors crosstalk has been observed [47, 48] to consist of two components. One component is directly proportional to the inducing signal. We will refer to this type as *proportional crosstalk*. It is obvious that proportional crosstalk is particularly harmful to energy resolution. The second component is proportional to the derivative of the induced signal and will be addressed as *derivative crosstalk*. Since the derivatives of charge signals are only non-zero during the rise time of the inducing signal, derivative crosstalk is especially important for position spectroscopy.

5.3.1 Proportional Crosstalk

The proportional fraction will cause shifts in energy whenever two neighboring segments are hit. It is therefore also of importance in building energy add-back spectra. Fig. 5.4 shows the typical proportional crosstalk amplitudes in segments as function of the angle as a 60 keV source is moved at constant depth, 1 cm behind the front surface, around the detector. All segments suffer from a lowering of the baseline, independently on which segment is hit. These crosstalk fractions are induced by the core such as the mechanism described in chapter 4. The lowering is less for front segments than for back segments. Proportional crosstalk induced by the core (see Fig. 5.4) is -0.66% of the core signal for a segment in the back and -0.30% for a segment in the front².

Besides the common fractions caused by the core signal, an additional shift of the baseline can be observed when a direct neighboring segment is hit. This is caused by the proportional crosstalk coming from the neighbor segment. Data from direct neighboring segments to hit segments were therefore excluded from Fig. 5.4 and shown separately in Fig. 5.5. Observed proportional crosstalk between segments always

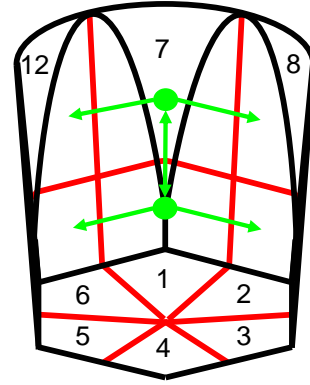


Figure 5.3: Schematic view of the crystal indicating the labeling of the 12 segments of the detector. Observed crosstalk induced by a segment is only picked up by its three closest neighbors. Two examples illustrate this behavior: a charge signal in front segment 1 induces crosstalk signals in segments 2, 6 and 7; a charge signal in back segment 7 induces crosstalk signals in segments 1, 8 and 12.

²Amplitudes will always be quoted relative to the core signals amplitude

existed between direct neighbors as shown in Fig. 5.3.

An average value of -0.77% was measured between proportional crosstalk going from front to back as can also be deduced from Fig. 5.5. Other segment-to-segment crosstalk was observed to be less. Such crosstalk is attributed to a weak capacitive (on the order of fF!) coupling between a drain and a source of different amplifiers as explained by Pullia [49].

The segment-to-segment proportional crosstalk still visible in Fig. 5.5 was consequently reduced to below 0.1% after building the same detector into a new cryostat with better shielding between FET's. Also the core to segment proportional crosstalk was slightly reduced. This proportional crosstalk is in agreement with the values reported by Weißhaar [45] for the first AGATA detectors.

5.3.2 Derivative Crosstalk

The difficulty in detecting derivative crosstalk is to distinguish between crosstalk and transient components of the signal. Taking advantage of the high segmentation of the detector, a method was developed to isolate derivative crosstalk and to cancel all transient information from a combination of traces from different events.

The novel method to determine the derivative crosstalk exploiting the segmentation of the detector is based on two neighboring events consisting both of single interactions within a very close range, e.g. interactions at point A and point B in Fig. 5.6. The charge carriers of interactions from both points will be collected by separate segment electrodes, Seg_A and Seg_B . Since all other segment electrodes besides Seg_A and Seg_B cannot resolve the small difference in position, the transient signals induced in any electrode Seg_X besides Seg_A and Seg_B primarily do not depend on a very small position difference between A and B . The signals symmetrically change as indicated in Fig. 5.6 when changing from events at point A to events at point B . As a consequence, when both normalized charge signals are subtracted, the same residual in Seg_A will show up but inverted in Seg_B . The residuals in all other segments will be zero.

In case of crosstalk from Seg_A or Seg_B to Seg_X , nonzero residuals will appear in Seg_X . The difference in sign between the residuals in Seg_A and Seg_B contains information on whether the crosstalk is caused by the signal in Seg_A or by Seg_B . By investigation of all possible combinations of Seg_A and Seg_B , it was observed that derivative crosstalk appears only in direct neighboring segments to Seg_A or Seg_B and behaves also as indicated in Fig. 5.3.

A typical experimental result of the described crosstalk analysis is shown in Fig. 5.7. In this case, a collimated ^{241}Am source was placed on the segmentation line between $\text{Seg}_{A=1}$ and $\text{Seg}_{B=6}$. All the trace residues $A - B$ after subtraction of the normalized events are shown. Including the response

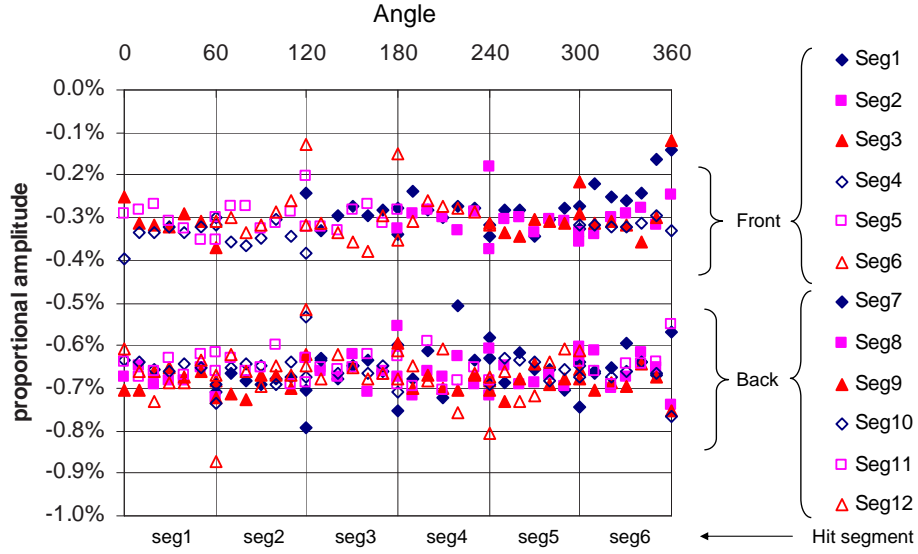


Figure 5.4: The variation of the proportional crosstalk amplitudes with angle and hit segment. All events were measured with 60 keV γ -rays at 1 cm depth. Front segments and back segments register a constant crosstalk induced by the core. Direct neighbors to hit segments were excluded from the graph and plotted separately in Fig. 5.5 so that only core-to-segment proportional crosstalk remains.

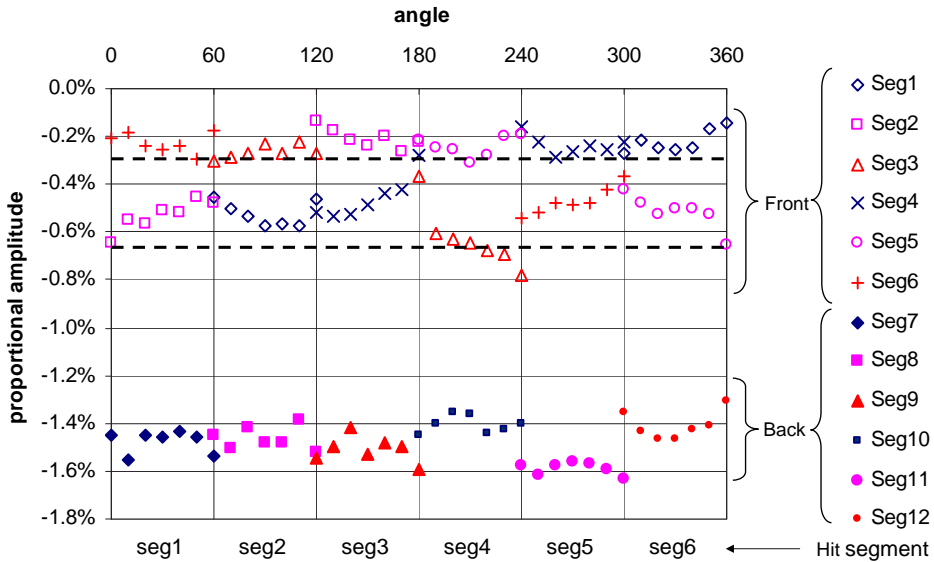


Figure 5.5: The variation of the proportional crosstalk amplitudes with angle and hit segment. Only direct neighbors to hit segments are shown. The average crosstalk induced by the core, as obtained from Fig. 5.4 is indicated with a dashed line. Deviations from this line are attributed to segment-to-segment crosstalk.

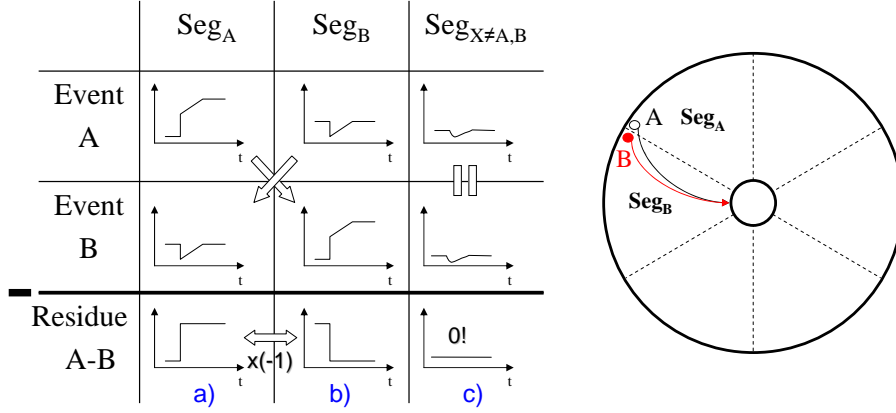


Figure 5.6: A novel method to extract derivative crosstalk in segments Seg_X is based on the charge pulses which are caused by interactions close to the segmentation line between Seg_A and Seg_B . To illustrate the procedure only schematic pulses and subtracted pulses are shown. Ideal pulses from measurements done at position A and B are subtracted. Derivative crosstalk contributions would be determined from non-vanishing pulses in segments Seg_X in row c (details see text).

function of the analog electronics, the measured signals in Fig. 5.7a,b compare very well to the residuals in Fig. 5.6a,b. The events A , B are built by averaging all events that hit Seg_1 and Seg_6 , respectively. The signal in Seg_6 is the inverse of Seg_1 as expected. The residues in all segments, excluding direct neighbors to Seg_1 or Seg_6 , are summarized in Fig. 5.7c. They do not reveal any significant crosstalk. However, the direct neighbors to Seg_1 and Seg_6 – grouped together in Fig. 5.7d and Fig. 5.7e respectively – obviously show crosstalk: Seg_2 and Seg_7 have the sign of a derivative crosstalk from Seg_1 , while Seg_5 and Seg_{12} follow the sign of the signal in Seg_6 . This is in agreement with the assumptions made that the derivative crosstalk is only propagating to direct neighboring segments as illustrated in Fig. 5.3. In Fig. 5.7f, the amplitudes of the proportional and derivative fractions in the crosstalk induced by Seg_6 in Seg_{12} , as shown in Fig. 5.7e, are fit by using the shape of Seg_6 . The optimum fit to the crosstalk consists of $0.72\% \text{ Seg}_6 + 503\% \text{ ns } d\text{Seg}_6/dt$. The maximum induced derivative crosstalk amplitude in Seg_{12} amounts to 4% .

The derivative crosstalk is depending on the rise time of the inducing signal. Their amplitudes are therefore expressed in $\% \text{ ns}$. An inducing signal with a rise time of 200 ns would thus on average induce a 1% amplitude if the derivative crosstalk amplitude is $200\% \text{ ns}$. The measured derivative crosstalk amplitude is typically about $700\% \text{ ns}$ for a crosstalk going from front to its neighboring back and around $500\% \text{ ns}$ in the opposite direction.

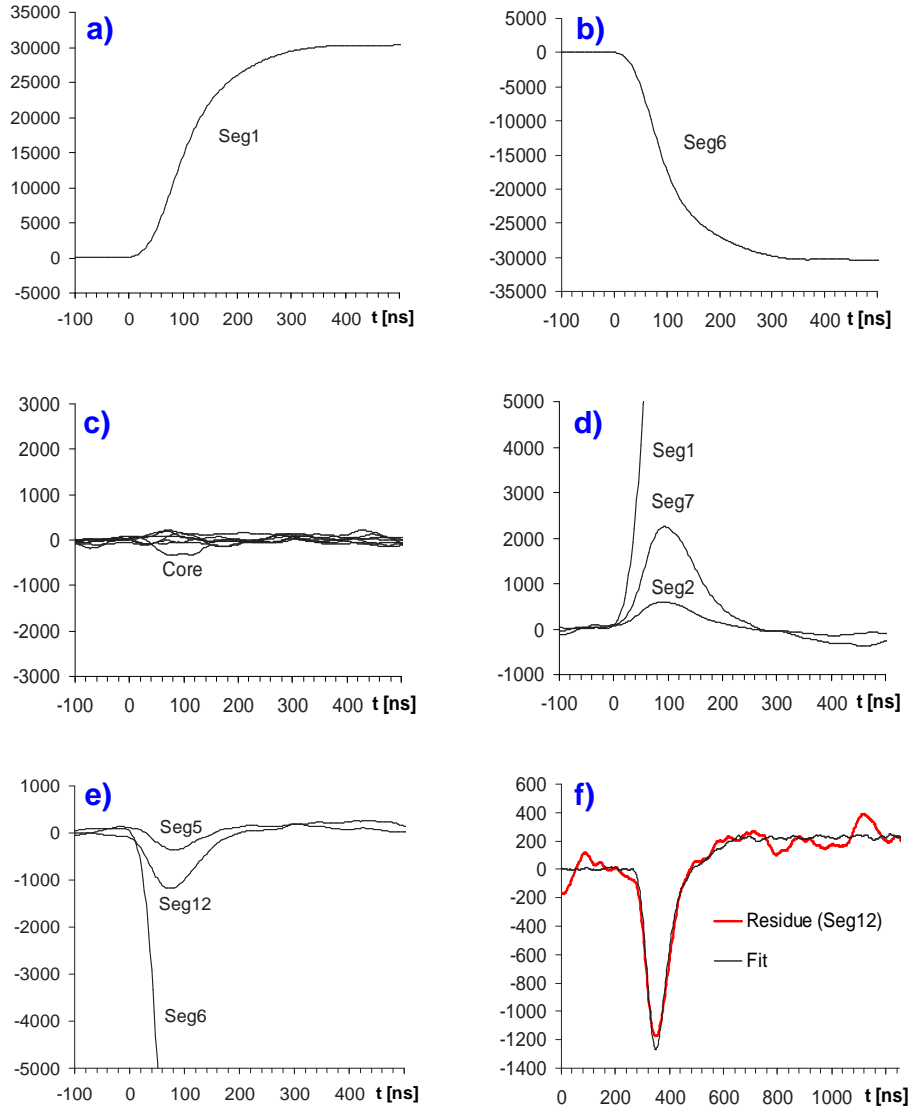


Figure 5.7: Measured results on the residues using the crosstalk detection method. The graphs a),b),c) shows the corresponding residue pulses to Fig. 5.6. Figure c) contains the pulses of no direct neighbor segment to Seg₁ or Seg₆. Figures d) and e) show the direct neighbors to Seg₁ and Seg₆, respectively. f): The residue in Seg₁₂ is fitted exploiting the shape of the inducing signal (Seg₆).

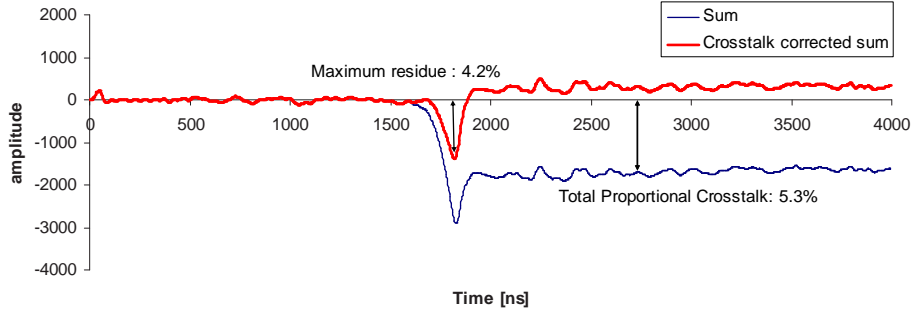


Figure 5.8: The segment signal sum after subtracting the core signal before and after crosstalk correction.

Other segment to neighbor crosstalk is smaller ($<300\%$ ns).

Unlike the proportional crosstalk, the origin of this crosstalk is attributed to construction compromises imposed by practical limitations. Similar amplitudes are expected in the new AGATA detectors. Such crosstalk could be due to bad determined grounds as discussed by Pullia [50]. The use of coaxial or twisted pair cables for the return grounds around drain and feed-back should diminish this effect. At the same time, it is expected to improve on the stability of the preamplifiers against oscillation.

The quality of the crosstalk correction was checked by comparing the sum of all segment signals with the core signal, which should be equal according to For. 3.12. After crosstalk correction and subtracting the core, a residue of typically 4.0% was observed. Since this residue is the sum of 13 signals, it is expected that in every channel the crosstalk is corrected on average to less than 0.4%. This remaining part may be caused by derivative crosstalk induced by or picked up by the core which is not isolated by this method.

In the theoretical introduction and Fig. 5.6, the residuals after subtraction in Seg_A and Seg_B were depicted as true step functions. Instead of giving a mathematical proof, experimental evidence is given by comparing the derivative of the residuals with the measured response function. The comparison shown in Fig. 5.9 clearly demonstrates that the residuals are thus as close to a true step function as the analog front-end electronics allow. This has the advantage that the amplitude of the derivative is maximized, which facilitates the detection of the derivative crosstalk in noisy signals.

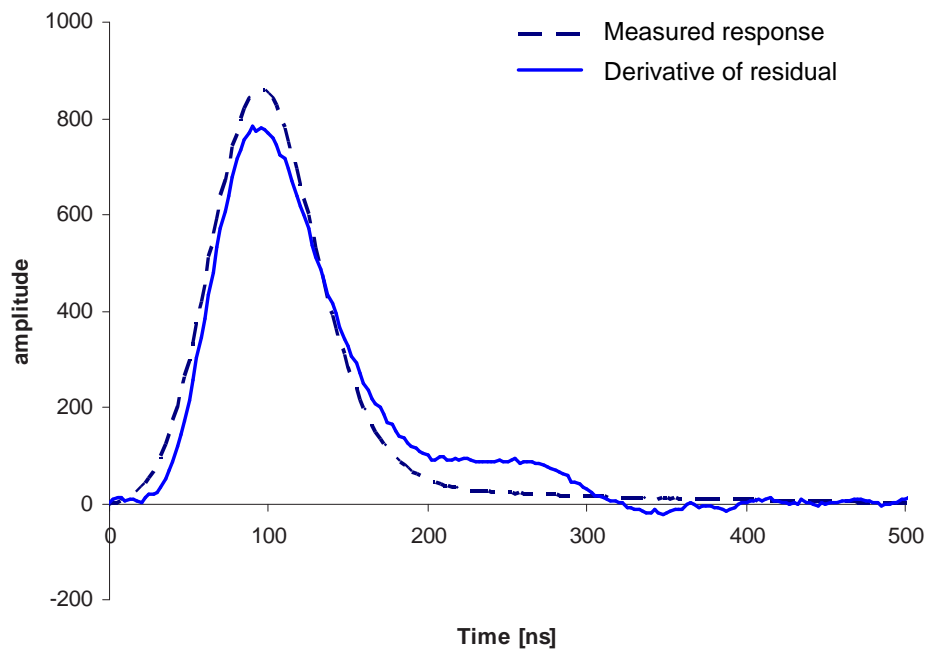


Figure 5.9: Comparison between the derivative of a residual pulse (Fig 5.7a) and the measured response function (shown in Fig. 5.1) for this segment demonstrating that the residuals in Fig. 5.6a,b can be indeed described by true step functions. The integral of the response function is normalized to an arbitrary number.

Chapter 6

Introduction to Mobilities

The final properties we need to know to understand the measurable charge pulses are the electron and hole drift velocities and this throughout the whole volume of the detector. These drift velocities are proportional to the applied field. The proportionality constant is called the mobility. At high field strengths, this coefficient becomes dependent on the field strength itself and moreover, in germanium, it develops from a scalar quantity into a tensor. Problems related to finding the electrical field inside the detector are more of practical nature and will be explained in this chapter. To describe the mobility with high precision is a challenge both for theory (chapters 7,8) as in practice (chapters 9,10).

6.1 A Poisson Solver

The rather complex geometry of the MINIBALL detector crystal (see Fig. 2.3) – but also future tapered, polygonal Ge detectors – require numerical solution both for the weighting potentials discussed in chapter 3 as for the electrical field. The weighting fields are actually the properties of the detector which can be calculated most accurately because they are not influenced by space charge. The space charge created by the ionized donor impurities in the depleted region of the detector greatly influences the electric field in the detector. Hence, to come to a detailed understanding of the charge collection process in such a detector, a numerical program to solve the Poisson equation (a Poisson solver) is necessary.

Such a numerical Poisson solver was developed according to the principles described in [51] and is conform with the commercially available program Simion 7.0 [52]. The 3D calculation of the potentials are based on a rectangular grid. To test the performance and reliability of the novel calculation, a true coaxial segmented detector was simulated. From the comparison with an expansion in cylindrical harmonics (For. 3.15), it was found that a 0.5 mm grid distance was sufficient to simulate the weighting potentials of the true coaxial detector with a relative error of less than 1%.

According to Mihailescu [53], the passivated surface at the back of the detector should act ideally like an electrostatic mirror. Homogeneous Neumann boundary conditions were applied to these surfaces in order that the equipotential lines would end up perpendicular to the passivated surface. The true field however could suffer from field inhomogeneities near the edges of the detector due to the limited knowledge on the real boundary.

A cylindrically symmetric space charge $\rho(r, z)$ is assumed with a distribution that varies linearly in radius and depth. The whole space charge potential is then specified by means of four values. These values were derived from electron mobility data as discussed in chapter 9.4 to be (in units of 10^{10} impurities/cm³):

$$\begin{aligned}\rho(r = 0, front) &= 0.0 & \rho(r = 37mm, front) &= 2.0 \\ \rho(r = 0, back) &= 2.0 & \rho(r = 37mm, back) &= 1.0\end{aligned}$$

The results of the calculations for this type of detector are shown in Fig. 6.1. The electric field strengths with and without space charge are compared. Note how the space charge relocates the high field regions. Without space charge, the highest fields can be found near the core. By inclusion of space charge, the high field regions are redistributed towards the outer contacts as indicated by the arrows in Fig. 6.1.

6.2 Modeling the Mobility

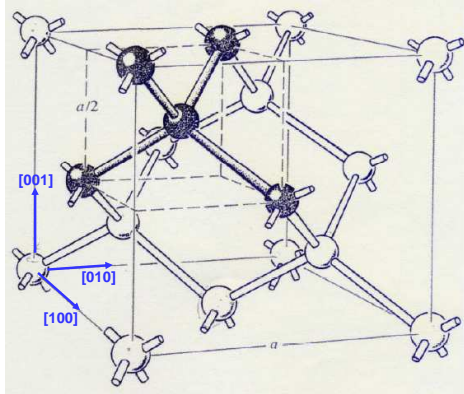


Figure 6.2: The diamond lattice structure of germanium. The lattice constant a equals 5.66 \AA . [54, p.76]

system, such that the positions $(1, 0, 0)$, $(0, 1, 0)$ and $(0, 0, 1)$ are occupied by other corners of the same unit cell, this coordinate system is aligned with the principal $\langle 100 \rangle$ directions. Because the detector has a single-crystalline structure, the crystal orientation is fixed throughout the detector volume.

Once the electrical field is specified, the electron and hole drift velocity can be mapped throughout the detector volume using the mobility models described in the next chapters. In mapping the drift velocities, the crystal orientation turns out to play an important role. A discussion of germanium crystal properties and related terminology is thus of use. Germanium has a diamond lattice structure as shown in Fig. 6.2. If one corner of a unit cell of this crystal is placed in the origin of a Cartesian coordinate system,

Such single-crystalline germanium structures are manufactured using the Czochralski technique [55]. In this process a seed crystal is dipped into molten germanium and then slowly withdrawn, while the temperature of the melt is just maintained above the freezing point. The depth direction of the final detector therefore inherits the direction of the initial seed in which the crystal was withdrawn, which is a $\langle 100 \rangle$ direction.

As long as the electron and hole temperatures do not differ much from the lattice temperature, the drift velocity is proportional to the electrical field and the lattice orientation has no influence. In this case the ratio between drift velocity and electrical field strength is given by the mobility coefficient μ_0 . When the temperature of the electrons rises above the lattice temperature – so called hot electrons – the electron drift velocity in a semiconductor will not be parallel to the applied electrical field but will be influenced and determined by the crystal lattice orientation. One speaks here from an anisotropic mobility. This effect was first discovered by Sasaki et al. [56] and is observed for electrons as well as for holes. Also germanium detectors cooled at liquid nitrogen temperature are affected by the effect.

That the average motion of the electrons is not aligned with the applied external field might be surprising and is demonstrating that the internal fields cannot be neglected. In absence of the external field, the systems Hamiltonian describes the interaction of the electrons with the ion lattice and the electron-electron interactions. The complicated many electron system can be approximated by an effective Hamiltonian, in which the electrons behave independently (*Bloch electrons*). The effective Hamiltonian inherits the periodicity of the underlying lattice structure. The behavior of electrons under action of such periodic potentials can be studied with *Bloch functions* [54, p.133]. These state that the eigenfunctions of such systems can be found under the form of plane waves, modulated by a function $u(\vec{r})$ with the periodicity of the lattice:

$$\Psi_{n,\vec{k}}(\vec{r}) = \exp(i\vec{k} \cdot \vec{r}) \cdot u_{n,\vec{k}}(\vec{r}) \quad (6.1)$$

The first index n is called *band index* and the second discrete index \vec{k} is obviously a *wave vector*. The possible wave vectors can be limited within the first Brillouin zone of this lattice. For germanium, this turns out to be a Wigner-Seitz cell as shown in Fig. 6.3a. Standard labels of the symmetry points and axis of this particular type of cell are indicated.

The \vec{k} -dependence of the energy $\epsilon_n(\vec{k})$ associated with a fixed index n varies continuously with \vec{k} and is a periodic function over the reciprocal lattice. This explains the origin of the energy band structure indexed with n . A part of the band structure of germanium is shown in Fig. 6.3b (see also [54, p.570]). The whole band structure would be a 4D graph. Therefore the band structure is traditionally only shown at symmetry points of the Brillouin zone and on the line in \vec{k} space which connects them. The labels

on the k -axis correspond to the symmetry points indicated in Fig. 6.3a.

Even for high external fields, interactions with the lattice vibrations (*phonons*) will prevent that energy levels can be reached far from equilibrium. In Fig. 6.3b, only the band structure in the close vicinity of the energy gap is of importance (locations where free electrons and holes are situated are indicated). The particular shape of these energy bands near these extrema predict preferential directions in which the electrons and holes are easier to accelerate by external fields through *effective masses* [54, p.228, 568]. It is the dependency of these effective masses upon the lattice orientation which forms the basis for the observed anisotropic mobilities.

For a fixed electrical field strength, both the projection of the drift velocity in the field direction and the drift component perpendicular to the field is depending on the field orientation with respect to the crystal lattice. The drift velocity anisotropy in both components are referred to as *longitudinal anisotropy* and *transverse anisotropy* respectively.

Due to the crystal lattice symmetry in germanium, in three directions – the crystallographic $\langle 100 \rangle$, $\langle 110 \rangle$ and $\langle 111 \rangle$ directions – the mobility however always has to be aligned with the electrical field: If the electrical field is oriented along a symmetry axis, the crystal plus field becomes invariant under a specific rotation. Therefore, the drift velocity necessarily also has to show this invariance. Consequently, the drift velocity has to be aligned with the symmetry axis.

Along symmetry directions, we therefore obtain direct information on the longitudinal anisotropy. Experimental data on the longitudinal anisotropy v_l in these specific directions can be found in literature. This mobility data can be well fitted in any principal crystallographic direction l with the parametrization reported by Knoll [31, p.423]:

$$v_l = \frac{\mu_0 E}{(1 + (\frac{E}{E_0})^\beta)^{\frac{1}{\beta}}} - \mu_n E \quad (6.2)$$

At low fields, the mobility becomes isotropic and therefore the mobility fit parameter μ_0 is expected to become independent of the crystallographic direction. For hot electrons, the departure from a linear $v_l - E$ relation is modeled through the parameters E_0 and β . At high fields, Mihailescu et al. [58] have added the term $\mu_n E$ to account for the *Gunn effect* that was observed by Ottaviani et al. [59] for field strengths above 3 kV/cm at 80 K. However, this effect is insignificant in our detector operating with field strengths (0.1-3 kV/cm) below the critical field strength as seen from Fig. 6.1. Therefore, this term is not necessary. Parametrization values on experimental longitudinal anisotropy data are summarized in Table 6.1.

The parametrization given in Table 6.1 does not only fix the mobility in two distinct directions of the electrical field but it determines the mobility in any direction. The anisotropy in the general case is related to the longitudinal anisotropy in the $\langle 111 \rangle$ and $\langle 100 \rangle$ direction and is in fact completely

specified by the latter. For the electron mobility, this relationship will be subject of the next chapter. For the hole mobility, a new model is presented in chapter 8 which establishes a similar relation.

Electron mobility parameters (μ in [$\frac{cm^2}{Vs}$])								
	$\langle 100 \rangle$ direction				$\langle 111 \rangle$ direction			
Ref.	μ_0	β	$E_0[\frac{V}{cm}]$	μ_n	μ_0	β	$E_0[\frac{V}{cm}]$	μ_n
A: [58]	40180	0.72	493	589	42420	0.87	251	62
B: ch. 9	38609	0.805	511	-171	38536	0.641	538	510

Hole mobility parameters (μ in [$\frac{cm^2}{Vs}$])								
	$\langle 100 \rangle$ direction				$\langle 111 \rangle$ direction			
Ref.	μ_0	β	$E_0[\frac{V}{cm}]$	μ_n	μ_0	β	$E_0[\frac{V}{cm}]$	μ_n
C: [60]	66333	0.744	181	-	107270	0.580	100	-
D: ch. 10	61824	0.942	185	-	61215	0.662	182	-

Table 6.1: An overview of charge carrier mobility data in Ge at 78 K. The fit parameters to Eq. 6.2 for the electron and hole mobility along the $\langle 100 \rangle$ and the $\langle 111 \rangle$ direction are presented. The parameters obtained from the data by Reggiani et al. [60] correspond to the fit shown in Fig. 8.3. Also data obtained through the characterization methods explained in chapters 9, 10 are listed.

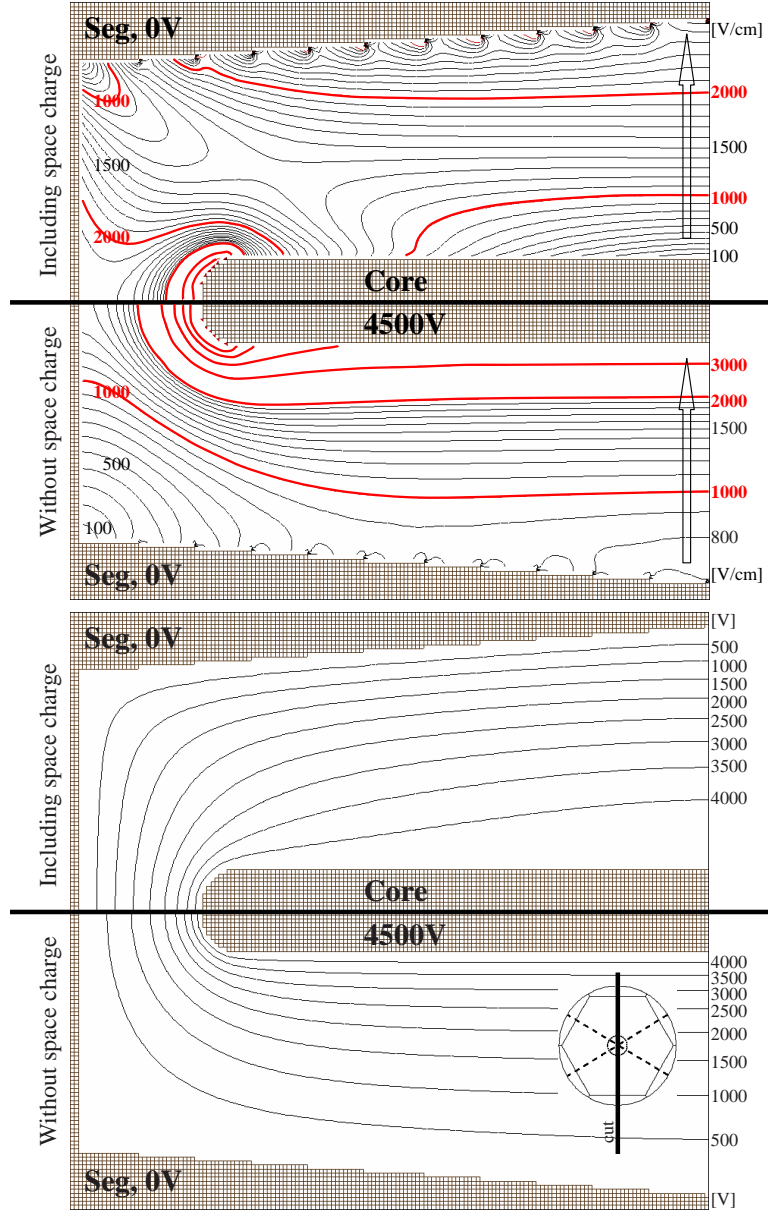


Figure 6.1: Calculated electrical field and potential in a MINIBALL detector. Top: Comparison between the electrical field strength with and without space charge. The arrows indicate the reversal in the gradient of the electrical field strength by the space charge. Bottom: The corresponding equipotential lines demonstrating the influence of the space charge on the potential.

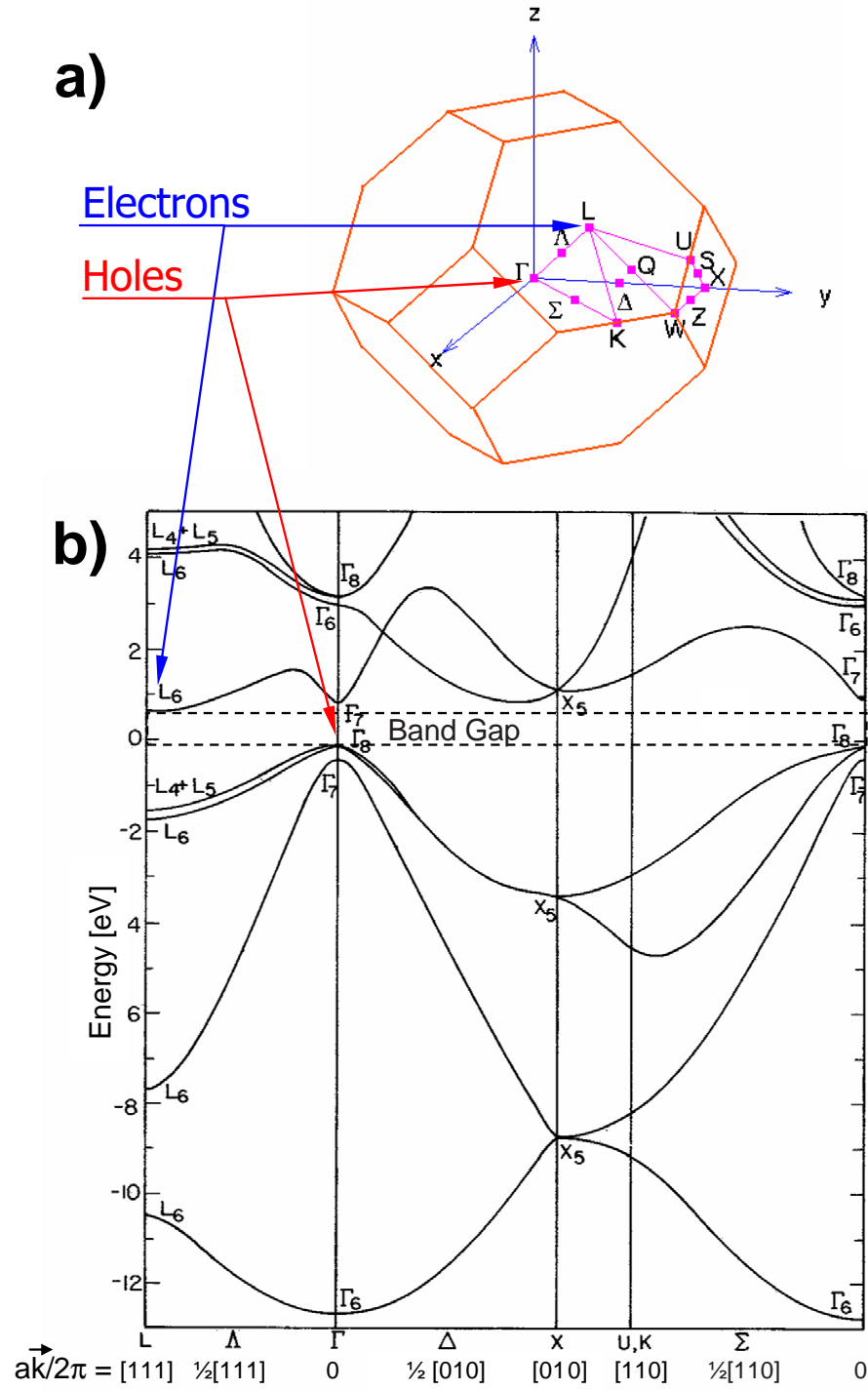


Figure 6.3: a): The first Brillouin zone in germanium. Standard labels of symmetry points and axis of the cell are indicated (see [57, p.199]). b): The germanium band structure. Band gap, conduction band minimum and valence band maximum are indicated [57, p.229]. a corresponds to the lattice constant of 5.66 Å.

Chapter 7

Electron Mobility Model

In this chapter, it will be described how the electron mobility parametrization for specific crystallographic directions can be used to predict the electron drift velocity at any field strength and at any orientation of the field with respect to the crystal lattice orientation. The model described here is owing to Nathan [61] and dates back to the 1960's. As presented here, it deviates slightly from the implementation as described by Mihailescu et al. [58] with regard to the treatment of the valley population.

7.1 Layout of the model

For the germanium band structure, the electrons are populating eight half ellipsoidal shaped valleys near the edge of the Brillouin zone along the four equivalent $\langle 111 \rangle$ directions as shown in Fig. 7.1 and Fig. 6.3b. With a suitable choice of primitive cell in k -space these can be represented as four valleys, the half ellipsoids on opposite faces in Fig. 7.1 being joint together [54, p.570]. For each of these four valleys $i \in [1 \dots 4]$, one can apply a linear transformation $\vec{k}_i^* = \alpha_i^{1/2} \vec{k}$ on the wave vectors \vec{k} such that in the new coordinate system the ellipsoid valley i is converted into a spherical valley. The tensor α_i is called the electron effective mass tensor. This tensor becomes diagonal when the coordinate axis is chosen to coincide with the

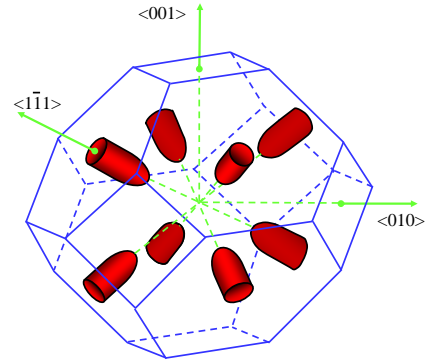


Figure 7.1: Germanium has eight equivalent minima in the conduction band, situated at the edge of the Brillouin zone. A surface of constant energy is shown to reveal the ellipsoidal shape of the valleys around these minima.

principal axis of the elliptic valley under consideration. In general the tensor α_i is given in terms of the rotation matrices R_i , responsible for aligning the y-axis of the lab system with the i -th $\langle 111 \rangle$ axis by:

$$\alpha_i = R_i^T \cdot \begin{pmatrix} m_t^{-1} & 0 & 0 \\ 0 & m_l^{-1} & 0 \\ 0 & 0 & m_t^{-1} \end{pmatrix} \cdot R_i \quad (7.1)$$

The mass values for $m_l = 1.64$ and $m_t = 0.0819$ were taken according to Mihailescu et al. [58]. The electrical field and the drift velocity transform then as $\vec{E}_i^* = \alpha_i^{1/2} \vec{E}$ and $\vec{v}_i^* = \alpha_i^{-1/2} \vec{v}$ (see [62, p.187]).

Since in \vec{k}_i^* -space, the valley i becomes spherical, the mobility relation for this valley in its mass-transformed frame takes on the isotropic form [62, 63]

$$\vec{v}_i^*(\vec{E}) = -\mu^*(E_i^*) \vec{E}_i^* \quad (7.2)$$

in which $\mu^*(E^*)$ is a scalar quantity only depending on the amplitude of the effective field strength E^* . The minus sign makes the electrons flow in the opposite direction of the applied electrical field.

In \vec{k} -space, the total drift velocity \vec{v}_d becomes the weighted average of the drift velocities associated with the individual valleys. The drift velocity \vec{v}_i of valley i contributes $\vec{v}_i = -\mu^*(E_i^*) \alpha_i \vec{E}$, weighted by the relative population n_i of this valley ($\sum_{i=1}^4 n_i = 1$). The total drift velocity thus yields:

$$\vec{v}_d(\vec{E}) = - \sum_{i=1}^4 n_i \mu^*(E_i^*) \alpha_i \vec{E} \quad (7.3)$$

7.2 Parametrization of the model

It is now possible to identify the effective mobility with the v_{100} drift velocity. When the field is oriented along the $\langle 100 \rangle$ axis, all four valleys are identically oriented with respect to the field as seen in Fig. 7.1. Due to this symmetry, all n_i are thus equal to 1/4. Identifying v_{100} with Eq. 7.3 for this specific direction then yields

$$\mu^*(E) = \frac{v_{100}(E/\Gamma_0)}{\Gamma_0 E} \quad (7.4)$$

in which the constant $\Gamma_0 = 2.888$ is defined by the mass tensor elements in Eq. 7.1.

In general, the population of the valleys is governed by the intervalley scattering rate $\nu(E_i^*)$. The equilibrium valley population can be expressed as

$$n_i = \frac{\nu(E_i^*)^{-1}}{\sum_{k=1}^4 \nu(E_k^*)^{-1}} \quad (7.5)$$

Nathan [61] experimentally observed at intermediate field strengths the power dependence

$$\nu(E) \propto E^\eta \quad (7.6)$$

with $\eta = 0.87$, while Reik et al. [64] derived for Maxwellian electron distributions the theoretical upper limit $\eta = 1$. For its parametrization, a log-linear electric field dependence is satisfactory:

$$\eta(E) = \eta_0 + b \ln(E/E_{ref}) \quad (7.7)$$

The parameters η_0 and b in Eq. 7.7, together with the parametrization of the v_{100} through Eq. 7.4 completely defines the electron mobility variation given by Eq. 7.3. The values obtained from our detector yielded: $\eta_0 = 0.496$, $b = 0.0296$ for $E_{ref} = 1200$ V/cm while the v_{111} experimental data from Mihailescu et al. [58] could be well reproduced in the region of interest (100-3000 V/cm) with the fit parameters $\eta_0 = 0.422$, $b = 0.201$ for $E_{ref} = 1200$ V/cm.

The rather large differences in η predicted by the different data suggest the necessity for experimental determination of these parameters for detectors with different purity separately rather than to rely on literature data. The same conclusion can be drawn from Schweitzer et al. [65], which studied the excess n_1 of the cold valley 1 over a uniform distribution $n_i = n_0 = 1/4$ for the case in which the field is aligned with the $\langle 111 \rangle$ direction of valley 1. In this case, the three hot valleys are equally strong populated with an amount of $(1 - n_1)/3$. Identification of Eq. 7.3, in specific for the $\langle 111 \rangle$ direction of valley 1, yields an expression for $n_1(E)$:

$$n_1(E) = \frac{v_{111}(E) - \Gamma_2^2 \mu^*(\Gamma_2 E) \cdot E}{\Gamma_1^2 \mu^*(\Gamma_1 E) \cdot E - \Gamma_2^2 \mu^*(\Gamma_2 E) \cdot E} \quad (7.8)$$

In which again $\Gamma_1 = 0.7809$ and $\Gamma_2 = 3.305$ are constants defined by the mass tensor elements in Eq. 7.1. The study of Schweitzer et al. was performed on n-type germanium samples with varying purity. The results – also including new data from [58] and chapter 9 – are shown in Fig. 7.2. The new $\frac{n_1 - n_0}{n_0}$ values were extracted from the electron mobility data parameters in Table 6.1 using Eq. 7.8.

The drift velocity as function of the orientation of the electrical field (for E fixed at 1200 V/cm and using the parametrization of a 12-fold segmented HPGe detector) is shown in Fig. 7.3. For the radial component, the major deviation from uniformity comes from the strong difference of the mobility along the $\langle 111 \rangle$ direction. Here it is worth mentioning that the θ and ϕ components behave differently than for the hole mobility (see for comparison Fig. 8.5). In the coaxial part of the detector, the electrical field is restricted to the $\theta = \pi/2$ plane. For such fields, the v_θ component of the drift velocity is always zero, while the v_ϕ component will always point towards the nearest $\langle 100 \rangle$ direction when following the drift velocity direction. Since electron

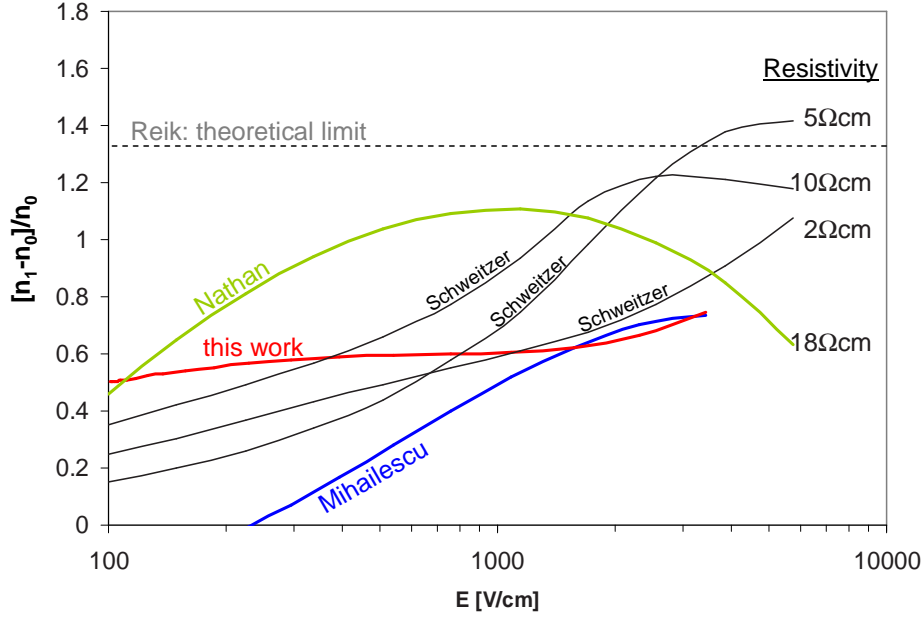


Figure 7.2: The excess in population of the cool valley 1 over a uniform population ($n_0 = 1/4$) for the case the field is aligned with the $\langle 111 \rangle$ direction. The data is taken from Schweitzer et al. [65] and corresponds to samples at 85 K. The room temperature resistivities of the samples are shown to indicate the difference in impurity concentration. Also the data from Nathan [61], Mihailescu et al. [58] and this work (Table 6.1B) are shown for comparison. The dashed line corresponds to the theoretical limit $\eta = 1$ from Reik et al. [64].

drift velocity and electrical field are opposed, the v_ϕ component will always point towards the nearest $\langle 110 \rangle$ direction when following the electrical field direction. The vectors in Fig. 7.3f illustrate this behavior. The counterclockwise orientation of the vector near 30° compared to the clockwise directed vectors at 60° and 330° is caused by the opposite sign of the v_θ component as shown in Fig. 7.3f.

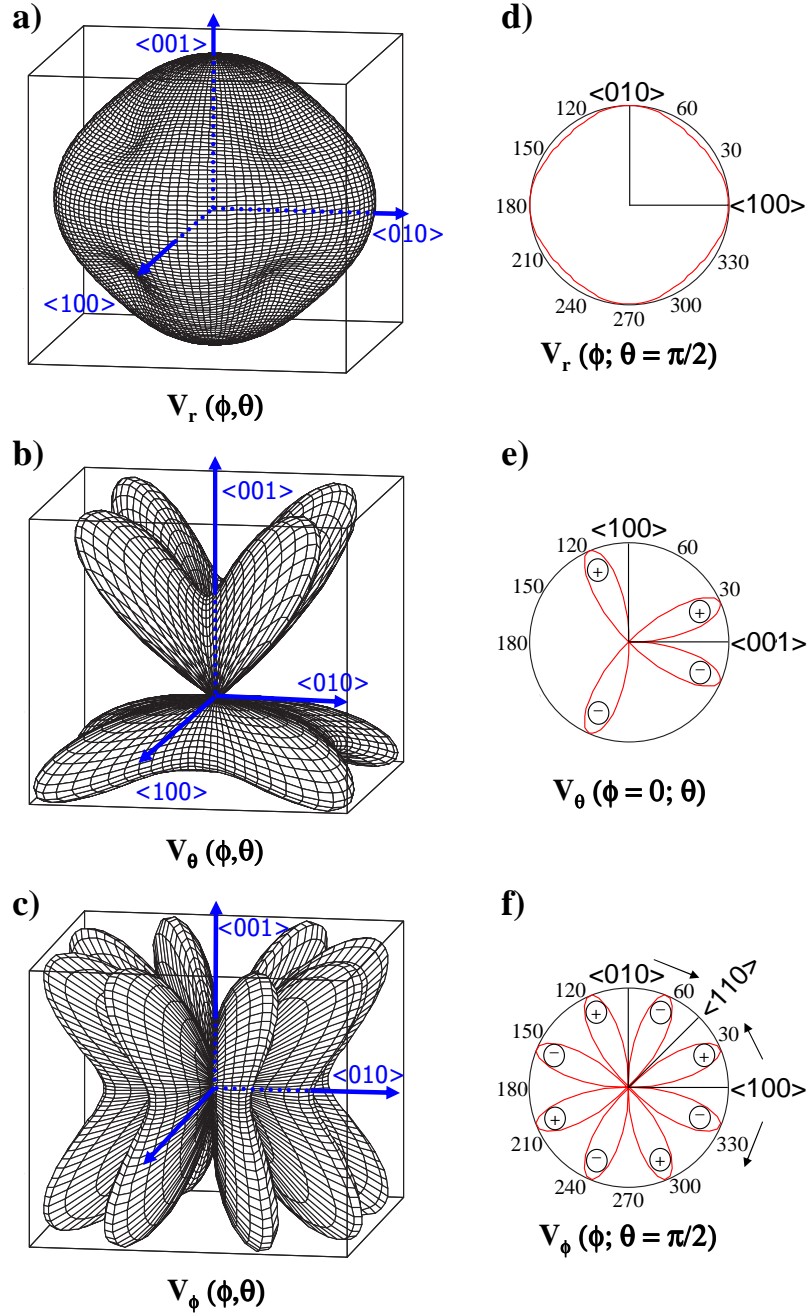


Figure 7.3: Illustration of the electron velocity components in spherical coordinates. a)-c): The radial and angular components of the total drift velocity, Eq. 7.3, plotted as function of the orientation of the electrical field. The amplitude of the electrical field was fixed at $E = 1200 \text{ V/cm}$ and the electron mobility parameters were taken from Table 6.1B. Projections are shown in the right part d)-f). Plus and minus symbols indicate the sign of the function at a specific angle.

Chapter 8

The Hole Mobility Model

In contrast to the electrons, for holes no direct applicable description of the anisotropic mobility exists in literature. This is due to the rather complicated mathematical description of the valence band near the maxima. Therefore, in the past it was more attractive to investigate the hole mobility by means of Monte-Carlo techniques. As a consequence, a model had to be developed which is applicable to our purpose.

8.1 Layout of the model

The maximum energy attainable in the valence band is found at the center of the Brillouin zone (Fig. 6.3b). The band structure in that point is twofold degenerated into a light hole ($0.04 m_0$, with m_0 the free-electron mass) and a heavy hole band ($0.3 m_0$) [62]. The heavy hole band has a warped spherical shape as shown in Fig. 8.1. Due to its smaller density of states the light hole band does not contribute substantially to the mobility. This causes that at thermal equilibrium, the hole population consists of only 4% light holes compared to 96% heavy holes (see Conwell [62, p.61]). The light hole band is close to spherical and would only contribute with an isotropic drift term. The next maximum in the valence band lies 0.29 eV lower in energy. These states cannot be populated as this energy lies

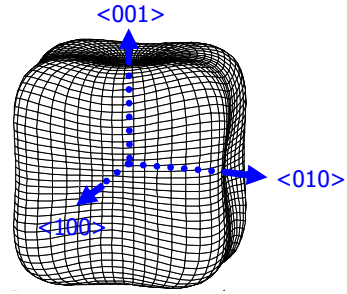


Figure 8.1: The hole mobility in germanium is governed by the region near the maximum in the heavy hole band situated at $k = 0$. A surface of constant energy of the heavy hole band is shown in k -space to reveal the warped spherical shape of this region. This surface is described by $\epsilon(\vec{k}) = \text{constant}$ using equation 8.2.

far above the threshold for emitting optical phonons. In addition, a good correspondence between simulation and experiment is achieved by only taking into account the heavy hole band in the Monte Carlo calculation performed by Reggiani et al. [60]. Therefore it is well justified that the heavy hole band is solely responsible for the anisotropic mobility.

Our new model is backed by experiments by Pinson et al. [66] and Alba et al. [67]. Since germanium has the property of being transparent to infrared light, the population of the heavy hole band could be studied by measuring the amount of light that is absorbed as a function of its wavelength. This led to the conclusion that the heavy holes, accelerated by an electric field, are trapped in the so called *streaming motion*: Since the energy loss to acoustical phonon modes are negligible, the holes are accelerated in the field until their energy becomes 0.037 eV. At that point their energy is sufficiently large to emit an optical phonon, a process which is very likely to happen. By emitting an optical phonon, the hole typically loses most of its energy as it scatters back into the near- $k = 0$ region from where it resumes acceleration in the field direction and a new cycle is started.

From this picture of streaming motion, the properties of the probability distribution function for finding a heavy hole in a specific \vec{k} -state can be predicted. The distribution should be peaking in the direction in which \vec{k} is parallel to the electrical field. As will be shown, this does not exclude the existence of a transversal anisotropy. Secondly, this distribution should drop fast to zero above the energy of the optical phonon branch at 0.037 eV.

Empirically it is found that a *drifted Maxwellian* distribution offers a good description for the measured wave vector distributions of heavy holes at field strengths in the range of 130-2150 V/cm, relevant for our Ge-detectors. This distribution takes on the form (e.g. Conwell [62, p.71])

$$f(\vec{k}; \vec{k}_0) = a \cdot \exp(-\hbar^2(\vec{k} - \vec{k}_0)^2/2mk_bT_h) \quad (8.1)$$

in which a is a normalization constant and m the heavy hole effective mass. The temperature of the holes is T_h and the mean wave vector is \vec{k}_0 . T_h was observed to be less than the lattice temperature of 77 K. The term *hot* holes is therefore somewhat misleading. The kinetic energy $\hbar^2k_0^2/2m$ associated with k_0 exceeded the thermal energy from $1.2 k_bT_h$ at 130 V/cm to $4.1 k_bT_h$ at 2150 V/cm. From the model on the streaming motion, we assume that $\vec{k}_0(k_0, \theta_0, \phi_0)$ will be aligned with the applied field. Therefore the complete distribution Eq. 8.1 is defined by only two parameters, k_0 and T_h , which will again be obtained from the v_{100} and v_{111} hole mobility data.

The model for the energy $\epsilon(\vec{k})$ dependence of heavy holes in germanium is taken from Reggiani et al. [60, 63]:

$$\epsilon(\vec{k}) = A \cdot \frac{\hbar^2k^2}{2m_0} \cdot [1 - q(\theta, \phi)] \quad (8.2)$$

in which m_0 is the free-electron mass and $A = 13.35$ is a germanium-specific constant. $q(\theta, \phi)$ describes the warping of the constant energy surfaces, and θ and ϕ are the polar and azimuthal angles of \vec{k} with respect to the frame defined by the three equivalent $\langle 100 \rangle$ axis:

$$q(\theta, \phi) = [b^2 + \frac{c^2}{4} \cdot (\sin(\theta)^4 \sin(2\phi)^2 + \sin(2\theta)^2)]^{1/2} \quad (8.3)$$

With $b = 0.6367$ and $c = 0.9820$ germanium specific parameters. Eq. 8.2, and Eq. 8.3 describe mathematically the constant energy surface shown in Fig. 8.1. The drift velocity can then be expressed by combining the distribution function of the heavy hole concentration (Eq. 8.1) and the \vec{k} dependence of a specific energy state (Eq. 8.2) yielding

$$\vec{v}_d = \frac{\hbar}{a\pi^{3/2}\sqrt{2mk_bT_h}} \int \vec{v}(\vec{k}) f(\vec{k}; \vec{k}_0) d\vec{k} \quad (8.4)$$

in which $\vec{v}(\vec{k})$ is the velocity associated with a specific \vec{k} -state:

$$\vec{v}(\vec{k}) = \frac{1}{\hbar} \vec{\nabla}_k \epsilon(\vec{k}) \quad (8.5)$$

The gradient $\vec{\nabla}_k \epsilon(\vec{k})$ is thus according to Eq. 8.5 in its spherical coordinates given by:

$$\begin{aligned} \vec{\nabla}_k \epsilon_k &= \frac{A\hbar^2 k}{m_0} (1 - q(\theta, \phi)) \\ \vec{\nabla}_k \epsilon_\theta &= \frac{-c^2 A\hbar^2 k}{8m_0 q(\theta, \phi)} (2 \sin(\theta)^3 \cos(\theta) \sin(2\phi)^2 + \sin(4\theta)) \\ \vec{\nabla}_k \epsilon_\phi &= \frac{-c^2 A\hbar^2 k}{8m_0 q(\theta, \phi)} \sin(\theta)^3 \sin(4\phi) \end{aligned} \quad (8.6)$$

8.2 Theoretical results on the hole model

The numerical evaluation of the three dimensional integral in Eq. 8.4 is still very computer time consuming. Fortunately, the k -dependence can be integrated over explicitly and only a double integration remains to be performed. To simplify the notation, the constant factor $\hbar/\sqrt{2mk_bT_h}$ in Eq. 8.1 will be absorbed in the definition of k and k_0 throughout the rest of the text. In this way, k_0 could be physically interpreted as a solid-state equivalent to the Mach number in fluid mechanics.

In order to perform the integration in Eq. 8.4, the integrand need to be expressed in Cartesian coordinates. Eq. 8.4 can then be written more

explicitly as:

$$\begin{aligned}
 v_x(\vec{k}_0) &= \frac{v_{100}(k_0)}{n(k_0)} \int_0^{2\pi} \int_0^\pi X(\theta, \phi) \exp[k_0^2(R^2 - 1)] I_3(k_0 R) \sin(\theta) d\theta d\phi \\
 v_y(\vec{k}_0) &= \frac{v_{100}(k_0)}{n(k_0)} \int_0^{2\pi} \int_0^\pi Y(\theta, \phi) \exp[k_0^2(R^2 - 1)] I_3(k_0 R) \sin(\theta) d\theta d\phi \\
 v_z(\vec{k}_0) &= \frac{v_{100}(k_0)}{n(k_0)} \int_0^{2\pi} \int_0^\pi Z(\theta, \phi) \exp[k_0^2(R^2 - 1)] I_3(k_0 R) \sin(\theta) d\theta d\phi
 \end{aligned} \tag{8.7}$$

of which the functions $n(k_0)$, R , (X, Y, Z) and I_3 are defined as follows: The common first factor was written in a special form to indicate that the normalization constant $n(k_0)$ can be found by identification of $v_x(k_0, \theta = \pi/2, \phi = 0)$ with the $v_{100}(k_0)$ mobility. R is used as an abbreviation for the cosine of the angle between \vec{k} and \vec{k}_0 :

$$R(\theta, \phi; \theta_0, \phi_0) = \frac{\vec{k}}{k} \cdot \frac{\vec{k}_0}{k_0} = \sin(\theta_0) \sin(\theta) \cos(\phi - \phi_0) + \cos(\theta_0) \cos(\theta) \tag{8.8}$$

and the vector $k[X(\theta, \phi), Y(\theta, \phi), Z(\theta, \phi)]$ represents the gradient $\vec{\nabla}_k \epsilon(\vec{k})$ expressed in Cartesian coordinates. Its k -dependence is absorbed in the integral I_3 . For completeness, the expression for X, Y, Z then takes the form:

$$\begin{aligned}
 kX(\theta, \phi) &= \vec{\nabla}_{\epsilon_k} \cos(\phi) \sin(\theta) + \vec{\nabla}_{\epsilon_\theta} \cos(\phi) \cos(\theta) - \vec{\nabla}_{\epsilon_\phi} \sin(\phi) \\
 kY(\theta, \phi) &= \vec{\nabla}_{\epsilon_k} \sin(\phi) \sin(\theta) + \vec{\nabla}_{\epsilon_\theta} \sin(\phi) \cos(\theta) + \vec{\nabla}_{\epsilon_\phi} \cos(\phi) \\
 kZ(\theta, \phi) &= \vec{\nabla}_{\epsilon_k} \cos(\theta) - \vec{\nabla}_{\epsilon_\theta} \sin(\theta)
 \end{aligned} \tag{8.9}$$

The function $I_3(k_0 R)$ includes all k -dependency of the integration. This type of integral is a special case of the family of integrals given in Eq. 8.10 for which an explicit solution is derived. A simple solution to the family of integrals of the type

$$I_n(x) = \int_0^\infty k^n \exp(-(k-x)^2) dk \tag{8.10}$$

was found by taking the derivative of Eq. 8.10 on both sides, which yields the iterative relation:

$$I_{n+1}(x) = xI_n(x) + \frac{1}{2} \frac{d}{dx} I_n(x) \tag{8.11}$$

By employing the error function $\text{erf}(x)$, the first component is identified with $I_0(x) = \sqrt{\pi}/2(1 + \text{erf}(x))$ and $dI_0(x)/dx = \exp(-x^2)$. The following

explicit expressions for the first members of the solution to integral Eq. 8.10 are obtained:

$$\begin{aligned}
I_0(x) &= \frac{\sqrt{\pi}}{2}(1 + \operatorname{erf}(x)) \\
I_1(x) &= \frac{\sqrt{\pi}}{2}x(1 + \operatorname{erf}(x)) + \frac{1}{2}\exp(-x^2) \\
I_2(x) &= \frac{\sqrt{\pi}}{2}(x^2 + \frac{1}{2})(1 + \operatorname{erf}(x)) + \frac{1}{2}x\exp(-x^2) \\
I_3(x) &= \frac{\sqrt{\pi}}{2}(x^3 + \frac{3x}{2})(1 + \operatorname{erf}(x)) + \frac{1}{2}(x^2 + 1)\exp(-x^2) \\
I_4(x) &= \frac{\sqrt{\pi}}{2}(x^4 + 3x^2 + \frac{3}{4})(1 + \operatorname{erf}(x)) + \frac{1}{2}(x^3 + \frac{5x}{2})\exp(-x^2)
\end{aligned} \tag{8.12}$$

An alternative and non-recursive solution to Eq. 8.10 was found by substitution of $y = k - x$ and by expanding the term $(y + x)^n$ in its binomial form. The following general solution is obtained:

$$I_n(x) = \frac{1}{2} \sum_{m=0}^n \binom{n}{m} x^{n-m} [\Gamma(\frac{m+1}{2}) + (-1)^m \cdot \operatorname{sgn}(x) \cdot \gamma(\frac{m+1}{2}, x^2)] \tag{8.13}$$

which expresses that, using the sign function sgn , the integral can be expanded in terms of the complete and incomplete gamma functions $\Gamma(x)$ and $\gamma(x, y)$, respectively.

Besides the integral I_3 , also other integrals of the type I_n show up naturally when taking other momenta of the distribution Eq. 8.1. For example in calculating the average hole energy, the integral I_4 would be needed.

8.3 A practical approximation

Although the numerical evaluation of the two-dimensional integral in Eq. 8.7 is feasible, its implementation in a simulation code would still slow down the computation considerably. Therefore a fit function had to be found for this integral. The following functions, inspired by Eq. 8.6, provide a good approximation for Eq. 8.7 for k_0 in the range of interest ($k_0 < 3$) using the $\vec{k}_0(k_0, \theta_0, \phi_0)$ components of the mean wave vector (which has the same orientation as the electrical field $\vec{E}(E, \theta_0, \phi_0)$):

$$\begin{aligned}
v_r &= v_{100}(E)[1 - \Lambda(k_0)(\sin(\theta_0)^4 \sin(2\phi_0)^2 + \sin(2\theta_0)^2)] \\
v_\theta &= v_{100}(E)\Omega(k_0)[2\sin(\theta_0)^3 \cos(\theta_0) \sin(2\phi_0)^2 + \sin(4\theta_0)] \\
v_\phi &= v_{100}(E)\Omega(k_0)\sin(\theta_0)^3 \sin(4\phi_0)
\end{aligned} \tag{8.14}$$

The functions Λ and Ω correspond to the relative difference in radial velocity $\Lambda = [v_{100} - v_{110}]/v_{100}$ and the relative tangential velocity $\Omega = v_\phi(\phi_0 = \frac{\pi}{8}; \theta_0 = \frac{\pi}{2})/v_{100}$. They govern the amplitude of the anisotropy.

Their dependence on the mean wave number k_0 was obtained by fitting Eq. 8.14 to the true solution, Eq. 8.7. This yielded:

$$\Lambda(k_0) = -0.01322k_0 + 0.41145k_0^2 - 0.23657k_0^3 + 0.04077k_0^4 \quad (8.15)$$

$$\Omega(k_0) = 0.006550k_0 - 0.19946k_0^2 + 0.09859k_0^3 - 0.01559k_0^4 \quad (8.16)$$

The choice of the reduced k_0 value still has to be related to the experimentally observed longitudinal anisotropy. To do so, it is assumed that for fixed electrical field strengths, k_0 is independent of the field orientation such that to first order, k_0 is function of $|E|$ only. Indications for this are the relatively small differences observed by Pinson et al. [66, Fig.13] at 800 V/cm between the experimentally determined distributions for fields aligned with the $\langle 111 \rangle$ and $\langle 100 \rangle$ directions. Also the nearly orientation independent power loss [66, Fig.16] to both acoustical and optical phonons is a further indication. By evaluating the coordinates for the special case of the $\langle 111 \rangle$ direction in Eq. 8.14, the expression

$$1.33\Lambda(k_0) = [v_{100} - v_{111}]/v_{100} \quad (8.17)$$

is obtained. Eq. 8.17, in combination with Eq. 8.15 gives us implicitly k_0 as function of $v_{rel} = v_{111}/v_{100}$. For the region of interest (the fit was performed for k_0 in the range between 0.3 and 1.5), this dependence can be expressed explicitly by:

$$k_0(v_{rel}) = 9.2652 - 26.3467v_{rel} + 29.6137v_{rel}^2 - 12.3689v_{rel}^3 \quad (8.18)$$

This provides a usefull relationship to deduce k_0 from experimental values as listed in Table 6.1.

The low field isotropic limit is well predicted by the model. For low fields, Λ and Ω approach zero in Fig. 8.2 as k_0 becomes small and therefore the model becomes isotropic as the distribution Eq. 8.1 becomes Maxwellian again ($k_0 = 0$). The mobility behavior at high fields can be tested on the experimental v_{110} data. The ratio between Λ and Eq. 8.17 in the approximation to the true solution becomes independent of k_0 :

$$\frac{v_{100} - v_{111}}{v_{100} - v_{110}} = 1.33 \quad (8.19)$$

This relation was verified in Fig. 8.3 where the models prediction on the v_{110} is compared to the experimental data from Reggiani et al. [60]. Also the best fit corresponding to the values in Table 6.1B are shown for the other two crystallographic directions. Good agreement is achieved between experiment and the model description.

It is worth mentioning that the data from Reggiani et al. was obtained under optimized laboratory conditions employing thin germanium samples (0.2 ... 0.8 mm) which were specially prepared and cut with respect to their

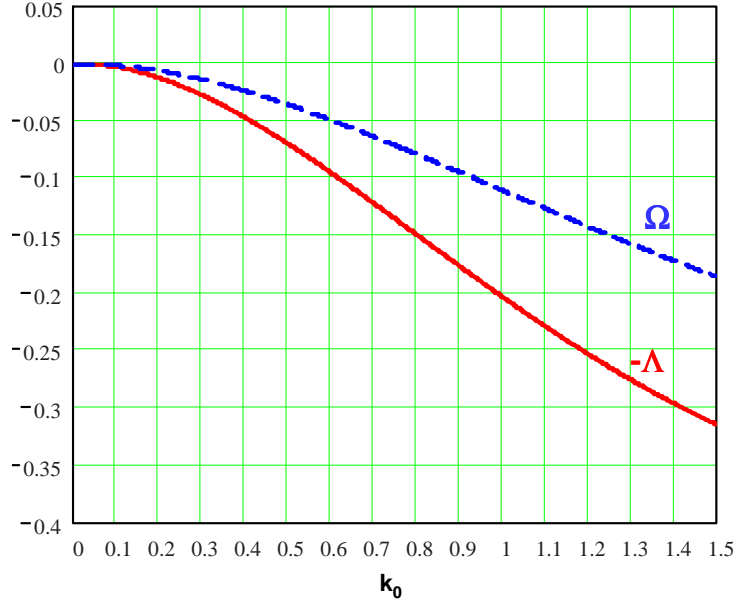


Figure 8.2: The relative velocity $-\Lambda = [v_{110} - v_{100}]/v_{100}$ and $\Omega = v_\phi(\phi_0 = \frac{\pi}{8}; \theta_0 = \frac{\pi}{2})/v_{100}$ as function of the reduced parameter k_0 demonstrating the increase of anisotropy as a function of k_0 .

crystallographic axes. A dedicated measuring technique using a pulsed-bias voltage was applied. Such conditions are very different from the situation applicable to the characterization of a HPGe detector. Also the analysis method using Monte-Carlo techniques is inapplicable to data obtained from a tapered, large volume HPGe detector crystal. For that purpose, analytical solutions as described here remain useful.

Huge differences between the two hole velocity parametrizations from Table 6.1 are obvious by comparing the k_0 dependence as a function of the electrical field strength Eq. 8.18 (see Fig. 8.4). The corresponding k_0 values to the experimental data by Alba [67] were also included in the graph. The large differences in Fig. 8.4 illustrate that hole mobility literature data may not be adequate for simulation of a specific detector to high precision. There is clearly a need for detector specific measurements.

8.4 Comparison with the electron mobility model

To demonstrate the differences between the hole mobility model and the electron mobility model, the variation of Eq. 8.14 with electrical field orientation is shown in Fig. 8.5. The value k_0 was taken to be 0.8, which according to Fig. 8.4 corresponds to $E = 1200 \text{ V/cm}$ for a large volume HPGe detector. For holes, mainly the drift velocity along the $\langle 100 \rangle$ is faster than in other

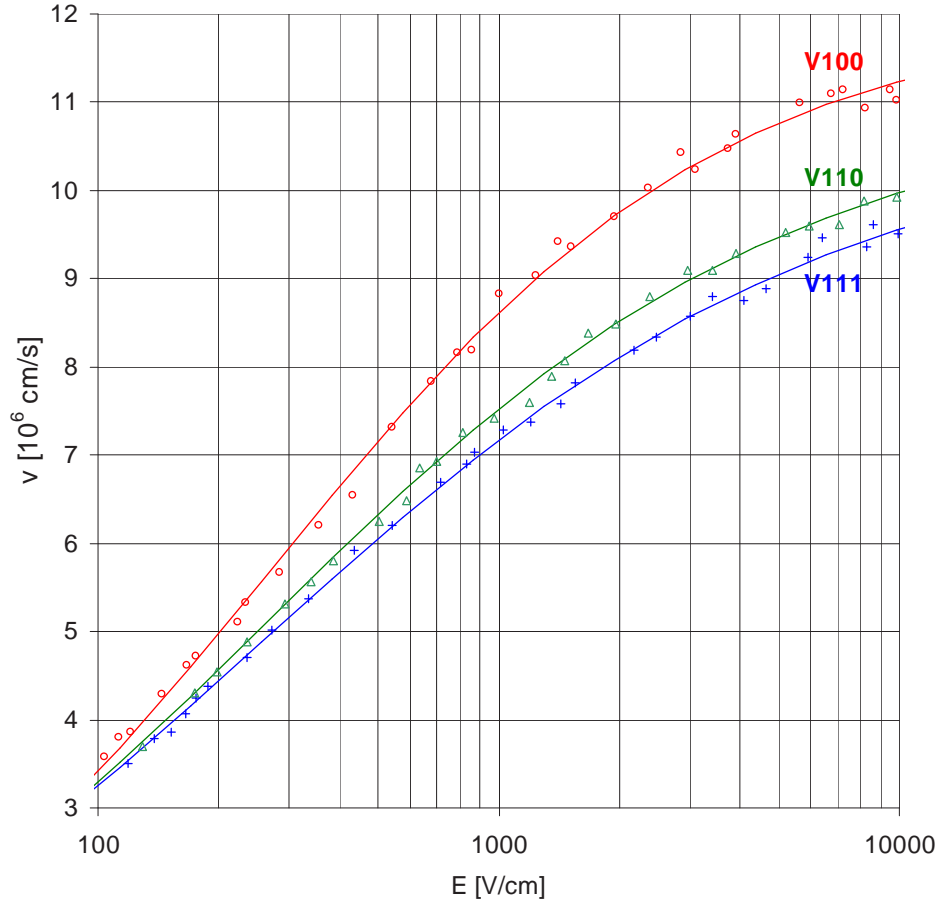


Figure 8.3: Experimental data on the drift velocity along the three crystal symmetry axis as taken from [60]. The longitudinal velocity component is clearly anisotropic. The solid lines to the v_{100} and v_{111} data correspond to the optimum fit obtained using Eq.6.2. The values obtained by the fit are listed in Table 6.1. The solid line through the v_{110} data is the prediction by our model and using the v_{100} and v_{111} fitted curves.

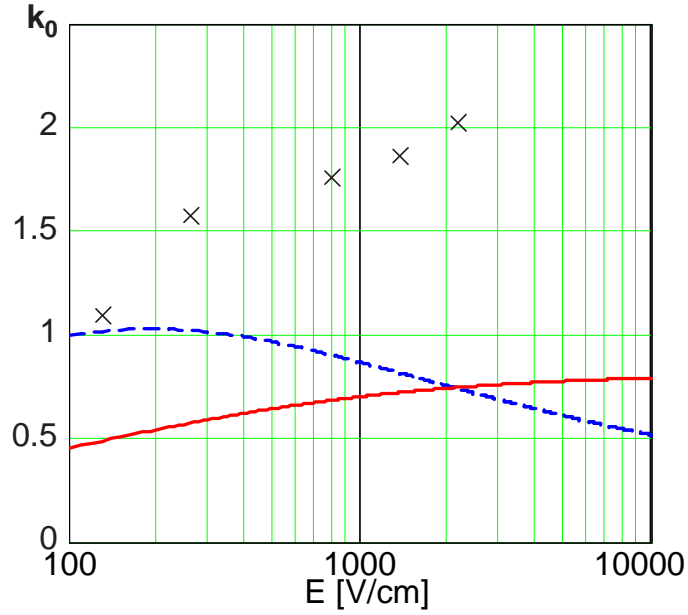


Figure 8.4: The reduced k_0 parameter as function of the field strength according to the data taken from [60] (solid line) and from Table 6.1D (dashed line). The single points correspond to the five values quoted in [67].

directions, which gives rise to the cubic shape of the radial drift velocity component in Fig. 8.5a. Compared to Fig. 7.3a, this is a major difference between hole and electron longitudinal anisotropy.

Also the tangential velocity anisotropy $v_t = \sqrt{v_\theta^2 + v_\phi^2}$ behaves remarkably different. The electron and hole tangential velocity anisotropy is plotted as a function of the field orientation in Fig. 8.6. The amplitude variations of the hole tangential components are oriented along the $\langle 100 \rangle$ directions, while for the electron tangential anisotropy, the $\langle 111 \rangle$ directions play a similar role.

In the coaxial part of the detector, the hole tangential velocity component behaves identical to the electron tangential velocity component. In both cases, the v_θ component is zero and, when following the direction of the drift velocity, a v_ϕ component is present, which in both cases points towards the nearest $\langle 100 \rangle$ direction. The inversions in graph Fig. 8.5b,c,e,f with respect to Fig. 7.3b,c,e,f is due to the fact that holes and electrons move in the opposite directions.

Both the electron and hole velocity anisotropy in HPGe detectors create measurable rise time effects and are therefore relevant to pulse shape analysis.

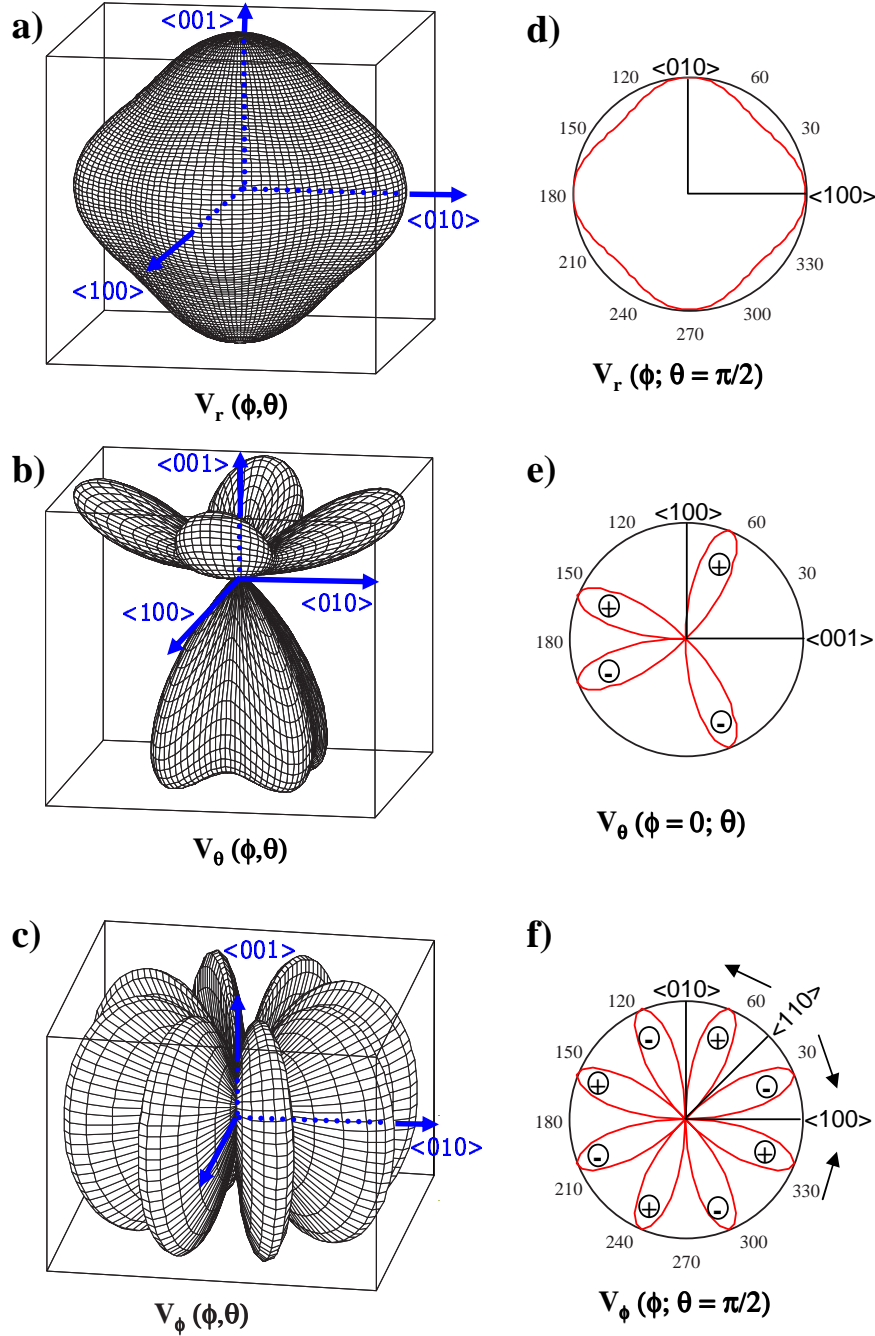


Figure 8.5: The angular dependence of the hole velocity on the electrical field orientation. a-c: The radial and angular velocity components of Eq. 8.14 plotted as a function of the orientation of the electrical field. The amplitude of the electrical field was fixed at $E = 1200 \text{ V/cm}$ and the hole mobility parameters were taken from Table 6.1D, which yield $k_0 = 0.8$ (see Fig. 8.4). Projections are shown in the lower part d-f. Plus and minus symbols indicate the sign of the function for a specific angle.

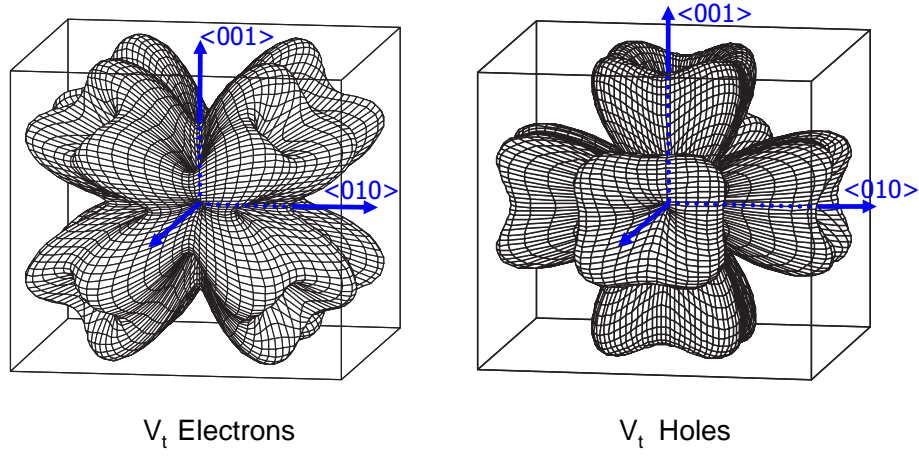


Figure 8.6: A comparison between the tangential velocity anisotropy as calculated from equation 7.3 for the electron mobility and equation 8.14 for the hole mobility.

Chapter 9

Electron Mobility Results

In this chapter, it will be described how the electron mobility in the detector and the space charge distribution can be characterized. The detector crystal orientation has traditionally been derived from electron rise time measurements, performed for source positions at a fixed radius at the front side of the detector. Our interests lie beyond the determination of the crystal orientation only. Consequently, the data acquisition, employing time resolved digital electronics and data analysis, is more involved.

9.1 The Measurement

To obtain information on the electron mobility, trace data was taken using 59.5 keV γ -rays from a ^{241}Am source at the outer surface of the germanium crystal. A small 7 mm thick collimator with a 1.5 mm hole was used. This was adapted to fit the cylindrical detector end cap and to facilitate precise positioning of the collimator holder. Since 59.5 keV γ -rays only penetrate the germanium about 1 mm before the gamma is absorbed, these events offer a way to create well localized photopeak interactions close to the outer electrodes using a light and easy to handle collimator setup. For these events the holes will be collected immediately such that the charge signals obtained only provide information on the electron movement towards the core. The drawback of the procedure is the very low γ -ray energy and the considerable noise in these signals requiring the averaging procedure described in chapter 5.2.

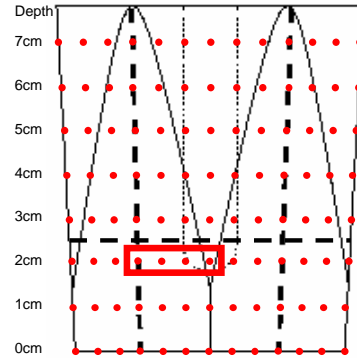


Figure 9.1: Data points taken for the electron mobility characterization. Eight depths were scanned in steps of 10°. The data in the square are shown in Fig. 9.6.

The electron mobility data set consist of a scan of the detector surface in steps of 10° around its axis of symmetry for fixed depths as shown in Fig. 9.1. The depth of the scans was varied in steps of 10 mm starting from the detector front (0 mm depth). This yielded a total amount of 42 averaged traces (positions at segmentation lines can be evaluated twice) at 8 depths. This scanning procedure is very fast. Averages are built on several thousand events per position.

9.2 Rise Time Fit Functions

First the rise time variation with respect to the angle was studied, as shown in Fig. 9.3. To treat the data in a quantitative way, simple fit functions were introduced with a clear physical interpretation. An observable for the time elapsed between creation and collection of the electrons is the 10% – 90% rise time for the core signal. This is a good measure for the average radial drift velocity. The variation of the rise times with angle behaves like

$$\Delta t = A(1 + R_{an} \cos(4(\theta - \theta_0)))(1 + R_{geo} \cos(6\theta)) \quad (9.1)$$

The first factor describes the effects due to the electron mobility anisotropy, which should have a four fold symmetry and a phase shift θ_0 relative to the second term defining the crystal orientation. The second term accounts for the semi-hexagonal cut shape of the detector and is expected to show a six fold symmetry.

For some data, a very small and barely measurable dipole seemed to be present in the data. Therefore Eq. 9.1 was extended with the additional factor $(1 + R_{di} \cos(2(\theta - \theta_{di})))$. Such effect could be due to a misalignment of the core electrode, an off axis mounting of the crystal in the end cap or, as was observed for the holes, an anisotropy enhanced space charge effect. The measured amplitudes R_{di} in the electron rise time data however were so small (usually $< 2\%$) that the results will not be discussed further.

To detect possible radial gradients in the drift velocity, partial rise times were investigated. As the core weighting field is reduced to about 30% in the middle between core and segment electrodes as shown in Fig. 9.2a), the 5% – 30% rise times and the 40% – 90% rise times of the core signals were separately investigated. These partial rise times were well described and fitted using Eq. 9.1.

However, the partial rise times observed on the collecting segments behave different as a result of the strong angular dependence of the weighting potential. In Fig. 9.2 the weighting equipotential lines for the segments are compared to corresponding core lines. Due to the difference in weighting potential, the segment partial rise times are shifted with respect to the core partial rise times and corresponding segment rise times are given by the 10% – 60% and 70% – 95% amplitude references. Since the segment

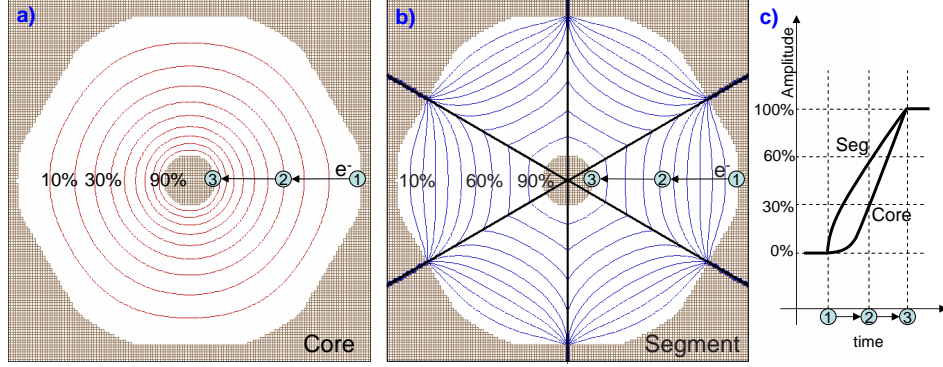


Figure 9.2: a): Calculation of ten equidistant equipotential lines of the core weighting potential in the coaxial part of the detector. b): A calculation for the hit segments. For an electron, starting at the detector surface (position 1), the rise time profiles of core and hit segment will resemble c). The core and segment signal value in the mid-detector region (position 2) reach respectively 30% and 60% of their maximum amplitude due to the corresponding weighting potential values in a), b).

equipotential lines are modulated more as $|\sin(3\theta)|$ rather than the $\cos(6\theta)$ geometrical dependence, the 10% – 60% and 70% – 95% rise times of the segment were found to be well described by the function

$$\Delta t = A(1 + R_{an} \cos(4(\theta - \theta_0)))(1 + R_{geo} |\sin(3\theta)|) \quad (9.2)$$

This causes the segment rise times to have a discontinuous derivative close to the segmentation lines. Remark that R_{geo} in Eq. 9.2 no longer represents the crystal geometry effect, but the geometry of the segment weighting potential shown in Fig. 9.2b.

9.3 Rise Time Profiles

The rise time variation (10% – 90%) as a function of angle and depth for core and active segment signals are shown in Fig. 9.3. In the front part of the detector (see the data for 0 cm and 1 cm), a huge anisotropy is present since the electrons velocity contains a considerable component in the $\langle 111 \rangle$ direction. Two centimeter lower, this effect is strongly reduced. Here the electrons move in the coaxial part of the detector where only mobilities in the $\langle 100 \rangle$ and $\langle 110 \rangle$ direction are in play, which do not differ much. The anisotropy in this region is comparable to the geometrical effect, seen most clearly at a depth of 3 cm in the segment rise time data of Fig. 9.3. Here, a six fold symmetry from the geometrical size is dominant rather than a four fold one.

Since core and collecting segment witness the creation and collection of the electrons simultaneously, both core and segment should experience the same total rise time. However, in the front part of the detector the 10% – 90% core rise times do not coincide with the segment data and the rise times poorly reflect the average radial velocity in the non-coaxial part of the detector. This is caused by the fact that the core weighting potential is very shallow in the corners at the front of the crystal. This means that the 0% – 10% rise time (which is not measurable in praxis) is considerably longer than for the active segment signals. The 10% reference therefore badly represents the real start of the trace in these cases.

Best fit values to Eq. 9.1 for the 10% – 90% rise times are shown in Table 9.1. For the crystal orientation angle θ_0 the same values are obtained independently from the geometry amplitude. This demonstrates that the analysis fit functions provide consistent results. The core rise time variation R_{an} due to the electron anisotropic mobility is in good agreement with the variations found in the active hit segments. In the coaxial part, this causes a 8% peak-to-peak effect. Considering the large difference in weighting potential, it is not surprising that the R_{geo} values of core and segment do not correspond.

It is worth mentioning that the obtained parameters are also of practical use for the steepest slope method discussed in chapters 3.2.1 and 11.1 to determine the radial position of a γ -ray interaction. For this technique a conversion of the steepest slope time into a radial distance is required. The parameters in Table 9.1 demonstrate the dependence of the conversion on the angle and the depth of the interaction. Eq. 9.1 provides a tool to correct these effects when angle and depth of the interaction are determined independently e.g. by the investigation of the transient signals in the nearest neighbor segments.

Table 9.1: 10% – 90% rise time fit parameters to Eq. 9.1 for core and active hit segment.

depth	Core 10% – 90%				Segment 10% – 90%			
	A[ns]	$\theta_0[^\circ]$	$R_{an}[\%]$	$R_{geo}[\%]$	A[ns]	$\theta_0[^\circ]$	$R_{an}[\%]$	$R_{geo}[\%]$
0cm	205.5	40.0	-10.9	-3.7	262.0	40.7	-11.0	-1.1
1cm	213.6	40.9	-12.1	-1.6	260.0	41.7	-12.3	-1.2
2cm	204.2	40.1	-5.7	-2.5	225.3	42.1	-6.6	-4.6
3cm	205.0	39.8	-4.0	-2.5	214.6	39.2	-3.4	-5.7
4cm	213.6	40.1	-3.8	-2.2	223.9	38.9	-3.6	-1.9
5cm	220.5	40.7	-3.9	-1.9	230.8	39.6	-3.7	-0.7
6cm	226.5	41.0	-3.8	-1.1	234.3	39.8	-3.7	0.4
7cm	232.5	40.2	-4.4	-0.6	233.5	40.2	-4.2	0.8

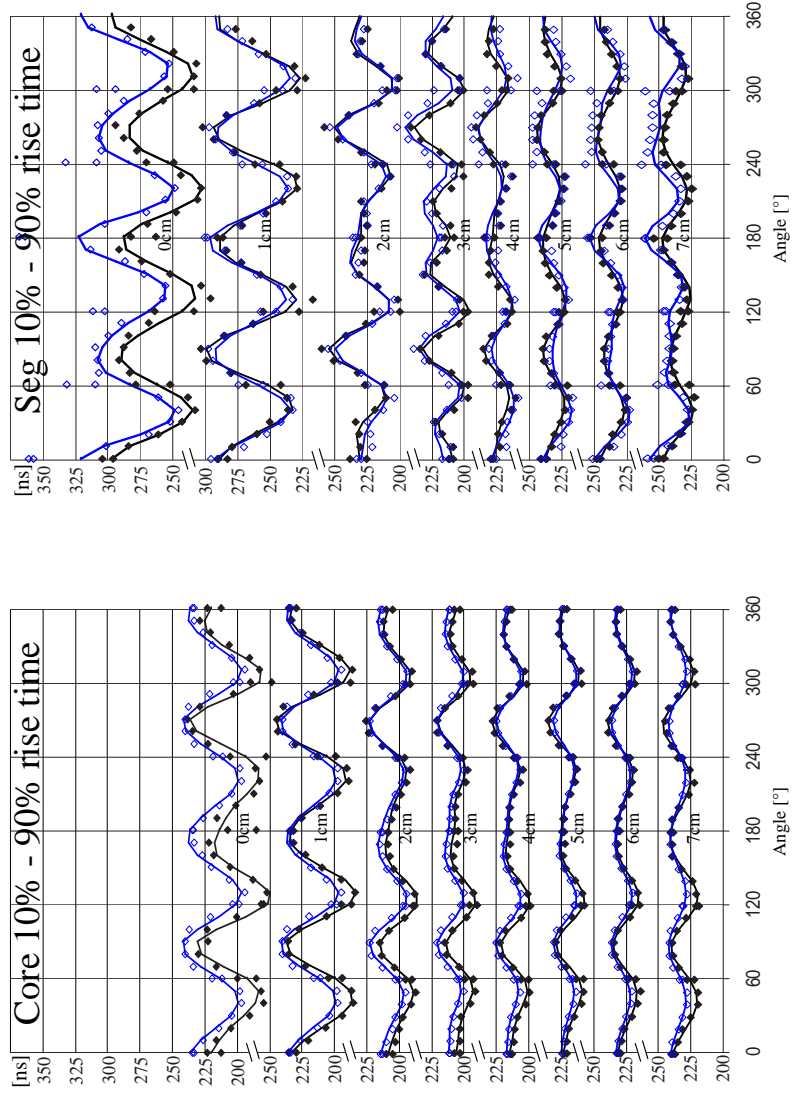


Figure 9.3: 10% – 90% rise time profiles of the electron mobility data. Full squares correspond to the measured data, open squares correspond to the optimized simulation. The solid lines correspond to the best fit using Eq. 9.1.

The fit parameters of the 5% – 30% and 40% – 90% core rise times are summarized in Table 9.2. In contrast to a strong dependency on the geometry of up to 7.9% near the outer electrodes the differences are completely vanishing near the core electrode as can be seen from the 40% – 90% core rise time fit values.

Table 9.2: Core partial rise time fit parameters to Eq. 9.1

depth	Core 5% – 30%				Core 40% – 90%			
	A[ns]	$\theta_0[^\circ]$	$R_{an}[\%]$	$R_{geo}[\%]$	A[ns]	$\theta_0[^\circ]$	$R_{an}[\%]$	$R_{geo}[\%]$
0cm	131.7	40.0	-14.9	-6.2	90.9	40.1	-5.3	-0.9
1cm	134.8	41.0	-17.5	-5.5	92.2	41.1	-4.5	-0.3
2cm	109.0	40.2	-8.2	-7.7	97.0	39.4	-2.3	-0.2
3cm	98.3	40.3	-5.0	-7.9	104.0	39.3	-2.7	-0.1
4cm	98.6	40.7	-4.3	-7.3	110.8	39.3	-3.1	0.1
5cm	98.7	40.8	-4.1	-6.0	116.3	41.3	-3.3	0.0
6cm	96.3	41.7	-3.7	-4.0	124.0	40.9	-3.4	0.2
7cm	89.9	40.6	-4.1	-2.4	137.4	39.6	-4.2	0.2

The anisotropy effect in the coaxial region is on average an 8% effect peak to peak, and is least pronounced near the core electrode. In the front region, this effect increases to over 30% due to the much lower mobility in the $\langle 111 \rangle$ direction. A similar behavior is observed for the anisotropy amplitudes measured on the segment partial rise times.

The 10% – 60% and 70% – 95% segment rise time data are shown in Fig. 9.5. The fit results using Eq. 9.2 are summarized in Table 9.3. In particular for the fit values for the 10% – 60% rise times of the segment data in Table 9.3, the large amplitude oscillations of R_{geo} are remarkable, which e.g. enables a very precise measurement of the angular position of the interaction. This information would be disregarded when only core and transient signals are used to determine the angle and depth of an interaction (see e.g. steepest slope and asymmetry 11.1).

9.4 Electron Mobility Parameters

To extract the electron mobility parameters from the 336 averaged traces measured along the detector surface, a large scale χ^2 minimization procedure was set up. This compared the core, the active segment and its three closest transient neighbor signals of all measured detector responses with data from simulation. The data at 0 cm depth was expected to show larger deviations from simulation. Since the unknown bulletization of the crystal was not included in the simulation, the rise times should be shorter than simulated

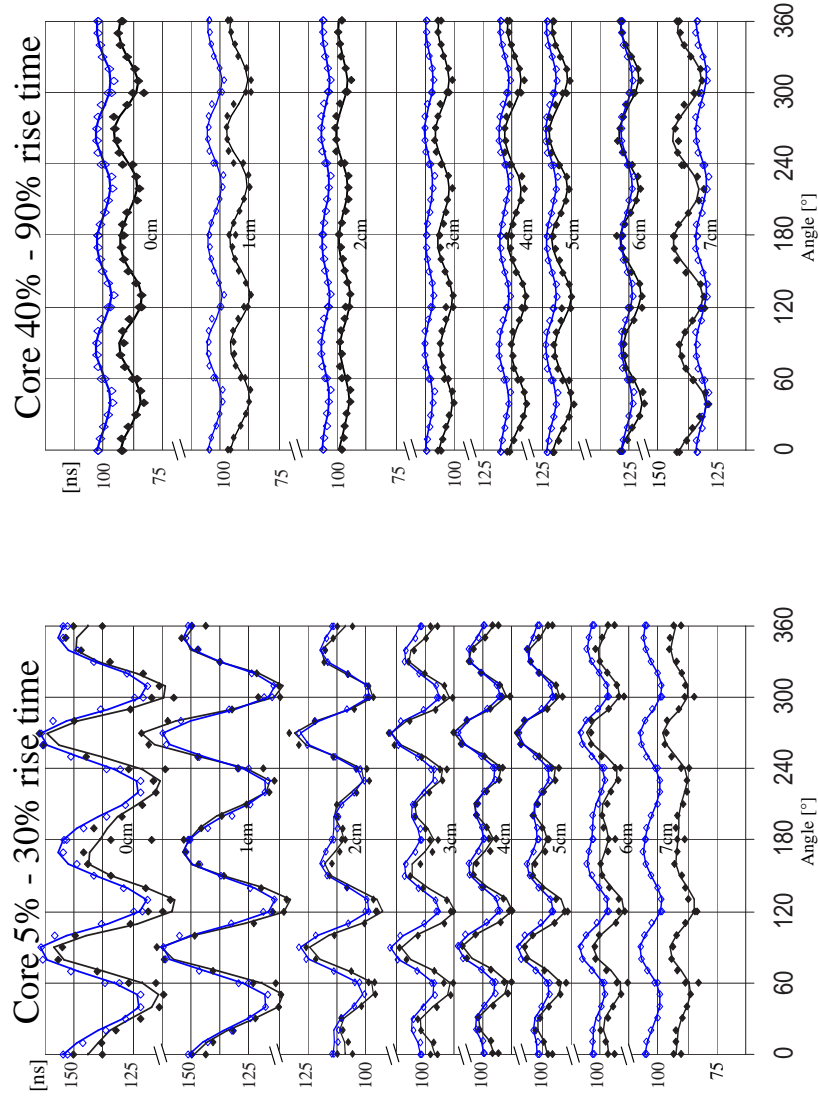


Figure 9.4: Core partial rise time profiles of the electron mobility data. Black squares corresponds to the measured data, open squares correspond to the optimized simulation. The solid lines correspond to the best fit using Eq. 9.1.

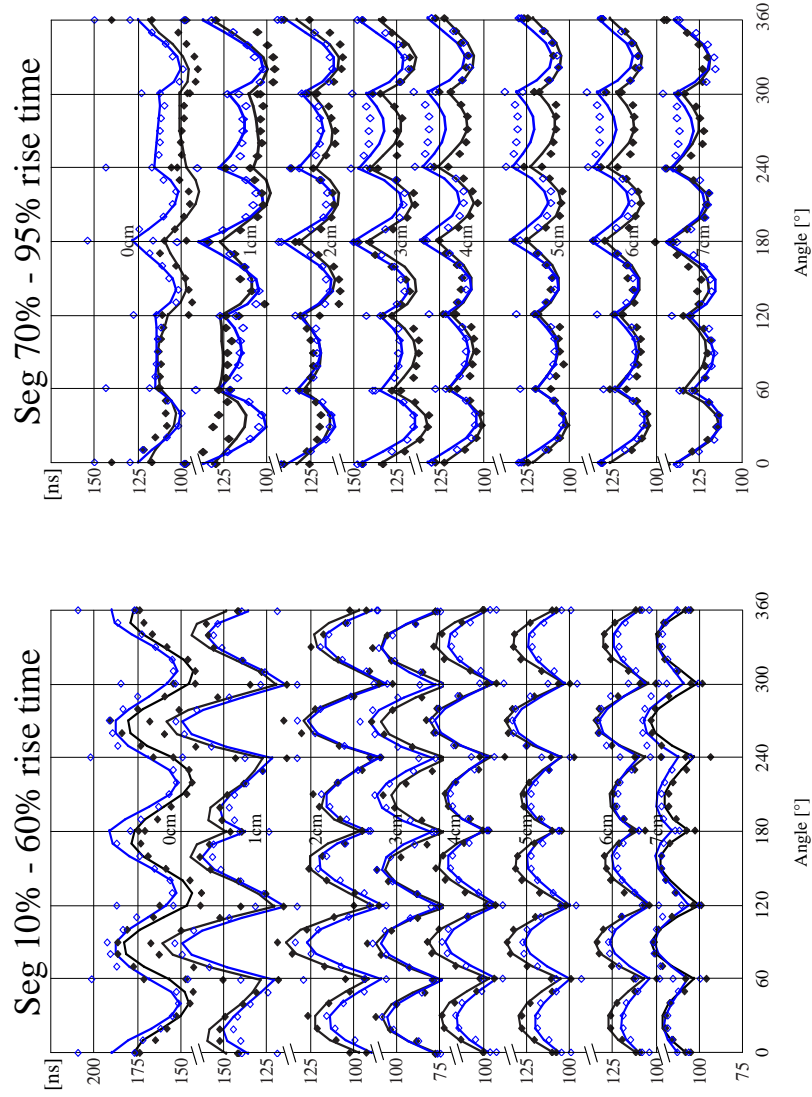


Figure 9.5: Segment partial rise time profiles of the electron mobility data. Full squares corresponds to the measured data, open squares correspond to the optimized simulation. The solid lines correspond to the best fit using Eq. 9.2.

Table 9.3: Segment partial rise time fit parameters to Eq. 9.2.

depth	Segment 10% – 60%				Segment 70% – 95%			
	A[ns]	$\theta_0[^\circ]$	$R_{an}[\%]$	$R_{geo}[\%]$	A[ns]	$\theta_0[^\circ]$	$R_{an}[\%]$	$R_{geo}[\%]$
0cm	159.1	40.5	-11.5	2.5	108.4	44.6	-6.0	-6.3
1cm	132.3	41.2	-12.7	24.0	120.9	46.6	-6.2	-10.9
2cm	90.1	41.9	-7.1	39.1	127.6	48.4	-3.1	-12.6
3cm	74.2	37.5	-2.5	46.8	134.5	38.6	-3.4	-14.9
4cm	96.4	39.1	-3.5	31.8	121.9	34.0	-2.5	-13.8
5cm	105.3	39.3	-3.6	25.7	120.7	37.0	-2.3	-12.9
6cm	107.4	39.9	-3.7	21.8	125.3	35.9	-2.6	-13.5
7cm	103.8	39.7	-3.6	19.7	137.3	38.2	-3.4	-13.1

at 0 cm depth. So, as not to dominate the optimization procedure, the 0 cm data was excluded from the fit.

The response functions and crosstalk amplitudes were implemented in the simulation as measured by the methods described in chapter 5. The mobility and space charge can be parameterized with 6 parameters for electron mobility (see chapter 7) and 4 for space charge, creating a final χ^2 optimization involving 10 parameters. It is assumed that the mobility parameters do not vary along the detector, and that the space charge varies linearly within the detector (see chapter 6). The last assumption is probably the boldest, since no parametrization for the space charge variation in such detectors is known and only average values of the space charge over the front and back surfaces are given by the manufacturer. The minimization routine was based on the sequential quadratic programming routine DONLP2 [68] which was developed for medium sized optimization problems (up to about 300 free parameters).

Requiring a cylindrically symmetric space charge distribution which varies linearly in radius and depth, the optimum space charge distribution was searched. The solution was discussed in chapter 6.1. The average impurity concentration was deduced to be 1.0 at the front plane and 1.5 at the back plane of the detector. These values compare to the values 1.47 (front) and 1.85 (back) as supplied by the manufacturer ¹.

Including the space charge values it was shown in Fig. 6.1 that the field strength ranges in the detector from 100-3000 V/cm. Obtained information on the mobility parameters will be obviously limited to this range of field strengths. The results on the extracted mobility parameters on the longitudinal anisotropy described by equation 6.2 are shown in Table 9.4. The

¹According to the manufacturer, the quoted numbers are the mean values between the concentrations measured at the center and on the outer radius of the crystal

Table 9.4: The optimum values found for the fit function For. 6.2 for the electron mobility data as obtained from the electron mobility characterization procedure.

Electron mobility parameters				
direction	$\mu_0[\frac{cm^2}{Vs}]$	β	$E_0[\frac{V}{cm}]$	$\mu_n[\frac{cm^2}{Vs}]$
$\langle 100 \rangle$	38609	0.805	511	-171
$\langle 111 \rangle$	38536	0.641	538	510

parameters on the $\langle 111 \rangle$ electron mobility were obtained from a fit to the electron mobility model described in chapter 7 using the $\langle 100 \rangle$ fit parameters of Table 9.4 and the values $\eta_0 = 0.496$, $b = 0.0296$ for $E_{ref} = 1200$ V/cm which were obtained from the χ^2 fit as optimum for the parametrization of the electron intervalley scattering rate. These mobilities differ substantially from the literature values reported by Mihailescu et al. [58].

In order to demonstrate the high precision and good quality of the new values, results of the simulation (open squares) and the best fit are compared to experiment in Fig. 9.3, 9.4 and 9.5. It shows that the worse comparison with experiment is at the very front side of the detector at 0 cm depth. Besides the constant off-set due to bulletization (not taken into account in the simulation), the simulation at 0 cm depth might be improved at the segmentation lines.

One observes in the 70% – 95% segment rise times that the 3cm-7cm simulated data show a stronger discrepancy between 240° and 300° . This is attributed to a badly measured response function in segment 11.

A quantitative comparison between the simulated and measured traces for the positions marked in Fig. 9.1 shows a very high agreement in Fig. 9.6. The maximum discrepancy between the various points of the traces is on average below 2%² as shown in Fig. 9.7. From the neighboring transients, one observes usually that the simulation is overestimating the maxima in the transients. The average maximum discrepancy however is less for the transient signals than for the core and hit segments.

9.5 Timing Measurement

So far only the signal pulse shape was object of discussion. In practice a very important quantity is the timing resolution. Also here pulse shape analysis can be of hand. By aligning experimental traces with their simulated counterpart, one also obtains information on the true trigger time, since the

²Amplitudes expressed in percentages are always quoted relative to the core signal amplitude.

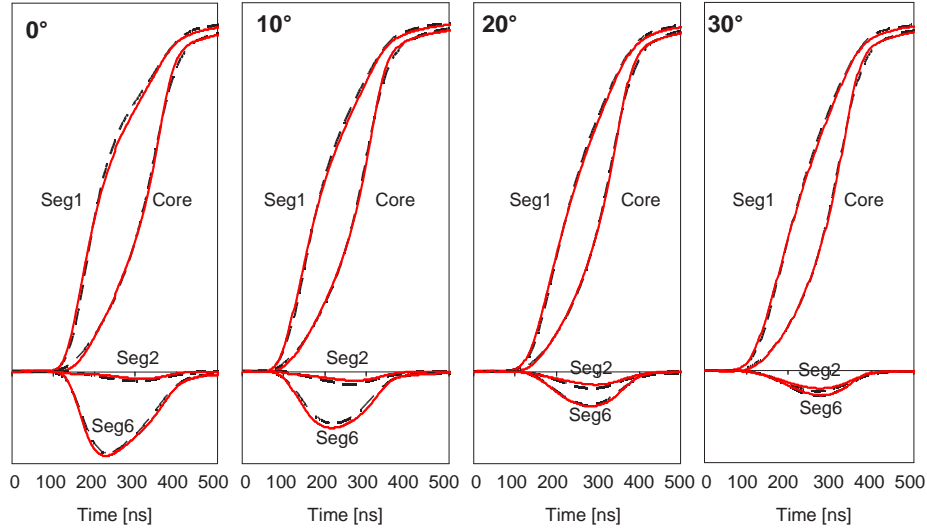


Figure 9.6: Direct comparison between measured (solid lines) and simulated (dashed lines) electron charge pulses. The pulses correspond to the response to positions 0,10,20,30 degrees in segment 1, at 2 cm depth (see Fig. 9.1). The maximum discrepancy between experiment and simulation is on average below 2%.

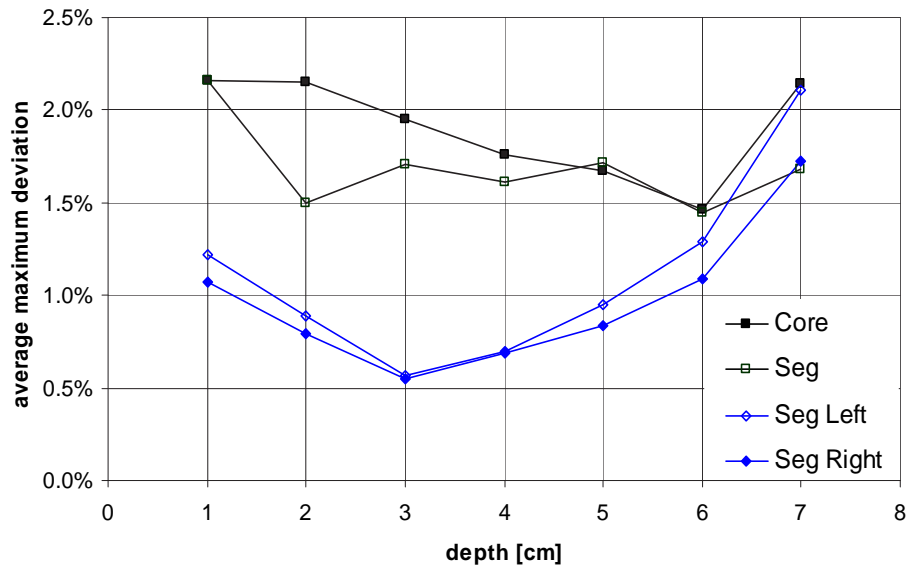


Figure 9.7: Variation with depth of the average maximum deviation between simulation and experiment.

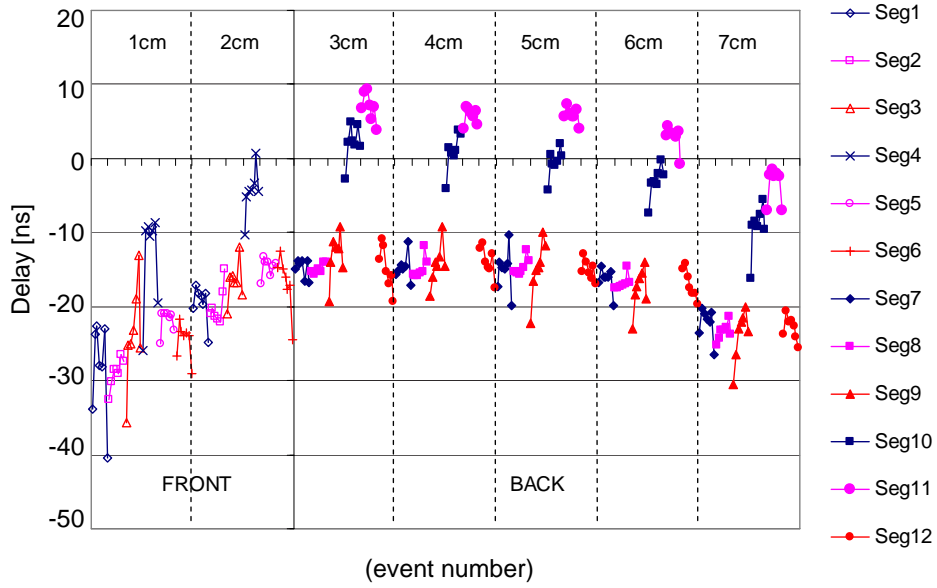


Figure 9.8: All relative delays of hit segments with respect to the core signals as obtained through a comparison with the optimized simulation.

underlying trigger time of the simulation is known.

Also in the minimization procedure described above, each channel was time shifted in order to maximize the overlap between simulation and experimental traces. In principle, one expects then that every channel has a fixed delay with respect to the core. The distribution of the relative time shifts to the core should therefore give information on the optimum timing resolution attainable by pulse shape analysis. This method should have better properties than standard analog techniques because it is walk-free³ and rise time independent.

To investigate the performance of such method, the optimum relative time delays from the hit segments of the 294 averaged events included in the fit procedure described above are shown in Fig. 9.8. One sees that there is not only a constant delay, depending on the specific segment, but also a variation with depth and angle shows up. The delays of the transients show a similar structure, however since transients are easier to misalign (e.g. small or zero transients are invariant under translation), they are more difficult to interpret and therefore are excluded from the discussion here.

To correct for the individual constant delays from electronics (cable length, rise time differences etc.) for each channel, an angle averaged delay was calculated for each segment at each depth. These 42 averages were

³For an introduction on the germanium related problems arising with timing, see [69, p.325]

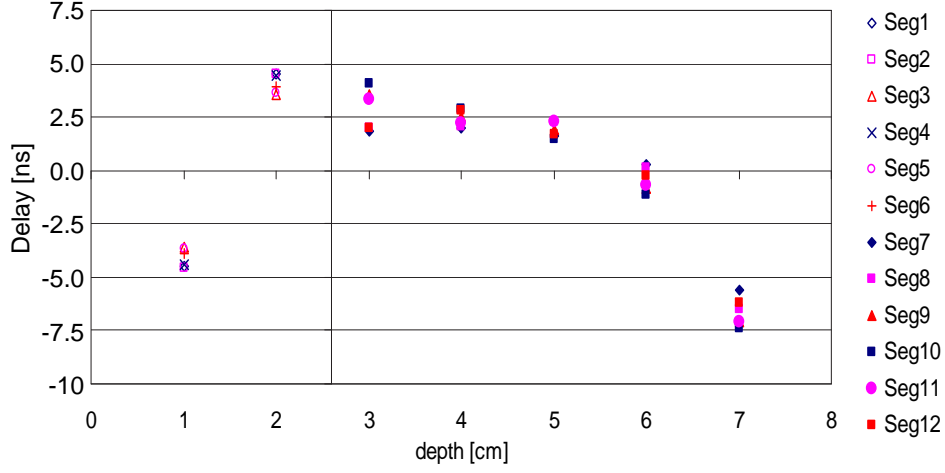


Figure 9.9: The depth dependent fraction of the delays shown in Fig. 9.8. This fraction is independent on the segment number.

further corrected for the total average time shift of each segment. Fig. 9.9 shows these corrected delays. One observes that a delay profile turns up which is only depending on the depth of the interaction and not on the segment number. Its effect varies over a range of 10 ns in total.

The residues, obtained after correction for the constant delays and depth depending delays, are still angle dependent. This can be seen from Fig. 9.10, where the variance of the residues is shown as function of angular position relative to the boundary of the hit segment. The variance was taken over all 42 data points sharing (relative) identical source positions. The variance turns out to be small inside the segments, but increases quadratically towards the edge of the segments. At the edge, the variance reaches a maximum of about 4 ns.

A possible explanation for the position dependent delay could therefore be that the time shifts are due to the extra path the current has to flow between the point where the cables are connected to the electrodes and the centers of mirror charge that are induced on these electrodes. However, it has to be pointed out that to achieve this accuracy in timing the demands on the simulation precision is very high (Remark that the original sampling rate amounted 25 ns). To show this, let us assume that the difference between the obtained average $T_{av}(t)$ and the simulation $S(t)$ is given by $S(t) = T_{av}(t) + N(t)$. When the trigger time t_0 is obtained through χ^2 fitting, it is found as the value y which minimizes:

$$\min_y \sum_i (T_{av}(t_i + y) - S(t_i))^2 \cong \min_y \sum_i \left(y \frac{d}{dt} T_{av}(t_i) - N(t_i) \right)^2 \quad (9.3)$$

The fraction in $N(t)$ that in χ^2 sense resembles the derivative of the trace

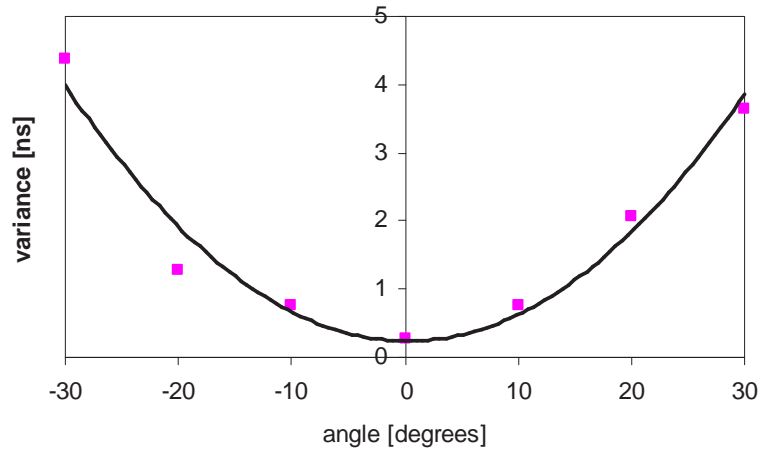


Figure 9.10: The variance of delays as function of angle after correction for the constant delays and depth dependent delays. This variance increases quadratically with angle.

will therefore cause a time shift. For rise times of the order of 200 ns, a derivative-like fraction in $N(t)$ of 1% would result in an error on t_0 of 2 ns. Such effects could therefore also form a possible explanation for the observed position dependencies of the time shifts.

Chapter 10

Hole Mobility Results

Measurements on the hole mobility in large volume HPGe n-type detectors have to cope with the experimental fact that only signals from γ -ray interactions very close to the inner contact at the central part of the crystal are exclusively determined by the holes as charge carriers. For a p-type detector, hole mobility measurements could be performed by applying the same method described above for the electrons. Indeed, such an investigation was done recently [70] on a p-type closed-end coaxial HPGe detector. A 13% hole anisotropy effect was observed on the rise times measured at fixed radial source positions in the coaxial part of the detector. For an n-type detector, it becomes much more difficult to demonstrate the anisotropy. The hole mobility characterization method described here provides for the first time detailed results on the hole mobility anisotropy and its parameters in a large volume, tapered n-type Ge detector.

10.1 The Measurement

Following the same reasoning as for the electrons in the previous chapter, information on the hole mobility is deduced from γ -ray interactions close to the core electrode. In these cases the electrons are immediately collected and the information on the holes travel towards the outer contacts can be extracted from the pulse shape. To reach the inner part of the crystal (radius of the detector is 35 mm) a higher initial γ -ray energy is required. The 356 keV line from ^{133}Ba was used for this purpose due to reasonably high yields at the center combined with a good photo peak to Compton scattering ratio. A 5 cm thick collimator with a 1 mm hole diameter was positioned at a depth of 7 cm with respect to the front of the detector (schematically shown in Fig. 10.1). At this depth, the crystal is nearly cylindrical and the semi-hexagonal crystal shape does not influence the measurements. By triggering on events with full energy deposition inside the segment positioned at 90° with respect to the collimator, Seg(i) in Fig. 10.1, the interesting events were selected online.

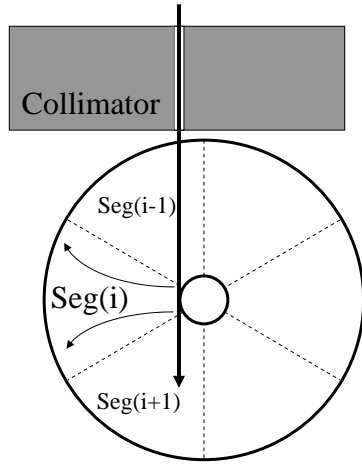


Figure 10.1: Setup of the collimator as used for creating events near the core. By gating on $\text{Seg}(i)$, a region near the core could be selected.

the time difference between both maxima was taken as reference for the collection time. A lower limit of 200 ns to this time difference was required, which typically reduced the events by 50%. This is in agreement with the expectation from the ratio between photo absorption and Compton scattered events. Events surviving this requirement generally also fulfill the first requirement. Third, a lower limit was applied to the 10% – 50% rise time of the core signals allowing for a good discrimination between traces with a short electron current contribution which reduces the 10% – 50% rise time considerably. Only 20% of the above events do not fulfill this requirement. An analysis of these rejected events showed that this condition very selectively cleaned out the region less than 6 mm from the core electrode.

To suppress Compton scattering events inside the selected segment, three conditions were applied to the recorded traces. First the transients in the neighboring segments have to be positive since only a positive charge is participating in the collection process. Crosstalk contributions however could make zero transients become negative, such that small negative transients were allowed. Second, long collection times are required because the hole mobility is smaller than the electron mobility, and thus the expected rise times are the largest possible in the detector. The core current signal for the events of interest is maximum at the trigger time, while the current through the hit segment will increase during the collection process till the holes are collected. Therefore the

10.2 Rise Time Profiles

In order to obtain a refined position information for the interaction point of the charge carriers, offline analysis was applied to extract the path the holes were following. The angular information on the trajectory is obtained from the maxima of the transients (see also section 11.1) in the neighboring segments ($\text{Seg}(i - 1)$ and $\text{Seg}(i + 1)$ in Fig. 10.1). The difference between both maxima has an equivalent function as the angle in Fig. 9.3 and gives values in the range of -30% till about 30% depending on which neighboring electrode was closest to the trajectory. Therefore, a pseudo-angle calibration is performed by mapping the range $[-30\%, 30\%]$ linearly into $[0^\circ, 60^\circ]$.

The rise time of the individual events are plotted as a function of the

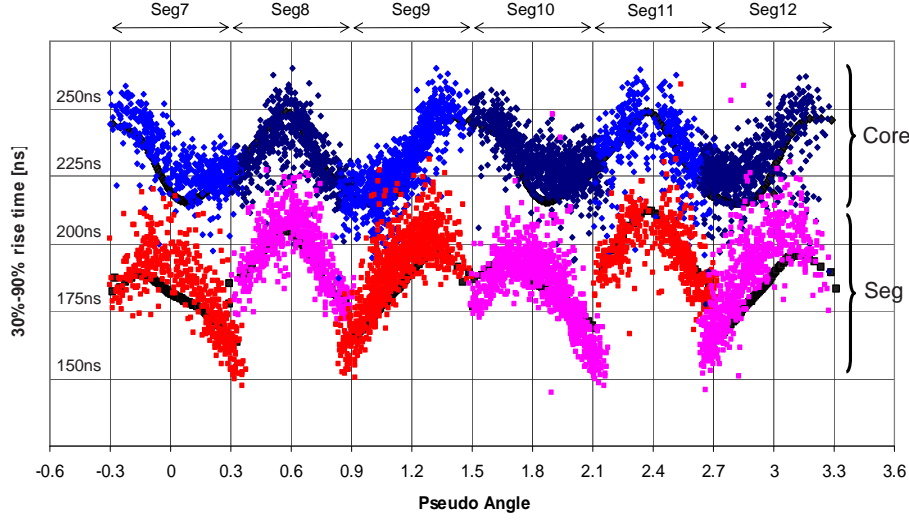


Figure 10.2: Rise time measurements at 7 cm depth of core and hit segments revealing the hole anisotropy. Dots correspond to single events. The thick line corresponds to the result of simulation calculations.

pseudo-angle in Fig. 10.2. The events shown were selected by the first two conditions. One can avoid here the third selection criterium by only showing the 30%–90% rise time. This makes the plot insensitive to any small electron current that might have been present during the 0% – 30% rise time. The 30% – 90% rise time reveals a nice continuity over the segment borders in the core data. From this, a hole mobility anisotropy effect of the order of 10% is deduced. For the rise times of the active segments, interestingly there is no continuity of the profile near segment crossings. This is due to transverse anisotropy as proven by simulation. By simulating the data with only the radial drift velocity component activated, this discontinuity was strongly reduced. The good agreement with experiment provides strong evidence that the applied hole mobility model can reproduce the transverse drift components correctly. The narrow width in the distribution of the events shown in Fig. 10.2 demonstrates the high angle selectivity obtained through this specific measuring technique. Such precision would be hard to achieve with the conventional Compton scattering technique alone.

To extract mobility parameters from this data, averaged traces were created and compared to simulation. Therefore, the pseudo-angle range of every segment was divided into 7 sectors. For each sector, a representative event was built out of the average of all the events in the sector. Analogously to the electron data, these 42 representative averages were then compared to the results of the simulation. The angular spread between events belonging to a specific sector still amounts up to 10° . This spread also has to be taken

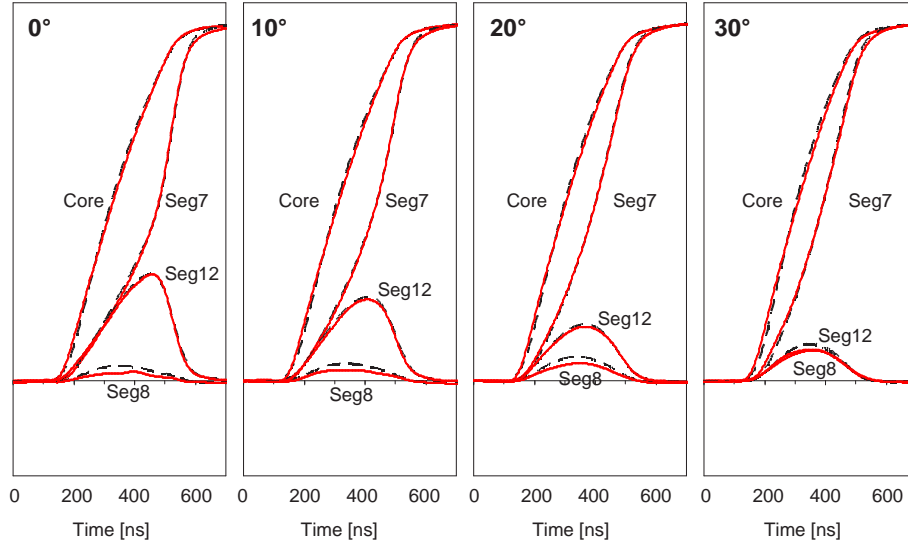


Figure 10.3: Comparison between measured (solid lines) and simulated (dashed lines) hole charge pulses. The pulses correspond to an averaged response near positions 0,10,20,30 degrees in segment 7, at 7 cm depth. Like in the electron case the deviations between simulation and experiment are on average below 2%.

into account when the representative averages are compared with simulation.

The simulation used for the holes employ the space charge distribution, crosstalk corrections and response functions as derived from the electron mobility characterization procedure. The model described in chapter 8 was employed to fully describe the hole mobility in the detector crystal using only 6 parameters which have to be determined from the fitting procedure. To simulate the 42 representative averages, 3600 traces were calculated from starting positions every 0.1° around the core. These traces were then sorted into the 42 sectors according to their calculated pseudo- angle. The average of every sector can then be compared to the experimental counterpart. Due to this elaborated procedure, this optimization took about ten times longer than for the electron mobility optimization.

The optimum hole mobility fit parameters are summarized in Table 10.1. With these values, the rise time dependence was simulated and compared with the experimental findings in Fig. 10.2. A direct comparison between four of the experimental averages and the simulation is shown in Fig. 10.3. The maximum deviations between simulation and experiment are on average below 2%; An accuracy which is comparable with the errors obtained for the electron mobility measurement at 7 cm depth.

Table 10.1: Optimum values for the fit function of Eq. 6.2 (with $\mu_n = 0$) for the hole mobility parameter as obtained from the hole mobility characterization procedure.

Hole mobility parameters			
direction	$\mu_0[\frac{cm^2}{Vs}]$	β	$E_0[\frac{V}{cm}]$
$\langle 100 \rangle$	61824	0.942	185
$\langle 111 \rangle$	61215	0.662	182

10.3 Anisotropy Enhanced Space Charge Effects

Since the measurements in the coaxial part of the detector in principle provided information in the crystal plane of $\langle 100 \rangle$ and $\langle 110 \rangle$ it is useful to investigate the pulses closer to the front part, e.g. at 2.1 cm depth, where the $\langle 111 \rangle$ mobility will also be important. Already during the acquisition, a striking difference in event yield was observed. While in some segments comparable yields as in the case of 7 cm depth were found, in other segments far more time was needed to collect the same amount of data. This is illustrated by the clustering of individual events in the core rise time profiles shown in Fig. 10.4A.

Simulation made clear what was driving this effect. Using the mobility parameters as derived from the 7 cm depth hole mobility data, events were simulated near the core electrode at 2.1 cm depth. These trajectories are shown in Fig. 10.5. At 2.1 cm, the trajectories are either going to the front of the detector or to the side. One millimeter above, all trajectories will end on the front side of the detector, while one millimeter below, all trajectories end on the detector side. This explains the large range in rise times that was observed as function of pseudo-angle in Fig. 10.4B. Since the shortest rise times originate from the positions created near 2.2 cm depth, the simulation of the 2.2 cm depth rise time profile creates a lower limit for the rise times shown in Fig. 10.4B.

To explain the clustering in Fig. 10.4A, a projection of the simulated trajectories at 2.2 cm depth is shown in Fig. 10.6. As shown in Fig. 8.5, tangential components in the drift velocity exist which grow to a maximum in-between the $\langle 100 \rangle$ and the $\langle 110 \rangle$ direction. This component always points into the direction of the nearest $\langle 100 \rangle$ direction as indicated by the arrows in the graph causing the contracted hole flow pattern in the regions near the $\langle 100 \rangle$ direction.

However, it is also demonstrated that the holes are trying to circumvent the crystal corners (points A, B and C in Fig. 10.6). This can be explained by the net effect the space charge has on the holes. If the detector geometry would be cylindrical symmetric, the space charge would only act on the holes

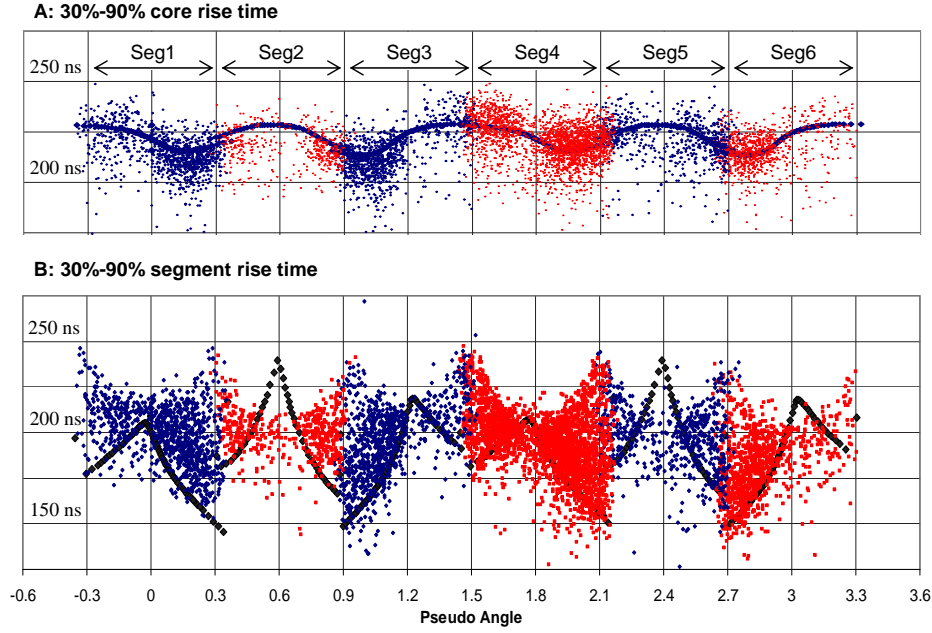


Figure 10.4: Rise time measurements at 2.1 cm depth. Dots correspond to single events. The thick dots correspond to the rise time simulation at 2.2 cm depth, which should give a lower limit to the observed rise times.

through radial forces. Due to the extra charge in such corners, this force will also have non-radial components. The repelling force in corner A is now enhanced due to the fact that also a $\langle 110 \rangle$ axis is going through this corner. The other $\langle 110 \rangle$ axis runs through the middle of corners B and C. Along this axis only a radial space charge repulsion can be felt due to symmetry. Enhanced spreading between the trajectories is therefore not observed along this axis. Anisotropy enhanced space charge effects therefore show up with a twofold angular symmetry.

The gaps and pile-ups created by this effect explain the clustering in the observed rise time profiles. In practice, the measured yield cannot be normalized easily since it will sensitively depend on the experimental conditions. For this reason, a direct comparison between the simulated hole current density (Fig. 10.7) and the experimentally obtained density (Fig. 10.4) cannot be made. However, similarities between both are present.

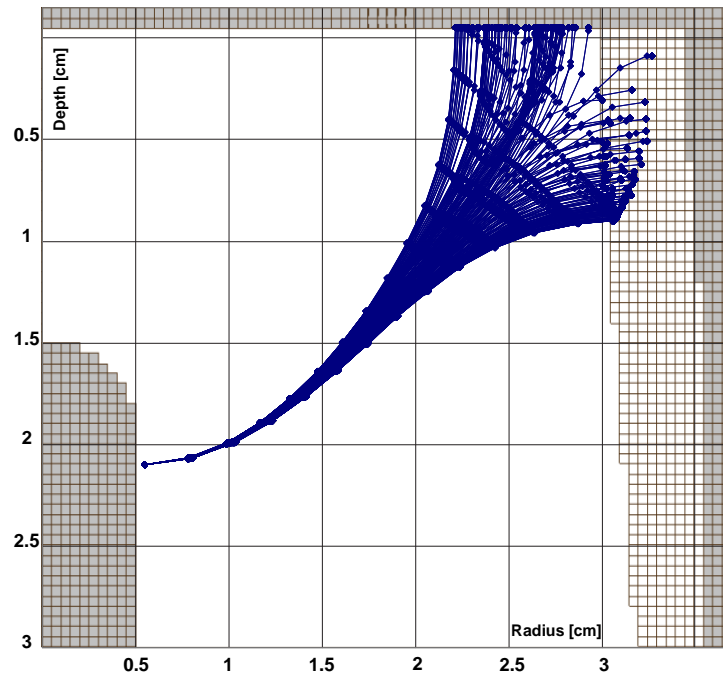


Figure 10.5: Simulated hole trajectories, radius vs. depth, for starting positions distributed in steps of 1° around the core at 2.1 cm depth. Dots along the curves correspond to 25 ns time steps. The holes are divided between collection on the front surface and collection at the side surface of the detector. The side surface is hexagonally shaped. This causes that the end of the trajectories are distributed over an interval of about 0.5 mm in radius (light gray area)

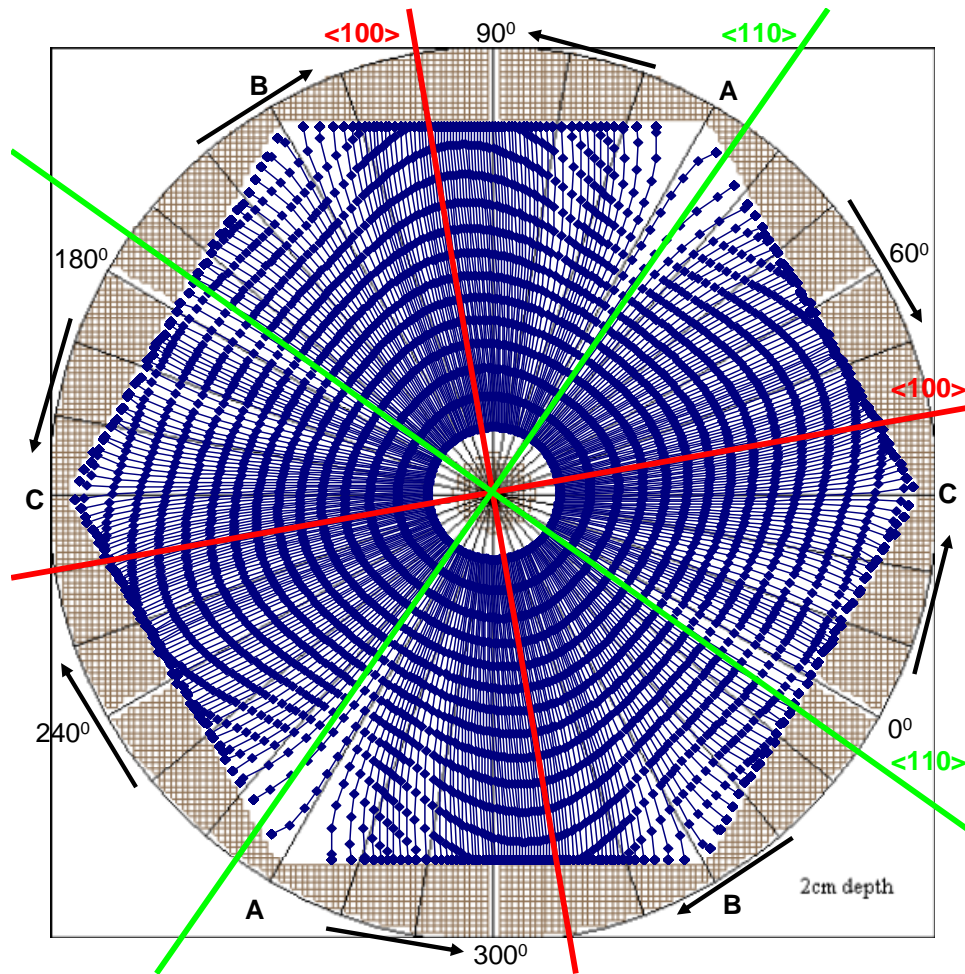


Figure 10.6: Simulated trajectories for starting positions near the core at 2.2 cm depth. The simulation was sampled every 25 ns. The crystal symmetry axis are indicated. The direction of the tangential anisotropic hole mobility component is indicated with vectors. This component, together with the net repulsion from the corners A,B,C cause the strong repulsion in corner A. A twofold symmetric pattern results.

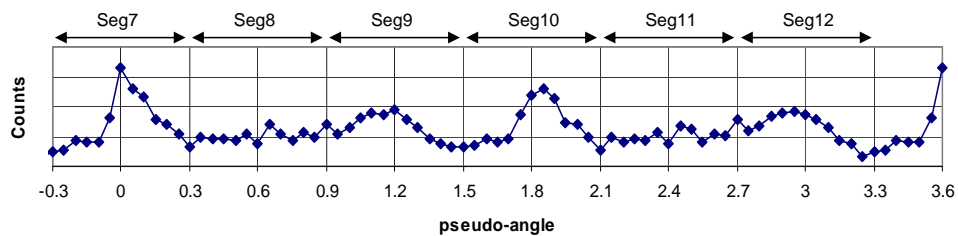


Figure 10.7: The hole current density as function of pseudo-angle for the simulation shown in Fig.10.6. To be compared with the experimentally observed density distribution shown in Fig.10.4.

Chapter 11

Pulse Shape Analysis

In this chapter, the problem of pulse shape analysis (PSA) is addressed. Past and future PSA methods are introduced. A simple PSA algorithm using simulated libraries will be established. This method was developed for the analysis of an experiment at ILL, which will be discussed in detail in chapter 12.

11.1 Steepest Slope & Asymmetry

Conventionally, MINIBALL relies on the steepest slope method (see section 3.2.1) to find the radial position of the main interaction. The time-to-steepest-slope T_{ss} can be expressed as [20, p.31] [23, p.87] [71, p.57]

$$T_{ss} = \min_t \frac{\partial^2}{\partial t^2} \text{Core}(t) - t_0 \quad (11.1)$$

with t_0 the trigger time and $\text{Core}(t)$ the core charge signal. For a single interaction, T_{ss} corresponds to the collection time of the electrons. This time is thus related to the distance of the interaction to the core electrode.

The angular information on the trajectory is obtained by analysis of the mirror charges $\text{Seg}_{i\pm 1}(t)$ observed in the direct neighbors to the hit segment i . The maxima M_L, M_R of the absolute value of these transients $M_L = \max_t |\text{Seg}_{i-1}(t)|$ and $M_R = \max_t |\text{Seg}_{i+1}(t)|$ are used to estimate the distance of the interaction from the neighboring segments. The asymmetry A_s in the mirror charges is then defined as [20, p.36]:

$$A_s = \frac{M_L - M_R}{M_L + M_R} \quad (11.2)$$

Due to the normalization, A_s will take on values between -1 and 1. Events with $A_s = -1$ happened close to the segmentation line between segment $i+1$ and i . Events with asymmetry $A_s = 0$ lie equally far from segment $i+1$ as from $i-1$, while events with $A_s = 1$ happened close to the segmentation line between segment i and $i-1$. Instead of the asymmetry, the function $\log(M_L/M_R)$ is sometimes used (see Gund [71, p.77]).

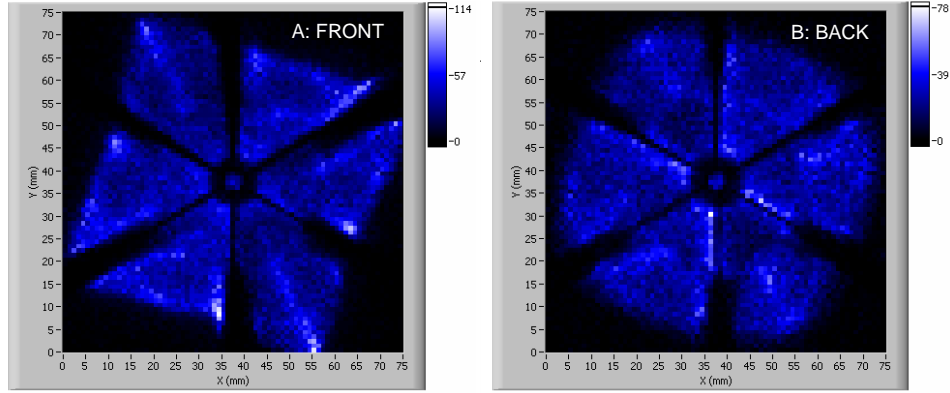


Figure 11.1: Position reconstruction using steepest slope and asymmetry. A: Reconstruction of events in the front part of the detector. B: Reconstruction in the coaxial part of the detector. Figures courtesy of Materna [74]: Obtained on the 2167 keV γ -transition in the $D(^{37}\text{Cl}, n)^{38}\text{Ar}$ reaction.

11.2 Doppler correction with MINIBALL

For the MINIBALL array, the combination of steepest slope with asymmetry provides the necessary position information on the main interaction to perform Doppler correction. True position information is not always needed for this task. Events can be sorted according to their steepest slope and asymmetry in a two-dimensional matrix. A spectrum obtained by gating on an individual bin of this matrix will show less Doppler broadening than the summed spectra. From the relative Doppler shift in the gated spectrum with respect to the stopped fraction, the average emission angle of the gated events can be obtained. For this, it is assumed that a γ -line of known energy is available which can be used as reference (which is not always the case).

The true position associated with each of the bins is then not needed. Therefore, systematic errors, created by nonlinearities in the conversion from asymmetry to angle and time-to-steepest-slope to radius, can be omitted. This method has the great advantage of being simple. The information can be calculated on-line [72] and no characterization is needed. With this method, it was demonstrated (Steinhardt [73]) that with an AGATA detector, a position determination of the main interaction to better than 5 mm is feasible.

Concerning tracking, this method cannot be applied. For tracking, the true three-dimensional position coordinates of all interaction positions are essential. Radius determination with this method is hindered as soon as multiple interactions are in play: All radii need to be identified from a single core signal. Obtaining depth information is hampered in the front and back segments, as these segments have less neighbors. In case of multiple

interactions, the necessary transients in neighboring segments can become corrupted by transients induced by the other interactions.

Besides that, this Doppler correction method also shows some obvious shortcomings when conversion from (T_{ss}, A_s) into real position information is unavoidable: In the non-coaxial part, the electrons move out of the plane perpendicular to the core electrode. This hinders a straight forward interpretation of the radial position. In this part of the detector, the steepest-slope-to-radius conversion is further strong angle dependent due to the anisotropic mobilities (see also chapter 9.3). For the 12-fold segmented detector, this causes that the reconstruction of the interactions in the front part of the detector is mapped into a square geometry (see Fig. 11.1A). As expected, in the coaxial part of the detector, this effect is strongly reduced (see Fig. 11.1B). Both graphs are affected by nonlinearities in the asymmetry-to-angle conversion which seem to be radius dependent and are responsible for the gaps between segmentation lines in Fig. 11.1A,B.

11.3 Future methods

Several new PSA methods are currently under development for the future AGATA spectrometer (see [75]). These methods should not only deal with the above listed problems. The aim for online analysis puts also stringent conditions on the numerical tractability and on the processing speed of these future computer codes.

The PSA codes can be divided into three categories. One category consists of single-step algorithms. This group of methods aims at predicting specific information in a non-iterative way, e.g. the number of interactions in an event, which can provide valuable input for the second category of algorithms: the iterative methods. As for position information, their capability is usually restricted to single interaction events. The conventional MINIBALL method of chapter 11.1 is a typical example. Its limitations were already discussed in detail in the previous section. Other examples are Artificial Neural Networks [76],[77, p.38] and the Folding Algorithm [38].

The second branch of PSA codes consists of iterative methods aiming at a decomposition of an event into single interactions. All of these codes make use of libraries with precalculated single interactions. The main difference between these codes lies in the search algorithm used with which the libraries are scanned. A second difference comes from the *figure of merit* (FOM) which measures the quality of agreement between the measured and reconstructed event. FOMs applied in the time domain are most common. Examples are the Least Square Method [78, p.93], the Genetic Algorithm [11, 79], its successor: the Particle Swarm method [80], Adaptive Grid Search [81], and the simple method described in chapter 11.4. Some people however prefer comparing events in a wavelet transformed space [53] (e.g. the Pattern

Recognition algorithm and the Haar wavelet transformation based method [82]). However, if time alignment as discussed in chapter 9.5 would turn out as important, a comparison outside the time domain is a less evident choice.

The last group of methods consist of a hidden form of linear least square fitting. They can be described as matrix methods. In this method, every single element in the library is considered as a base vector. The problem is then regarded as a decomposition of events in its basis. The method distinguishes itself from others in the fact that not just a small number of interactions is assumed, but one obtains a kind of probability distribution for each of the base vectors from which the interaction positions have to be distilled. The large number of parameters to determine makes this decomposition process very susceptible for noise. A fair amount of regularization is usually necessary, e.g. using singular value decomposition [51, p.59]. Since only positive coefficients in the decomposition are allowed, nonlinear boundary constraints are applied (see the Constrained Least Squares algorithm [83] and the Singular Value Decomposition algorithm [84]).

11.4 A simple PSA method

11.4.1 Single interactions

For the experiment at GAMS5, which purpose is described in detail in chapter 12, the fully characterized detector was for the first time brought into play. For this purpose, a simple iterative PSA program was developed to compare observed single interactions directly with the library. Libraries with simulated detector responses corresponding to single interaction positions covering the whole detector volume with 1 and 2 mm grid spacing were created.

A simple χ^2 value was implemented as FOM. The χ^2 value was evaluated over a *region of interest* (ROI) which contained the position-sensitive information: The ROI consisted of a time window on the rising edges of the charge signals and on transients and was further taken as small as possible in order to optimize the signal to noise ratio. For the same reason, only the χ^2 values of the core, the hit segment and its three closest neighbors were included in the FOM. Possible noise amplitude variations over different segments were not taken into account. It is obvious that this leaves room for improvement. In appendix A, a better FOM will be represented with respect to the signal to noise ratio.

However, before the FOM can be evaluated between the presumed single interaction $S(t)$ and an element in the library $L(t)$, both traces have to be normalized to each other and time-aligned (see the observed timing effects described in section 9.5). The normalization cannot be performed before the time alignment due to details in the structure of the acquisitions response function (see chapter 5.1). This structure causes bad normalization if both

traces involved are not perfectly aligned in advance. Therefore, the time alignment had to be performed independent on the amplitude of the traces involved. This time alignment procedure was based on the Cauchy-Schwarz inequality:

The Cauchy-Schwarz inequality 11.4.1 *Between two vectors \vec{S} and \vec{L} in an n -dimensional space ($i : 1 \dots n$), the following inequality holds:*

$$\left(\sum_{i=1}^n S_i \cdot L_i \right)^2 \leq \left(\sum_{i=1}^n S_i^2 \right) \cdot \left(\sum_{i=1}^n L_i^2 \right) \quad (11.3)$$

The equality holds if – and only if – S and L are linearly dependent.

The time alignment procedure therefore aims at maximizing the inequality in For. 11.3. Alternatively, the time alignment and normalization could be obtained through least square fitting. This means that parameters obtainable in a single step would be searched through iterative methods, which has negative consequences on the processing speed.

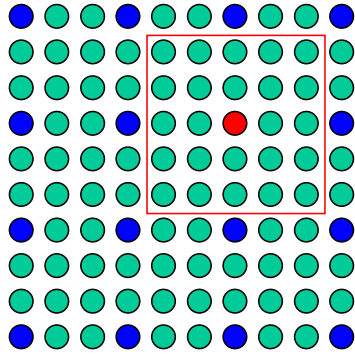


Figure 11.2: A simple grid search method: First the optimum (in red) is searched on a coarse grid. Subsequently, a better local optimum is searched in the red square on the full grid.

To speed up the library search, first a search on a coarse grid was performed to find a first optimum (see Fig. 11.2). Subsequently, a second local search was performed near the first optimum on the full grid. The grid size of the coarse grid was optimized by comparison of the routines performance to a full grid search. A wrong selection of this parameter causes that this procedure returns local minima rather than global minima (a search in three stages rather than two seemed also more critical with this respect). A typical coarse grid size of around 8 mm was chosen. With this method, single interactions were analyzed at a rate of 70 events per second, which was sufficient to perform an off-line analysis of the GAMS5 experiment.

No interpolation in the matrix was implemented yet, such that position resolution is limited by the final library grid size. Such interpolation method is described in detail in appendix A. Its performance is closely linked with the final attainable position resolution.

11.4.2 Multiple interactions

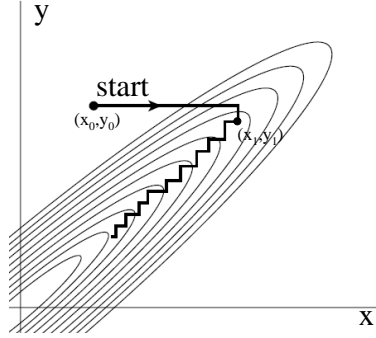


Figure 11.3: Typical multidimensional minimum search by iteration over one-dimensional problems (after [51, p.414]).

improved guess value (x_1, y_1) is passed to the search program as the initial guess value for a new iteration. Such procedure is repeated until the true optimum is found.

From Fig. 11.3, it is further evident that a proper choice of the coordinate system can speed up convergence considerably. By aligning the coordinate axis with the principle axis of the valley, the optimum would have been found after two iterations. Using such procedure, Powell [51, p.415] was able to come up with a method which is able to find the true minimum of a quadratic surface in n dimensions after exactly $n \cdot (n + 1)$ iterations. As Powells method provides the fastest convergence known to date for the described iterative method, a quadratic dependence of the CPU time on the number of interactions is the best one can hope for.

Applied to PSA, for n interactions, the problem is first reduced to a one-dimensional problem by isolating the contribution of the i -th interaction from the measured event S :

$$S_i = S - \sum_{j \neq i} E_j \cdot L_j \quad (11.4)$$

In this process, the simulated trace L_j and corresponding energy E_j represent the best assumptions for all interactions $j \neq i$ participating in the event. An improved choice for L_i and E_i can then be obtained by comparing the single interaction S_i with the library as described above. This procedure has to be repeated for all the interactions $i \in 1 \dots n$ till the iteration has converged.

At present, it is assumed that there can be maximally one hit per segment resolved. This conclusion was drawn from the analysis in section 12.2.1. The number of interactions therefore was taken equal to the number of hit

The single interaction scheme can be extended in a natural way to handle multiple interactions. The typical way to find a minimum of a function in a multidimensional search, is by iteration over constrained one-dimensional searches. This is illustrated in Fig. 11.3 for a minimum search of an exemplary two-dimensional function $f(x, y)$: Starting from the initial guess values (x_0, y_0) , a first optimum is searched using a one-dimensional minimization procedure to find $x_1 = \min_x f(x, y = y_0)$. A second one-dimensional search along $x = x_1$ yields $y_1 = \min_y f(x = x_1, y)$. This improved guess value (x_1, y_1) is passed to the search program as the initial guess value for a new iteration. Such procedure is repeated until the true optimum is found.

segments. If multiple interactions happen within one segment, the energy-weighted barycenter¹ of the multiple interactions is returned.

This procedure, implemented in the simple PSA method, seems generally to converge to a minimum. However, even for double interactions, the processing time turns out to be of the order of 1 s per event on an AMD athlon 2.4 Ghz processor (this compares to 14 ms per event for single interactions). Iterative methods therefore become rapidly slow.

¹The barycenter (from the fields of astronomy, astrophysics) is the center of mass of two or more bodies which are orbiting each other. Related to PSA, it is used to address the energy-weighted center of mass of multiple interaction positions.

Chapter 12

Gamma ray diffraction at GAMS5

After the detector had been characterized as described in the previous chapters, the detector was deployed in a test experiment at GAMS5 ILL, Grenoble. This experiment provided the first real challenge for PSA under true experimental conditions with a MINIBALL detector. A basic PSA method was for the first time applied. Its performance was compared with the traditional method using rise time and asymmetry.

12.1 GAMS5

12.1.1 About the spectrometer

At GAMS5, a Bragg-spectrometer augmented by a HPGe-detector is coupled to a high flux reactor of the Institut Laue-Langevin (ILL) [85]. With this experimental setup, the γ -rays produced by neutron capture are investigated through study of their Bragg-reflection. This allows at present an energy resolution which is unequalled by any other γ -spectroscopic method.

In a typical GAMS5 experiment, the line shape of the diffraction curve around the Bragg angle is measured. The width of this curve constraints the attainable energy resolution. Therefore, continuously efforts are undertaken to reduce the intrinsic resolution of the spectrometer. State of the art measurements allow energy resolutions of $\Delta E/E$ down to 10^{-6} using two flat crystals. This technique was for example used to determine the mass of the neutron [86], but also allows the study of short lifetimes ($\tau < 100$ fs) and interatomic potentials [87].

For experiments using such flat crystals, the most limiting factor is the count rate (The efficiency using double flat crystals is as low as 10^{-12}). Problems arise with environmental background and background created by

scattered gammas. Prolongation of the measuring time is no option as it also makes the experiment more sensitive to systematic errors [88].

The efficiency can be boosted by two orders of magnitude when bent crystals are used [89, 90, 91], although the resolving power of bent crystals is inferior with respect to flat crystals. Cylindrical shapes can only be realized with a precision of about 0.3-0.5 arcsec, while flat crystals have their surface determined with a precision of 0.005 arcsec. Thus at present, the trade-off for using bent crystals is a worsening of the resolution.

The requirement for a well defined bending is less stringent if the γ -detection system allows tracing back every diffracted γ -ray to the location at which it diffracted in the crystal. If the bending of the diffraction crystal is known from point to point along the crystals surface, the spectrometers response could be corrected for on an event by event basis. This concept is well known and applied in optics and x-ray diffraction (see e.g. [92]). For γ -rays, this is however not straightforward. The 12-fold segmented MINIBALL detector came in very handy for that purpose. Besides for the needed position sensitivity, it also provides good energy resolution to suppress background.

12.1.2 Setup of the experiment

A schematic overview of the setup is shown in Fig. 12.1 (see also [93, 94]). One or two 2.5 mm-thick Si-crystals in double bent mode were placed at a distance of 17 meters from a thin ($150\ \mu\text{m}$) in-pile source, consisting of natural erbium oxide. This source was situated at half a meter from the reactor core where it was exposed to a flux of $5 \cdot 10^{14}$ neutrons/cm s. This target material provides a number of very strong γ -ray transitions. During the experiment, the 184.285 keV, 284.655 keV and 815.900 keV γ -transitions were addressed.

These γ -rays, created by thermal neutron capture in ^{167}Er , were collimated through a $3 \times 8\ \text{cm}^2$ opening before hitting the first bent crystal. The trajectories of the diffracted γ -rays were subsequently sorted using a 1 m-long Soller collimator before they reached the segmented detector.

The low divergence of the γ -rays due to the large distance between the in-pile source and the crystals as well as the use of the Soller collimator makes it possible to correlate the position where the γ -ray hits the detector to the diffracting area of the Si-crystal.

12.2 Obtained position resolution

The registered traces were saved for off-line analysis with the PSA code described in section 11.4. Some of the data was acquired with only one slit – 2 mm by 15 mm – of the Soller collimator opened (as indicated in Fig. 12.1). From this data set, the obtained position resolution can be determined. In

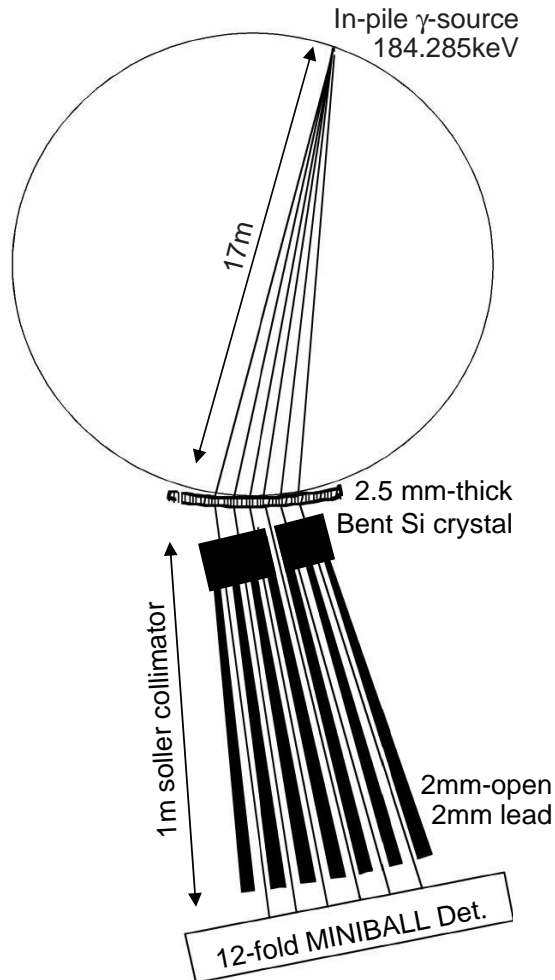


Figure 12.1: Schematic overview of the experimental setup at GAMS5. Part of the data was acquired with only one slit of the Soller collimator as indicated to deduce the position resolution.

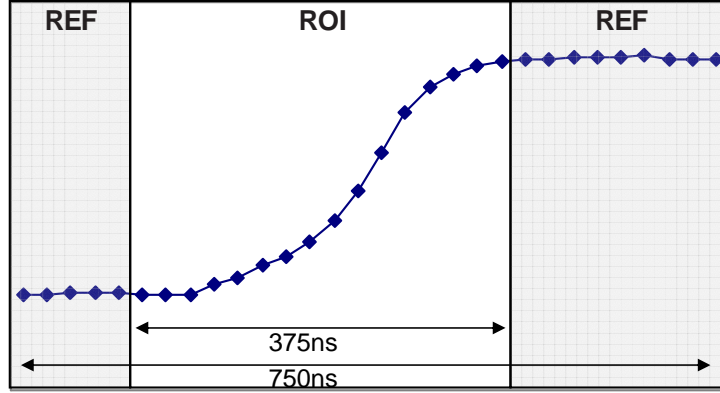


Figure 12.2: A typical core signal as acquired during the experiment. Traces of 750 ns were recorded. The ROI and REF time windows are indicated as used for the analysis.

total, more than 20000 184 keV photopeak events were acquired with the single slit.

12.2.1 Noise Analysis

The optimum position for each of these events was determined using the simple PSA algorithm described in section 11.4 and assuming a single interaction per segment. The discrepancy between simulation and experiment at this optimum was investigated. The noise was analyzed using a simple least square FOM.

In Fig. 12.2, one of the treated 184 keV events is shown. The noise level was measured twice: Once in the region of interest (ROI) and once in the reference time windows (REF) next to the ROI. The total noise vector \vec{n} in the ROI with length $|ROI|$ is expected to consist of two components: an electronic noise component \vec{e} and a component due to simulation imperfections \vec{c} . From the χ^2 value of the difference between the measured trace and the optimum simulated single event, one obtains an estimate for the variance σ_n^2 of the total observed noise:

$$\begin{aligned}\sigma_n^2 &= \frac{1}{|ROI|} \sum_{ROI} E(e_i + c_i)^2 \\ &= \sigma_e^2 + \sigma_c^2\end{aligned}\tag{12.1}$$

with σ_e^2 , the variance of the electronic noise and $E(.)$ the expectation operator. The simulation error σ_c^2 is not truly stochastic. Its influence on the total χ^2 FOM however behaves as a stochastic variable with variance σ_c^2 , which is not correlated with the electronic noise ($E(e_i \cdot c_i) = 0$).

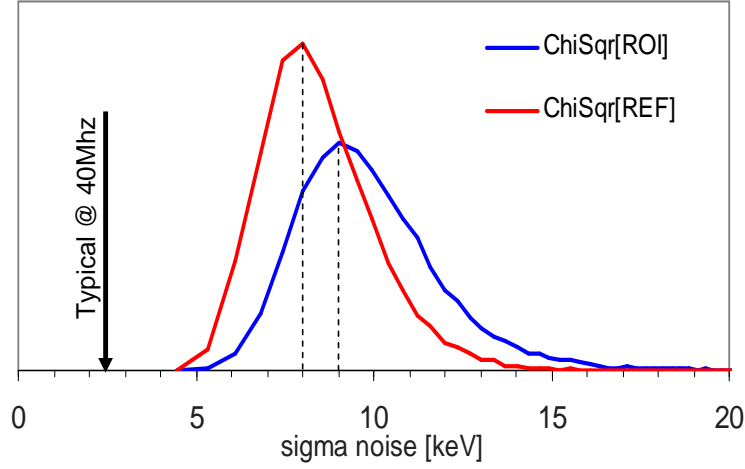


Figure 12.3: Noise levels measured at ILL. The electronic noise level amounted 8 keV. In the ROI, this value is increased due to characterization inaccuracy. Under good conditions, electronic noise levels of 2.4 keV can be achieved, in agreement with [41].

The electronic noise component can be measured directly in the REF area. A histogram of σ_n is shown in Fig. 12.3. On average, the measured electronic noise level during the experiment at ILL amounted 8 keV. Before the detector was transported to ILL, an average noise level of 2.4 keV was measured, which is in agreement with expectation from theory (Blair et al. [41]). The rather high noise levels are therefore attributed to the experimental conditions at the ILL site. The results on the obtained position resolution reported below have to be seen with respect to this low signal to noise ratio ($E/\sigma_e = 23$).

The measured noise level in the ROI is about $\sigma_n = 9 \text{ keV}$. From the characterization (see chapters 9.4, 10.2), one can expect an error which is about 2% of the energy, in this case $\sigma_c(184 \text{ keV}) = 3.6 \text{ keV}$. The expected noise level using For. 12.1 yields $\sigma_n = 8.8 \text{ keV}$. A value which is barely less than the average value of the observed distribution in the ROI (see Fig. 12.3).

Remember that these values were obtained under assumption of single interactions. That the observed value is close to our prediction indicates that the difference between multiple interactions and a single interaction is too small to observe using a simple χ^2 FOM. This does not exclude that other FOMs, dedicated to distinguish between single and multiple interactions, could be more successful with this respect. Using the simple least square comparison, multiple interactions happening inside one segment cannot be distinguished from single interactions at this noise level.

12.2.2 Image of a single slit aperture

The interaction distribution in the detector obtained with the single slit data are shown in Fig. 12.4. In A), a front view of the slit image is shown, as analyzed using a 1 mm and a 2 mm library. The 2 mm data was rotated by 180° around the core axis in order to facilitate the comparison of the projections of these distributions along the depth of the crystal (B,C). In the 2 mm data, the collimator is better visible. This is an effect of the higher binning, which increases the statistics per bin with a factor of 8 compared to the 1 mm grid. The linewidth of the 1 mm data (see Fig. 12.7) is smaller than for the 2 mm data.

In the side view (Fig. 12.4B), one sees a low count rate near the corners of the detector crystal. The reason for this effect was already observed during the characterization. It is caused by a bulletization of the crystal at the front of the detector. Although this effect was not included in the simulated libraries, it shows up as a PSA result.

The traditional method using steepest slope and asymmetry was also applied to the same data (see Fig. 12.4D). The method clearly performs worse than the PSA code using a library. The main reason that this method fails is the lack of depth information. Most events in this experiment lie in the non-coaxial part of the detector where depth corrections for the time-to-steepest-slope conversion are necessary. Such corrections are very difficult to perform with the 12-fold segmented detector.

12.2.3 Analysis of the observed collimator line width

Number of interactions

As discussed in section 12.2.1, a discrimination between single interactions and multiple interactions is impossible within the same segment using only a basic least square FOM. Multiple interactions located in the same segment will therefore be assigned to a single interaction coordinate by the PSA code equal to the energy-weighted barycenter of the interaction positions involved. To estimate to which amount this affects the observable line width of the collimator, the probability for multiple interactions has to be estimated.

At 184 keV, one expects about 40% of the events as single interactions, while 33% will undergo a single Compton scattering. Already 27% of the events therefore will undergo multiple Compton scattering. To make a first order estimate on the observable line width, these multiple Compton scattered events will be neglected in the following discussion.

Distribution of the energy-weighted barycenter

The profile created by the single interactions is very easy: Its front view resembles the shape of the collimator, while in depth, it creates an exponen-

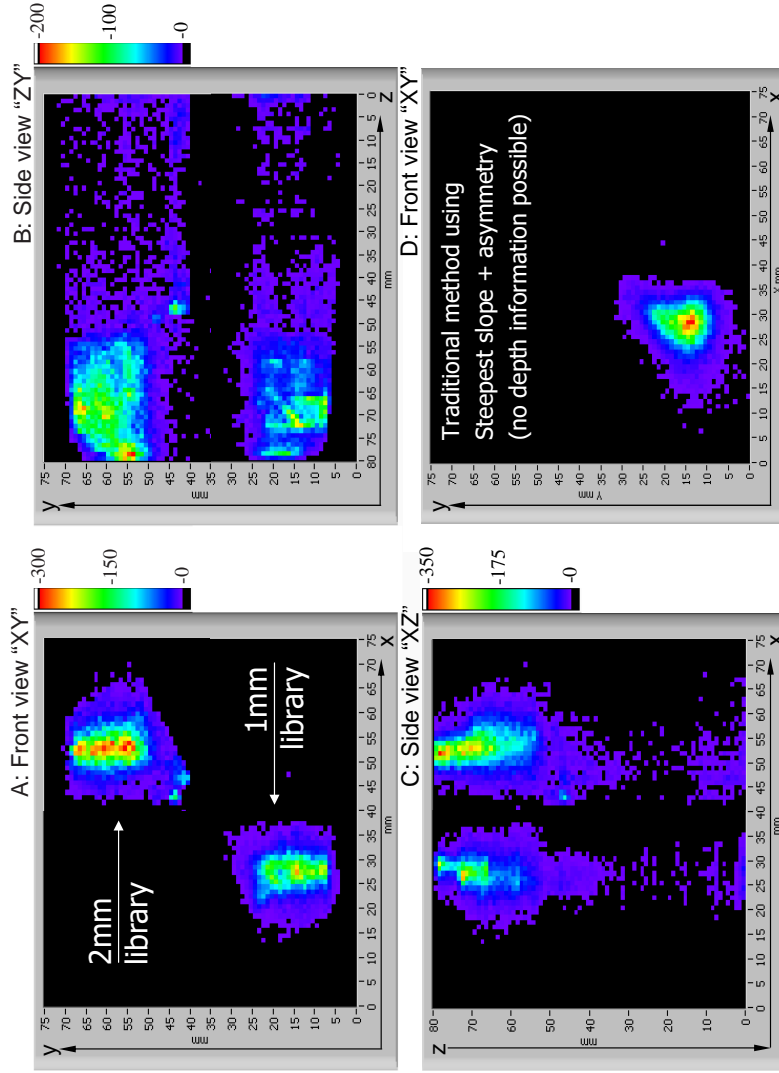


Figure 12.4: Image of a single slit (2 mm by 15 mm) made with the 12-fold segmented detector. The same data was three times analyzed. A: PSA results using libraries of different granularity. The 2 mm library results were rotated by 180° around the core axis such that the corresponding side views (B,C) are easily compared with the 1 mm library results. D: For comparison, the results using the traditional method in section 11.1.

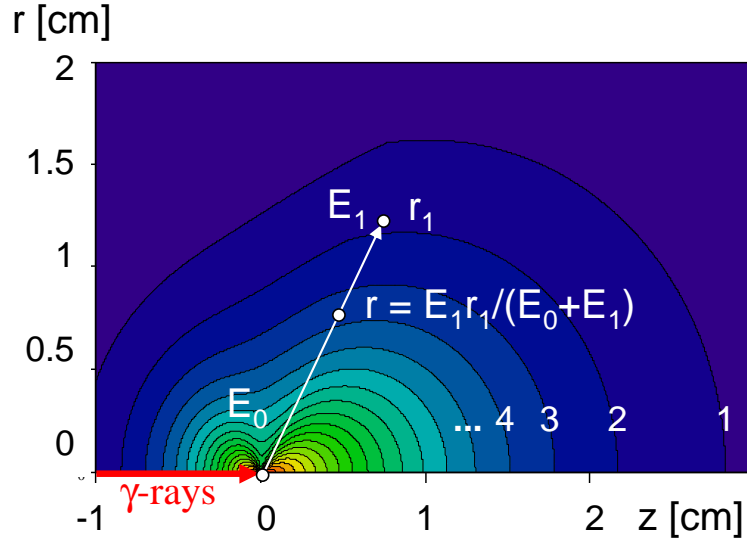


Figure 12.5: The probability in germanium for finding the second absorption event at position (r, z) from the scatter center $(0, 0)$ for a single 184 keV Compton scattered event originally incident along $r = 0$. Analyzing a Compton scattered event by assuming a single interaction will yield the position of the energy-weighted barycenter r .

tially decaying distribution with an average range of $\lambda(184 \text{ keV}) = 1.0 \text{ cm}$ for germanium.

For the single Compton scattered fraction, let us first assume that the first interaction in the detector happened at coordinate $(r = 0, z = 0)$. The probability of finding the location where the absorption took place is then given by the Klein-Nishina formula, combined with the exponential absorption law. This results in Fig. 12.5. From this distribution, the distribution of the energy-weighted barycenter of both interactions can be easily derived as illustrated.

Finally, in case the collimator is a slit rather than a pinhole, the observed distribution is the projection (integral) of the distribution of barycenters deduced from the probability distribution drawn in Fig. 12.5. The distribution of these barycenters, integrated along the slit, is shown in Fig. 12.6.

At this energy, the distribution has a minimum width of 8.4 mm FWHM across the collimator slit. The distribution in depth does not show a maximum at 0, but is shifted by nearly 5 mm along the initial γ direction. This shape has to be convoluted with the exponential decaying probability for the penetration of the first interaction in the germanium. The final distribution of the Compton scattered fraction therefore does not behave exponential along the detectors depth. Moreover, in the front, this distribution is lowered as more gammas can scatter out of the detector.

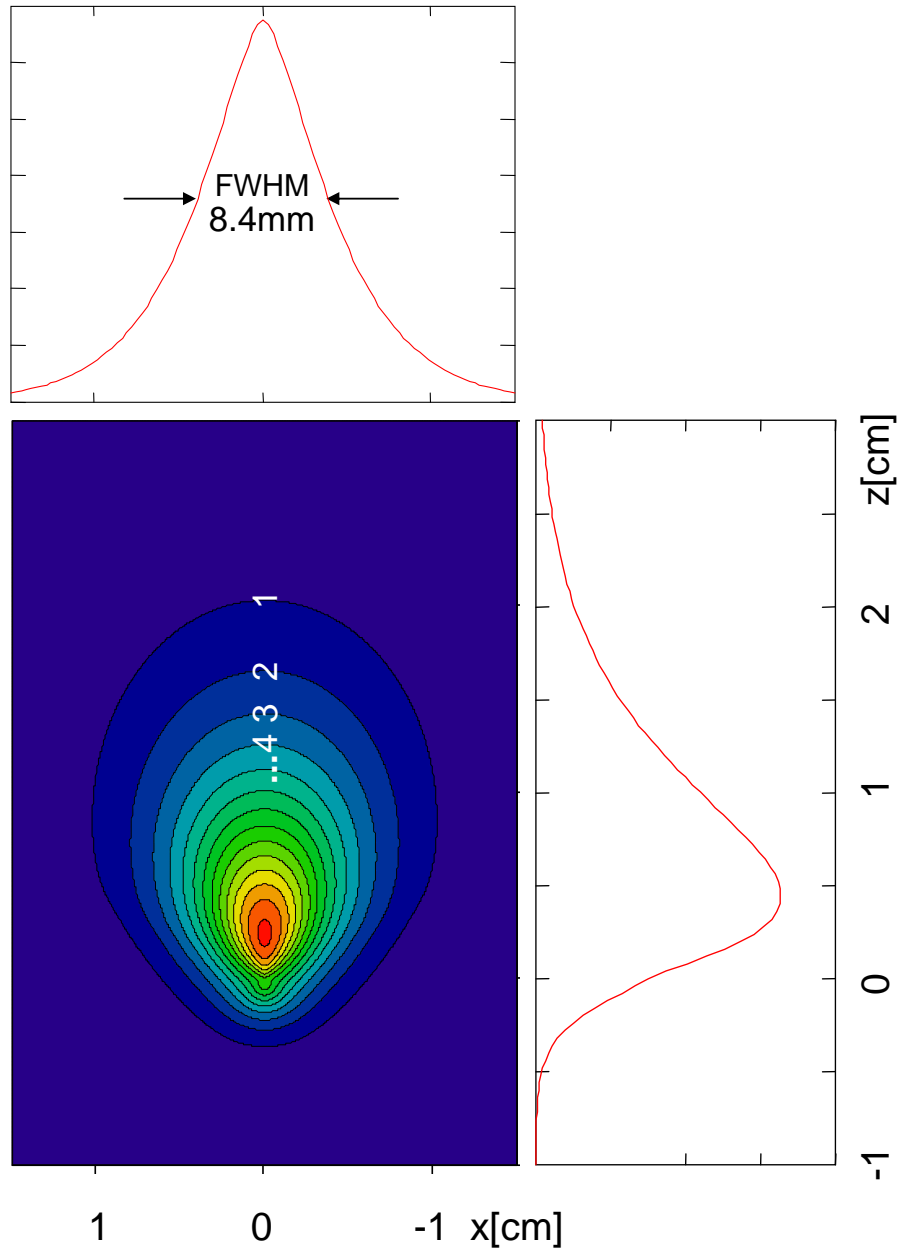


Figure 12.6: The projected distribution (integral over y) in germanium for finding the barycenter of a single Compton scattered event at a distance (x, z) from the scatter center. The distribution was derived from the distribution shown in Fig. 12.5.

Comparison with the measured line width

Combining the results from the previous paragraph, one can estimate the observed profile $P(x)$ across the slit. This should mimic the following form:

$$P(x) \cong [w_1 \cdot \delta_x + w_2 \cdot C_1(x)] \otimes S(x) \otimes R(x) \quad (12.2)$$

The weights $w_1 = \frac{40}{73}$ and $w_2 = \frac{33}{73}$ correspond to the probabilities for obtaining one and two interactions. $C_1(x)$ is given by the projection shown in Fig. 12.6. $S(x)$ is the profile given by the shape of the collimator (taken as a gaussian with a FWHM of 2 mm) and $R(x)$ is the position resolution.

The function 12.2 is compared with the experimentally observed distribution in Fig. 12.7. The ideal line width is shown with a red thick line. The best fit through the observed distribution (black thin line) is obtained assuming a gaussian $R(x)$ with $\sigma = 1.4$ mm for the analysis using a 1 mm library. The results with the 2 mm library are slightly worse ($\sigma = 1.8$ mm). This is partly due to the missing interpolation routine such that the position resolution is limited by the library grid size.

The distribution along the depth is shown in Fig. 12.7. An exponential function ($\lambda(184 \text{ keV}) = 1.0$ cm) was plotted through the distribution to guide the eye. In the front part of the detector, the distribution does not behave exponentially due to scattering out of the detector and the bulletization of the crystal. The same happens near the single segmentation line in depth. This is because near segmentation lines one can better distinguish between single and multiple interactions. The behavior near the end of the crystal is caused by background.

12.3 Results

Once the position interactions in the detector are known, the further analysis can be performed analogously to the traditional doppler correction method explained in section 11.1. For a specific area at the detector front surface, a diffraction curve can be created gating on all events that passed that particular surface. Fig. 12.8 shows how the means of these gated spectra vary with the position of the events registered in the detector. On average, position corrected diffraction curves are 30 % smaller than the full diffraction curve obtained without position correction.

For a single crystal the shifts shown in Fig. 12.8 can be directly related to the local bending imperfections of the crystal. Therefore, these corrections should be independent of the energy of the incident γ -ray. This hypothesis was confirmed by the measurements at 284.655 keV and even with lower statistics at 815.990 keV, which both yielded a similar diffraction correction profile as shown in Fig. 12.8.

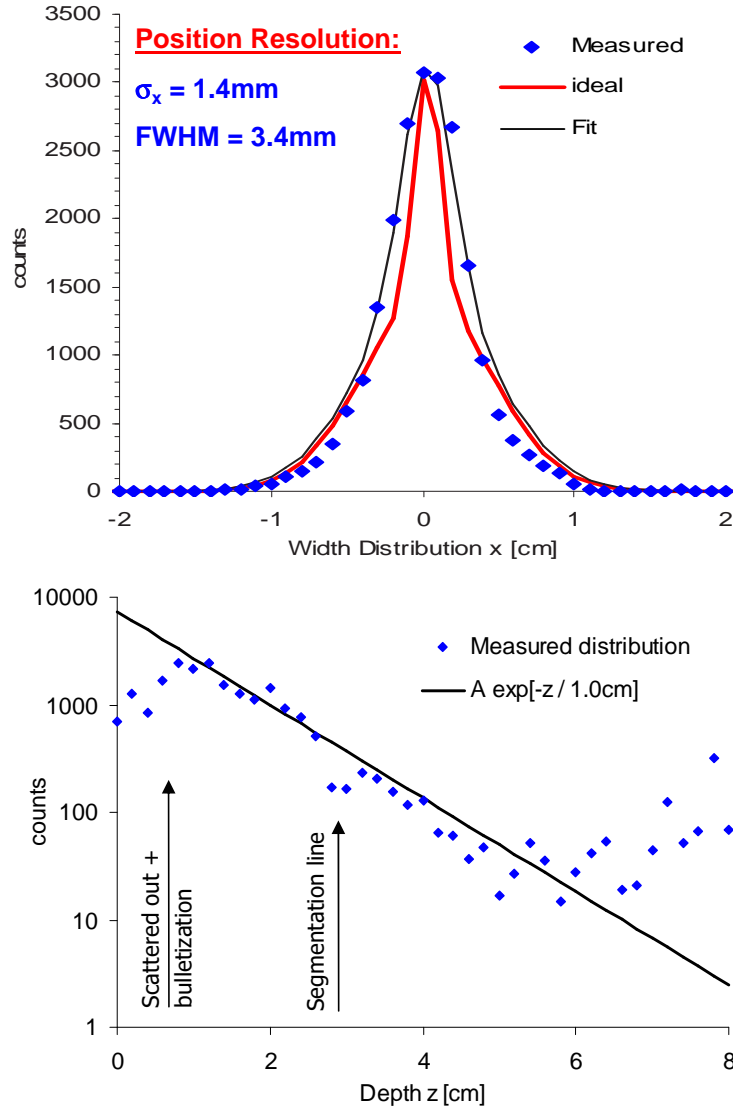


Figure 12.7: Analysis of the obtained position distribution using the 1 mm library. Top: The projection of the distribution shown in Fig. 12.4A. The fit function used corresponds to equation 12.2. Bottom: A histogram of the penetration depth obtained from the distribution shown in Fig. 12.4C.

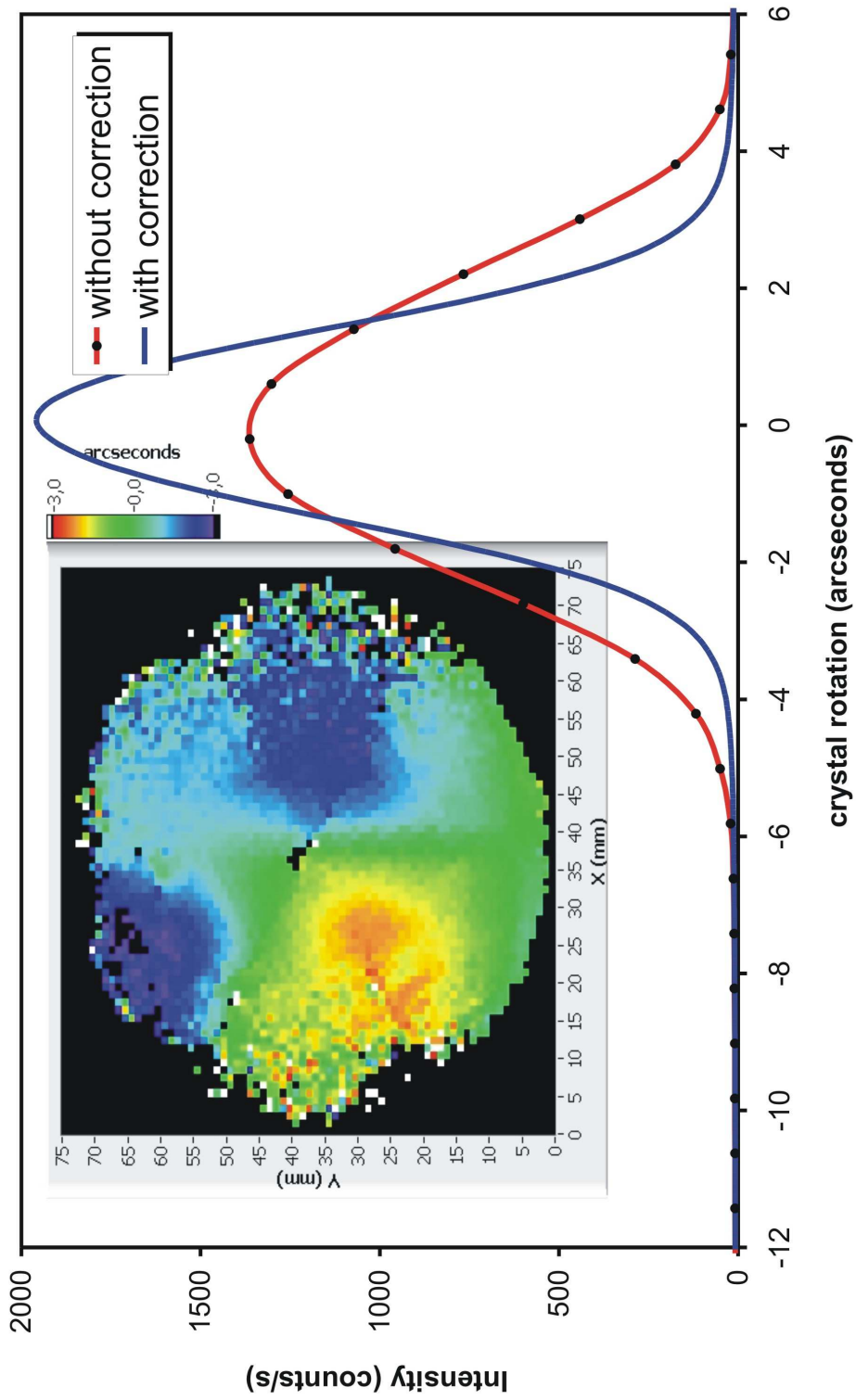


Figure 12.8: Plot of the observed shifts in the position gated distributions as function of the position on the detector. This corresponds to an image of the surface imperfections at the crystals diffractive surface. Also the full corrected and uncorrected line widths, measured at 184 keV, are shown.

Chapter 13

Conclusion

In chapters 7, 8 the problem of electron and hole mobility characterization was addressed from a theoretical point of view. An alternative electron mobility parametrization was presented, however, the more important contribution is an applicable anisotropic hole mobility model. The validity of this model was demonstrated using existing data from literature. The longitudinal and tangential velocity anisotropy as a function of the electrical field orientation for the hole mobility was compared to the electron mobility. The large differences between them cause specific rise times and pulse shapes as a function of the location where the charge carriers are created in the germanium crystal. These measurable effects of the electron and hole mobility are of pivotal interest for position determination and γ -ray tracking.

Both electron and hole mobility values in literature differ substantially at the level of accuracy required for pulse shape simulations in future applications. For the electron mobility, the difference is due to the dependency of the intervalley scattering rate on the purity of the crystal. A method for experimental determination of these mobility parameters on HPGe detectors was described in chapters 9, 10.

This allowed for the first time a full characterization of a large volume, irregular shaped, segmented HPGe detector. The final event information obtained by these methods is based solely on digitized preamplifier signals enabling a very precise response function analysis. To eliminate the derivative crosstalk contributions in the pulse shapes the use of these digitized pulses as a function of measuring time turned out to be a crucial prerequisite for a novel crosstalk method for segmented HPGe detectors. Its functionality was demonstrated on real data and allows a detailed reconstruction of the original signals. Besides the detection of these unwanted crosstalk phenomena, the origin of these effects was investigated and partially explained.

Numerous measurements of charge pulses very close to the outer and inner contact of the electrodes were utilized to measure the contributions of electrons and holes as charge carriers independently. The interplay of

Ge crystal properties and the response of the acquisition electronic was disentangled. The basic Ge crystal characteristics: crystal orientation, space charge distribution, electron mobility and hole mobility were extracted from the experiments. Precise electron mobility measurements were performed leading to a detailed knowledge on space charge and electron mobility parameters throughout the detector crystal. High precision in reproducing all measured electron charge pulses of the detector was achieved in simulations.

Measurements on the hole mobility have led to the first hole anisotropy measurements ever revealed in such large volume n-type Ge detectors. Both electron and hole mobility characterization measurements have allowed a precise description of the detector under study. High agreement between simulation and experiment was obtained, on average to better than 2%. This was achieved by implementation of anisotropic electron and hole mobility models in the simulation. The consistency of the new hole mobility model could be verified on the measured data. Non-trivial space charge enhanced anisotropy effects are clarified by this investigation.

With aid of the good simulation performance, for the first time a MINIBALL detector was applied in an experiment using a simulated library based PSA code. This enabled to overcome several limitations present in the traditional MINIBALL PSA codes based on steepest slope and asymmetry. The good position sensitivity achieved in the GAMS5 experiment (chapter 12) can be solely attributed to the high level of agreement achieved in the characterization procedures. Careful analysis of the data revealed that a position resolution of $\sigma = 1.4$ mm was achieved with a 1 mm library for a signal to noise ratio of $E/\sigma_e = 23$.

Correlations in the electronic noise turned out to be stronger than expected. As an outlook, a more powerful PSA method is described in appendix A which is able to deal with correlated noise. The method is expected to improve substantially on the resolution quoted above.

Appendix A

Position Resolution

The question on the obtainable position resolution is not so simple to answer, as it depends on numerous factors such as the ratio between deposited energy and electronic noise, the interaction position in the detector, the number of interactions, the properties of the frontend electronics etc. It clearly also depends on the pulse shape analysis (PSA) applied. A short introduction is given into the complexity of the fitting procedures that result when high-precision PSA is aimed at. Finally, the theoretical attainable position resolution is discussed under application of such high-precision PSA algorithms.

A.1 The Multivariate Normal Distribution

A.1.1 Shape of the distribution

To be able to relate noise and resolution in a mathematically tractable fashion, it is necessary to introduce a relevant statistical tool: the *Multivariate Normal Distribution* [95]. This distribution is a generalization of the normal distribution into higher dimensions:

$$N(\vec{e}; \vec{\mu}_e, \mathbf{\Sigma}_e) = \frac{1}{\sqrt{(2\pi)^n \det(\mathbf{\Sigma}_e)}} \exp \left[-\frac{1}{2} (\vec{e} - \vec{\mu})^T \cdot \mathbf{\Sigma}_e^{-1} \cdot (\vec{e} - \vec{\mu}) \right] \quad (\text{A.1})$$

The distribution describes the probability of obtaining a vector \vec{e} which has mean (vector) $\vec{\mu}_e$. Its variance-covariance matrix $\mathbf{\Sigma}_e$ is the multivariate version of the variance in a normal distribution. This matrix is defined as $\Sigma_{eij} = \sigma_{ij}$. The diagonal of this matrix consists of the variances $\sigma_{ii} = \sigma_i^2$ of \vec{e}_i , while the off-diagonal elements allow to account for possible correlations between the components of \vec{e} .

A.1.2 Parameter Estimation

In a similar way as for Gaussian distributions, the mean $\vec{\mu}_e$ and variance-covariance matrix $\mathbf{\Sigma}_e$, which describe a multivariate normal distribution

completely, can be estimated from a statistic. Given a statistic of length n : $\vec{B}_i, i \in 0 \cdots n$, taken from a multivariate normal distribution $N(\vec{\mu}_e, \Sigma_e)$, then

$$\langle \vec{B} \rangle = \frac{1}{n} \sum_i \vec{B}_i \quad (\text{A.2})$$

$$\langle \Sigma_e \rangle = \frac{1}{n-1} \sum_i (\vec{B}_i - \langle \vec{B} \rangle) \odot (\vec{B}_i - \langle \vec{B} \rangle)^T \quad (\text{A.3})$$

are unbiased¹, sufficient² estimators for $\vec{\mu}_e$ and Σ_e respectively. The Law of Large Numbers also applies which guarantees that $\langle \vec{B} \rangle \rightarrow \vec{\mu}_e$ and $\langle \Sigma_e \rangle \rightarrow \Sigma_e$ as $n \rightarrow \infty$. In Eq. A.3, the symbol \odot denotes the matrix direct product and is defined by [96]:

$$\vec{a} \odot \vec{b}^T = (a_0, a_1, a_2, \cdots) \odot \begin{pmatrix} b_0 \\ b_1 \\ b_2 \\ \vdots \end{pmatrix} = \begin{pmatrix} a_0 b_0 & a_0 b_1 & a_0 b_2 & \cdots \\ a_1 b_0 & a_1 b_1 & a_1 b_2 & \cdots \\ a_2 b_0 & a_2 b_1 & a_2 b_2 & \cdots \\ \vdots & \vdots & \vdots & \ddots \end{pmatrix} \quad (\text{A.4})$$

A.2 Measured noise properties

In *ordinary least square* (OLS) based fitting procedures, it is assumed that the data being fitted are all acquired independently. Blair et al. [41] derived the attainable position resolution under OLS conditions. This assumes the electronic noise is white: No correlation exists between noise sampled at dissimilar times.

How white the noise is in reality can be easily checked by measuring correlations in noise samples. Electronic noise is in general multivariate normal distributed. Along with the measurements described in chapter 5, random baseline samples $\vec{B}_k, k \in 0 \cdots n$ were taken with a total length of $|\vec{B}_k| = 30 \times 25 \text{ ns}$ to elicit the noise covariance matrix. The offset of these samples was adjusted, which causes that the mean μ_e is zero. Such procedure is commonly used in normalization procedures. The variance-covariance matrix of the noise Σ_e can be estimated from this statistic using equation A.3 as

$$\Sigma_e \cong \frac{1}{n-1} \sum_k (\vec{B}_k \odot \vec{B}_k^T) \quad (\text{A.5})$$

The statistical nature of the electronic noise is expected to be time invariant. The covariance matrix should therefore exhibit the property that $\sigma_{i,j} = \sigma_{i+k,j+k}$. It can be shown with this property that every row of the covariance

¹An estimator $\langle \vec{B} \rangle$ for $\vec{\mu}$ is unbiased if $E(\langle \vec{B} \rangle) - \vec{\mu} = 0$

²An estimator $\langle \vec{B} \rangle$ for $\vec{\mu}$ is called sufficient if the (Fisher-)information about the parameter $\vec{\mu}$ contained in $\langle \vec{B} \rangle$ equals the information in the statistic \vec{B} : $I_{\langle \vec{B} \rangle}(\vec{\mu}) = I_{\vec{B}}(\vec{\mu})$

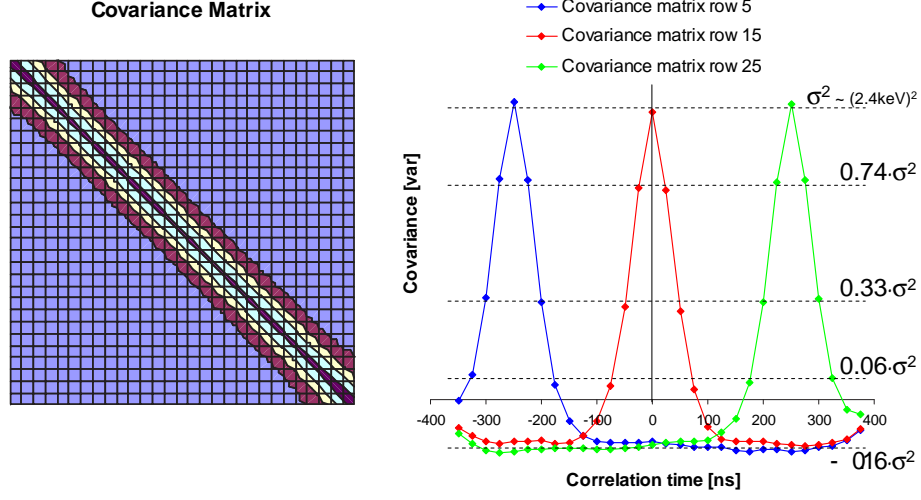


Figure A.1: Left: Contour plot of the entire 30×30 covariance matrix obtained using equation A.5. Right: Selected rows of the covariance matrix. Every row is a time-shifted image of the noise autocorrelation function. Average correlation coefficients for the most important matrix elements are indicated. Observe the negative correlation (-16%) at long correlation times induced by the normalization procedure.

matrix consists of a time-shifted window on the autocorrelation function³ of the noise. For true white noise, the covariance matrix becomes $\Sigma_{\mathbf{e}} = \sigma^2 \cdot \mathbf{I}_n$, with \mathbf{I}_n the identity matrix.

Realistic electronic noise, as observed through analysis of Eq. A.5, turns out to be more colorful than expected. A typical example of a noise covariance matrix for a single segment is shown in Fig. A.1. Three rows of this covariance matrix are shown in detail. The matrix is clearly non-diagonal. The observed noise shows relatively long memory effects. On all channels of the detector, the autocorrelations FWHM amounted slightly less than 100 ns. Even more surprising was that the correlations do not vanish over long times, but level off at a negative constant. This effect is produced by the baseline normalization $\sum_i B_{ki} = 0$ which causes that the sum of the covariance matrix elements $\sum_i \Sigma_{\mathbf{e}i,j}$ is zeroed for every column j :

$$\sum_i \Sigma_{\mathbf{e}i,j} = \frac{1}{n-1} \sum_k \left(\sum_i B_{ki} \cdot B_{kj} \right) = \frac{1}{n-1} \sum_k (0 \cdot B_{kj}) \quad (\text{A.6})$$

The described measurement demonstrates correlations in the noise within a single segment. In chapter 4, it was shown that segments form a weakly coupled network. It can therefore be expected that the noise, observed in

³Autocorrelation: see [21, p.124] or [97]

one channel, is not entirely uncorrelated from the noise observed in other channels either. Similar correlation measurements as described here have revealed that indeed strong correlations exist, mainly between direct neighboring segments. Such analysis could therefore provide an alternative way to investigate the behavior of crosstalk. In conclusion, there are indeed reasons enough re-evaluate the attainable position resolution applying realistic, colored noise.

A.3 General Least Square Estimation

Using the knowledge on the statistical properties of the electronic noise, obtainable as described in previous section, allows to make better predictions on interaction positions. The fitting procedure which makes it possible to fit safely with correlated data points is called *General Least Square Estimation* (GLS). An introduction is given here, with omission of all details and proofs, to illustrate how GLS and traditional OLS estimation compare. In this, the notation used in chapter 11.4 is maintained here for convenience.

Suppose $\vec{S}(\vec{p})$ is a normalized measured event of an interaction at position \vec{p} (represented by a vector which is the concatenation of the traces measured in all the segments). Suppose that $\vec{L}(\vec{p}_0)$ corresponds to the library event associated with position \vec{p}_0 in the vicinity of \vec{p} . The difference between $\vec{S}(\vec{p})$ and $\vec{L}(\vec{p}_0)$ is due to the distance $\Delta\vec{p}$ between locations \vec{p} and \vec{p}_0 and the electronic noise \vec{e} (the simulation error is disregarded for the moment).

In the neighborhood of \vec{p}_0 , one can approximate the variation of the events with position in first order by the model matrix

$$\mathbf{X}(\vec{p}_0) = \frac{\partial \vec{L}}{\partial \vec{p}} \big|_{\vec{p}_0} \quad (\text{A.7})$$

as:

$$\vec{S}(\vec{p}) - \vec{L}(\vec{p}_0) \cong \mathbf{X}(\vec{p}_0) \cdot (\vec{p} - \vec{p}_0) + \vec{e} \quad (\text{A.8})$$

The matrix in For. A.7 is sometimes called sensitivity matrix, for reasons which will become clear later (see section A.4). In general, this matrix is not square and thus not invertible such that a strict solution of the form

$$\Delta\vec{p} = \mathbf{X}^{-1}(\vec{p}_0) \cdot (\vec{S}(\vec{p}) - \vec{L}(\vec{p}_0)) \quad (\text{A.9})$$

does not exist, even when \vec{e} is zero. This is where fitting comes in. The PSA algorithm performs a regularization: it chooses the position which is most likely. Such fitting procedure can in general be regarded as selecting a pseudo-matrix inverse $\mathbf{X}^+(\vec{p}_0)$ [98] such that the best fit for $\Delta\vec{p}$ equals

$$\Delta\vec{p} = \mathbf{X}^+(\vec{p}_0) \cdot (\vec{S}(\vec{p}) - \vec{L}(\vec{p}_0)) \quad (\text{A.10})$$

Such fitting procedure implicitly makes a decision on what part of $\vec{S}(\vec{p}) - \vec{L}(\vec{p}_0)$ is caused by the distance $\Delta\vec{p}$ between locations \vec{p} and \vec{p}_0 and which part is caused by noise \vec{e} . Pseudo matrix inverses are not unique. Clearly holds: The better the noise can be predicted, the more accurate will be the obtained position information.

In the case of OLS fitting, the pseudo inverse in Eq. A.10 $\mathbf{X}^+(\vec{p}_0)$ becomes the generalized matrix inverse [99] $\mathbf{X}_{OLS}^+ = (\mathbf{X}^T \mathbf{X})^{-1} \mathbf{X}^T$, which provides the best guess to the solution of For. A.8, provided the noise is white. When this is not true, the best estimator for $\Delta\vec{p}$ is obtained with the GLS matrix inverse (see [100]):

$$\mathbf{X}_{GLS}^+ = (\mathbf{X}^T \Sigma_e^{-1} \mathbf{X})^{-1} \mathbf{X}^T \Sigma_e^{-1} \quad (\text{A.11})$$

This definition of the matrix inverse has the advantage over the OLS inverse that correlations in the noise are correctly taken into account through Σ_e^{-1} . This makes that the GLS estimator is more efficient⁴ than the OLS estimator.

Multivariate normal distributions posses the property to transform under affine transformations into other multivariate normal distributions. It is therefore not surprising that by the linear transformation in equation A.10, the multivariate electronic noise can be translated into a multivariate uncertainty in position. For the GLS inverse A.10, the following results are obtained (without proof):

Corollary A.3.1 *The position errors induced by electronic noise are multivariate normal distributed: $\Delta\vec{p} \sim N(\vec{\mu}_p, \Sigma_p)$. The optimum attainable position resolution is defined by the covariance matrix*

$$\Sigma_p = (\mathbf{X}^T \Sigma_e^{-1} \mathbf{X})^{-1} \quad (\text{A.12})$$

The optimum (GLS) estimator on the position, interpolated from the library at point \vec{p}_0 is given by:

$$\Delta\vec{p} = \mathbf{X}_{GLS}^+(\vec{p}_0) \cdot (\vec{S}(\vec{p}) - \vec{L}(\vec{p}_0)) \quad (\text{A.13})$$

In practice, additionally to the electronic noise, an unknown simulation error μ_e is present in Eq. A.8. This term is only depending on the position p_0 and leads, according to Eq. A.13, to a systematic position error $\vec{\mu}_p$ of

$$\vec{\mu}_p = \mathbf{X}_{GLS}^+ \cdot \vec{\mu}_e \quad (\text{A.14})$$

⁴Here, the statistical meaning of the word efficiency is intended (see [101]).

A.4 Position sensitivity

Equation A.12 gives us information about the obtainable position resolution. The errors on the position coordinates are given by the diagonal matrix elements of Σ_p . Remark that from For. A.1, all positions satisfying

$$\vec{p}^T \cdot \Sigma_p^{-1} \cdot \vec{p} = \text{constant} \quad (\text{A.15})$$

are assigned equal probability. Eq. A.15 can therefore be used to draw ellipsoidal confidence limits in position space. Such procedures are described in detail in [51, p.695].

In the case of white noise Σ_e equals $\sigma^2 \cdot \mathbf{I}_n$ and equation A.12 reduces to the OLS results published by Blair et al. [41]:

$$\Sigma_p^{OLS} = \sigma^2 (\mathbf{X}^T \mathbf{X})^{-1} \quad (\text{A.16})$$

with

$$\mathbf{X}^T \mathbf{X} \cong \frac{1}{\Delta T} \int \frac{\partial L(\vec{p}_0, t)}{\partial p_i} \cdot \frac{\partial L(\vec{p}_0, t)}{\partial p_j} dt \quad (\text{A.17})$$

and ΔT , the sampling period of the digitizers. The resolution obtained in OLS sense could thus be defined as $\sigma \sqrt{\text{tr}[(\mathbf{X}^T \mathbf{X})^{-1}]}$. The term *Position sensitivity* is frequently used as synonym for position resolution. However, the definition of the sensitivity seems to vary from author to author. A definition for sensitivity proportional to $\text{tr}(\mathbf{X}^T \mathbf{X})$ was used by G6rgen in [102] while the definition used by Kuhn [78] is inverse proportional to this. It is not difficult to prove that in general from neither of these definitions of sensitivity, the position resolution can be deduced: A fixed relation between sensitivity and resolution exists if, and only if the eigenvalues of $\mathbf{X}^T \mathbf{X}$ are threefold degenerated. Position resolution however is in generally not isotropic and sensitivities tend to lead to an overoptimistic approximation of the attainable position resolution.

Sensitivities for an AGATA and a GRETA prototype detector were discussed in great detail within the references [78, 102]. Summarized, one can state that these sensitivities predict that the resolution is highest near the segmentation lines. The resolution is increased when the segment volume is decreased. However, near the front and the back of the crystal, the resolution is reduced due to the missing neighboring segments.

A.5 Improved Figure of Merit

Let us now apply the acquired knowledge on the system errors to construct a good figure of merit (FOM). The evaluation of FOMs with a high signal to noise ratio (SNR) has also been studied in parallel fields of research, such as imaging with MRI [103] or as applied in radar technology, which could serve as further sources of information.

We will investigate a specific category of FOM's, which are derived from positive definite matrices \mathbf{F} as:

$$\text{FOM}[\vec{S}(\vec{p}) - \vec{L}(\vec{p}_0)] = [\vec{S}(\vec{p}) - \vec{L}(\vec{p}_0)]^T \cdot \mathbf{F} \cdot [\vec{S}(\vec{p}) - \vec{L}(\vec{p}_0)] \quad (\text{A.18})$$

The aim is to use \mathbf{F} as a smart filter such that the signal to noise ratio is optimized. In section 11.4.1, a modest attempt to create such FOM was introduced. This FOM is obtained by putting $\mathbf{F} = \mathbf{P}^T \mathbf{P}$, with \mathbf{P} the matrix which projects on the ROI-subspace. The shortcomings of this FOM were already discussed before.

A good FOM should weight the trace residues $(\vec{S}(\vec{p}) - \vec{L}(\vec{p}_0))(t)$ according to the information they contain at time t and inverse proportional to the estimated noise level at that time. Such kind of filter can be derived as follows: Consider the best FOM in position space. According to our knowledge on the error distribution (see For. A.12), the best FOM in position space would be the error-weighted⁵ FOM:

$$\text{FOM}(\vec{p} - \vec{p}_0) = (\vec{p} - \vec{p}_0)^T \cdot \Sigma_p^{-1} \cdot (\vec{p} - \vec{p}_0) \quad (\text{A.19})$$

This can now easily be converted into a FOM applicable to the library. Using relation A.13 we get:

$$\text{FOM} = (\vec{S}(\vec{p}) - \vec{L}(\vec{p}_0))^T \cdot \mathbf{X}_{GLS}^{+T} \Sigma_p^{-1} \mathbf{X}_{GLS}^+ \cdot (\vec{S}(\vec{p}) - \vec{L}(\vec{p}_0)) \quad (\text{A.20})$$

The trace samples are thus being weighted according to the amount of information (through the presence of \mathbf{X} in For. A.20) and inverse proportional to the amount of noise (through the presence of Σ_e^{-1} in For. A.20).









The performance of FOM A.20 was compared to the simple FOM described in section 11.4.1 using test signals and simulated multivariate noise. From comparison of the relative SNR values, improvements in SNR up to two orders of magnitude were observed for the sophisticated FOM. However, absolute numbers are difficult to quote, as the SNR values turned out quite sensitive to the signal shapes under test.

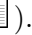



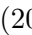

Such sophisticated filters are depending on the local position \vec{p}_0 in the library where the comparison is performed and are therefore computational intensive. Therefore, it is not expected that simple and fast FOMs will disappear completely from PSA. However, when high accuracy is requested, e.g. for the analysis of multiple interactions inside a single segment, such precise FOMs offer a more powerful alternative which cannot be overlooked. Finally, any scan of the library should be completed with a GLS-based interpolation as described by Eq. A.13, in order that the predicted position resolution by Eq. A.12 is also realized.

⁵The FOM obtained with omission of Σ_p^{-1} in For. A.19 was shown equally to produce high SNR values.

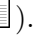
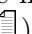

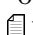
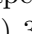
Bibliography

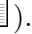
- [1] The official AGATA homepage.
URL <http://www-w2k.gsi.de/agata/>
- [2] the official GRETA homepage.
URL <http://greta.lbl.gov>
- [3] I.-Y. Lee, M. A. Deleplanque, K. Vetter, Developments in large gamma-ray detector arrays, Rep. Progr. Phys. 66 (2003 [\[1\]](#)) 1095–1144.
- [4] I.-Y. Lee, Proposal for gretina (2003 [\[1\]](#)).
URL <http://radware.phy.ornl.gov/greta/news2.html>
- [5] J. Simpson, AGATA Week Introduction., The Agata Week (February 2005 [\[1\]](#)).
URL http://npg.dl.ac.uk/AGATA/agata_week_talks/
- [6] The EUROBALL home page.
URL <http://nnsa.dl.ac.uk/euroball-home/>
- [7] GAMMASPHERE at ANL.
URL <http://www.phy.anl.gov/gammasphere/>
- [8] G. J. Schmid, M. A. Deleplanque, I. Y. Lee, F. S. Stephens, K. Vetter, R. M. Clark, R. M. Diamond, P. Fallon, A. O. Macchiavelli, R. W. MacLeod, A γ -ray tracking algorithm for the GRETA spectrometer, Nucl. Instr. Meth. A 430 (1999 [\[1\]](#)) 69–83.
- [9] J. van der Marel, B. Cederwall, γ -ray tracking in germanium: the backtracking method, Nucl. Instr. Meth. A 477 (2002) 391–396.
- [10] J. Gerl, W. Korten, AGATA technical proposal for an advanced gamma tracking array for the european gamma spectroscopy community, The AGATA collaboration (2001 [\[1\]](#)) 1–95.
URL <http://agata.pd.infn.it/documents/Agata-proposal.pdf>
- [11] T. Kröll, K. Vetter, D. Bazzacco, I. Y. Lee, Pulse shape analysis for γ -ray tracking applying a genetic algorithm, Tech. rep., lbl (2000 [\[1\]](#)).
URL <http://greta.lbl.gov/>

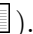




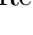


- [12] K. Vetter, A. L. Kuhn, M. A. Deleplanque, I. Y. Lee, F. S. Stephens, G. J. Schmid, D. Beckedahl, J. J. Blair, R. M. Clark, M. Cromaz, R. M. Diamond, P. Fallon, G. J. Lane, J. E. Kammeraad, A. O. Macchiavelli, C. E. Svensson, Three-dimensional position sensitivity in two-dimensionally segmented HP-Ge detectors, *Nucl. Instr. Meth. A* 452 (2000 ) 223–238.
- [13] K. Hauschild, A. Korichi, A. Lopez-Martens, J. Roccas, Simulations of the experimental set-up for the characterisation of AGATA prototype detectors, Tech. rep., Centre de Spectrométrie Nucléaire et de Spectrométrie de Masse (C.S.N.S.M.), University of Orsay, Paris (2004 ).
URL <http://www-csnsn.in2p3.fr>
- [14] A. Boston, Agata coincidence measurements and initial comparison with MGS, MGS workshop (April 2005 ).
URL <http://mgs2005.in2p3.fr/>
- [15] N. Saito, AGATA detector characterization: Quick 3D scanning system, MGS workshop (April 2005 ).
URL <http://mgs2005.in2p3.fr/>
- [16] J. Eberth, G. Pascovici, H. G. Thomas, N. Warr, D. Weißhaar, D. Habs, P. Reiter, P. Thierolf, D. Schwalm, C. Gund, H. Scheit, M. Lauer, P. Van Duppen, S. Franchoo, M. Huyse, R. M. Lieder, W. Gast, J. Gerl, K. P. Lieb, the MINIBALL COLLABORATION, MINIBALL: A Ge detector array for radioactive ion beam facilities, *Progr. Part. Nucl. Phys.* 46 (2001 ) 389–398.
- [17] N. Warr, J. Eberth, G. Pascovici, H. G. Thomas, D. Weißhaar, the MINIBALL Collaboration, MINIBALL: the first gamma-ray spectrometer using segmented, encapsulated germanium detectors for studies with radioactive beams, *Eur. Phys. J. A* 20 (2004 ) 65–66.
- [18] PT100 resistance table ().
URL <http://www.uss.no/apps/PT100A.pdf>
- [19] H. G. Thomas, Entwicklung eines Germanium-CLUSTER-Detektors für das Gamma-Spektrometer EUROBALL, Ph.D. thesis, Institut für Kernphysik, Köln (1995).
- [20] D. Weißhaar, MINIBALL: Ein neuartiges Gamma-Spektrometer mit ortsauflösenden Germaniumdetektoren, Ph.D. thesis, Institut für Kernphysik, Köln (2002 .
- [21] P. W. Nicholson, *Nuclear Electronics*, John Wiley and Sons, 1974.
- [22] F. Manfredi, *Selected Topics in Nuclear Electronics*, International Atomic Energy Agency (IAEA), Vienna, Austria (1986).




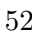

- [23] L. P. Gámir, A new method for the determination of the entry position of γ -rays in HPGe detectors by current pulse analysis, Ph.D. thesis, Max-Planck-Institut für Kernphysik, Heidelberg (1997 ).
URL <http://www.mpi-hd.mpg.de/cb/theses.html>
- [24] X-Ray Instrumentation Associates, 8450 Central Ave Newark, CA 94560 USA, User's manual digital gamma finder (DGF), 3rd Edition (July 2003 ).
URL <http://www.xia.com>
- [25] W. Shockley, Currents to conductors induced by a moving point charge, J. Appl. Phys. 9 (10) (1938 ) 635–636.
- [26] S. Ramo, Currents induced by electron motion, Proc. IRE 27 (1939) 584.
- [27] C. K. Jen, On the induced current and energy balance in electronics, Proc. IRE (1941) 345.
- [28] Z. He, Review of the Shockley-Ramo theorem and its application in semiconductor gamma-ray detectors, Nucl. Instr. Meth. A 463 (2001 ) 250–267.
- [29] E. Vittone, F. Fizzottia, A. Lo Giudicea, C. Paolinia, C. Manfredottia, Theory of ion beam induced charge collection in detectors based on the extended Shockley-Ramo theorem, Nucl. Instr. Meth. B 161-163 (2000 ) 446–451.
- [30] C. Lu, K. T. McDonald, The charge distribution on the cathode of a straw tube chamber, ArXiv High Energy Physics – e-prints (2000 ) 1–6.
URL <http://arxiv.org/abs/hep-ex/0009006>
- [31] G. F. Knoll, Radiation Detection and Measurement, 3rd Edition, John Wiley & Sons, New York, 1999.
- [32] R. A. Serway, Physics for scientists and engineers, 4th Edition, Saunders College Publishing, 1996.
- [33] J. D. Jackson, Classical Electrodynamics, 2nd Edition, John Wiley & Sons, New York, 1975.
- [34] G. Cavalleri, G. Fabri, E. Gatti, V. Svelto, On the induced charge in semiconductor detectors, Nucl. Instr. Meth. 21 (1963) 177–178.
- [35] G. Cavalleri, E. Gatti, G. Fabri, V. Svelto, Extension of Ramo's theorem as applied to induced charge in semiconductor detectors, Nucl. Instr. Meth. 92 (1971) 137–140.




- [36] J. Ljungvall, J. Nyberg, A study of fast neutron interactions in high-purity germanium detectors, *Nucl. Instr. Meth. A* 546 (2005) 553–573.
- [37] M. Descovich, I. Y. Lee, P. N. Luke, R. M. Clark, M. Cromaz, M. A. Deleplanque, R. M. Diamond, P. Fallon, A. O. Macchiavelli, E. Rodriguez-Vieitez, F. S. Stephens, D. Ward, Effects of neutron damage on the performance of large volume segmented germanium detectors, *Nucl. Instr. Meth. A* 545 (2005) 199–209.
- [38] E. Gatti, A. Geraci, G. Casati, S. Riboldi, G. Ripamonti, Spatial localization of multiple simultaneous hits in segmented HPGe detectors: a new algorithm, *Nucl. Instr. Meth. A* 458 (2001) 738–744.
- [39] B. Sernelius, Laplace’s and poisson’s equations (2006).
URL <http://www.ifm.liu.se/~boser/elma/Lect4.pdf>
- [40] E. Gatti, G. Padovini, Signal evaluation in multielectrode radiation detectors by means of a time dependent weighting vector, *Nucl. Instr. Meth.* 193 (1982) 651–653.
- [41] J. Blair, D. Beckedahl, J. Kammeraad, G. Schmid, Spatial resolution attainable in germanium detectors by pulse shape analysis, *Nucl. Instr. Meth. A* 422 (1999) 331–336.
- [42] J. M. Miller, Dependence of the input impedance of a three-electrode vacuum tube upon the load in the plate circuit, *Scientific Papers of the Bureau of Standards* 15 (351) (1920) 367–385.
URL <http://www.mit.edu/~klund/papers/jmiller.pdf>
- [43] Wikipedia: The laplace transform.
URL http://en.wikipedia.org/wiki/Laplace_transform
- [44] M. Abramowitz, I. A. Stegun, *Handbook of Mathematical Functions*, National Bureau of Standards, 1972.
URL <http://www.convertit.com/Go/ConvertIt/Reference/>
- [45] D. Weißhaar, Status report detector team, The Agata Week (February 2005).
URL http://npg.dl.ac.uk/AGATA/agata_week_talks/
- [46] N. Warr et al., private communications.
- [47] K. Vetter, A. Kuhn, I. Y. Lee, R. M. Clark, M. Cromaz, M. A. Deleplanque, R. M. Diamond, P. Fallon, G. J. Lane, A. O. Macchiavelli, M. R. Maier, F. S. Stephens, C. E. Svensson, H. Yaver, Performance of the GRETA prototype detectors, *Nucl. Instr. Meth. A* 452 (2000) 105–114.

- [48] T. Kröll, D. Bazzacco, K. Vetter, I. Y. Lee, Pulse shape analysis for the γ -ray tracking array MARS, Tech. rep., LNL Annual Report, Laboratori Nazionali di Legnaro, Padova (1999 ).
URL <http://www.lnl.infn.it/~annrep/>
- [49] A. Pullia, Test of a new low-noise preamplifier with the MARS segmented detector and extraction of physical data from the noise measurements, AGATA EDAQ meeting, Padova (September 2002 ).
URL <http://www.nsg.tsl.uu.se/agata/padova-sep2002/>
- [50] A. Pullia, AGATA preamplifiers: status and hints to improve their performance, AGATA week November 2005 (November 2005 ).
URL http://ireswww.in2p3.fr/ires/workshops/agata_week/
- [51] W. H. Press, S. A. Teukolsky, W. T. Vetterling, B. P. Flannery, Numerical Recipes in C, Cambridge University Press, 1995.
URL <http://www.library.cornell.edu/nr/bookcpdf.html>
- [52] Simion 7.0.
URL <http://www.simion.com>
- [53] L. Mihailescu, Principles and methods for γ -ray tracking with large volume germanium detectors, Ph.D. thesis, Bonn (2000).
URL <http://www.fz-juelich.de/ikp/kernspektroskopie/>
- [54] N. W. Ashcroft, N. D. Mermin, Solid State Physics, Holt and Rinehart and Winston, 1976.
- [55] HPGe detector manufacturing.
URL http://www.ortec-online.com/detectors/photon/a1_1.htm
- [56] W. Sasaki, M. Shibuya, Experimental evidence of the anisotropy of hot electrons in n-type germanium, J. Phys. Soc. Jpn. 11 (1956 ) 1202–1203.
URL <http://jpsj.ipap.jp/link?JPSJ/11/1202/>
- [57] T. S. Moss, Band Theory and Transport Properties, Vol. 1 of Handbook on Semiconductors, North-Holland Publishing Company, 1982.
- [58] L. Mihailescu, W. Gast, R. M. Lieder, H. Brands, H. Jäger, The influence of anisotropic electron drift velocity on the signal shapes of closed-end HPGe detectors, Nucl. Instr. Meth. A 447 (2000 ) 350–360.
- [59] G. Ottaviani, C. Canali, A. Alberigi Quaranta, Charge carrier transport properties of semiconductor materials suitable for nuclear radiation detectors, IEEE Trans. Nucl. Sci. NS-22 (1975) 192–204.

- [60] L. Reggiani, C. Canali, F. Nava, G. Ottaviani, Hole drift velocity in germanium, *Phys. Rev. B* 16 (6) (1977) 2781–2791.
- [61] M. I. Nathan, Anisotropy of the conductivity of n-type germanium at high electric fields, *Phys. Rev.* 130 (6) (1963) 2201–2204.
- [62] E. M. Conwell, High field transport in semiconductors, Vol. 9 of *Solid State Physics*, Academic Press, 1967.
- [63] L. Reggiani, C. Canali, F. Nava, Y. K. Pozhela, M. Asche, S. Komiyama, T. Kurosawa, T. Masumi, K. Hess, G. J. Iafrate, E. Constant, *Hot-Electron Transport in Semiconductors*, Vol. 58 of *Topics in Applied Physics*, Springer-Verlag, 1985.
- [64] H. G. Reik, H. Risken, Drift velocity and anisotropy of hot electrons in n germanium, *Phys. Rev.* 126 (5) (1962) 1737–1746.
- [65] D. Schweitzer, K. Seeger, The anisotropy of conductivity of n-type germanium in strong D.C. fields, *Z. Phys.* 183 (1965) 207–216.
- [66] W. E. Pinson, R. Bray, Experimental determination of the energy distribution functions and analysis of the energy-loss mechanisms of hot carriers in p-type germanium, *Phys. Rev.* 136 (5A) (1964) 1449–1466.
- [67] E. D. Alba, V. V. Paranjape, Energy distribution of holes in electric fields, *Phys. Lett.* 11 (1) (1964) 12–13.
- [68] P. Spellucci, DONLP2 users guide, T.U. Darmstadt, Dep. of Mathematics, 64289 Darmstadt, Germany.
URL <http://plato.la.asu.edu/donlp2.html>
- [69] W. R. Leo, *Techniques for Nuclear and Particle Physics Experiments*, 2nd Edition, Springer-Verlag, 1994.
- [70] A. Kuhn, Effects of the anisotropy in charge carrier drift velocity on position sensitive germanium detectors, Master’s thesis, U.C. Berkeley (1999).
URL <http://greta.lbl.gov/>
- [71] C. Gund, Das sechsfach segmentierte MINIBALL Modul Simulation und Experiment, Ph.D. thesis, Max-Planck-Institut für Kernphysik, Heidelberg (2000 ).
URL <http://www.mpi-hd.mpg.de/cb/theses.html>
- [72] M. Lauer, Implementierung von Algorithmen zur Echtzeitpulsformanalyse von HPGe Detektorsignalen, Master’s thesis, Max-Planck-Institut für Kernphysik Heidelberg (2001).
URL <http://www.mpi-hd.mpg.de/cb/theses.html>

- [73] T. Steinhardt, First in-beam experiment with AGATA detectors, AGATA week November 2005 (November 2005 ).
URL http://ireswww.in2p3.fr/ires/workshops/agata_week/
- [74] T. Materna, private communications.
- [75] Detector Performance and Pulse Shape Analysis for the Advanced GAMMA Tracking Array.
URL <http://www.e12.physik.tu-muenchen.de/AGATA/>
- [76] B. Majorovits, H. V. Klapdor-Kleingrothaus, Digital pulseshape analysis by neural networks for the Heidelberg-Moscow-double-beta-decay-experiment, ArXiv High Energy Physics – e-prints (1999 ) 1–12.
URL <http://arxiv.org/abs/hep-ex/9911001>
- [77] B. A. Majorovits, High purity germanium detectors for the search of rare events: Background discrimination and future prospects with the GENIUS project, Ph.D. thesis, Rupertus Carola University of Heidelberg (2000 ).
URL <http://www.ub.uni-heidelberg.de/archiv/1411>
- [78] A. Kuhn, Advanced pulse-shape analysis and implementation of gamma-ray tracking in a position-sensitive coaxial HPGe detector, Ph.D. thesis, U.C. Berkeley (2002).
URL <http://greta.lbl.gov/>
- [79] T. Kröll, D. Bazzacco, R. Venturelli, P. Pavan, C. A. Ur, Pulse shape analysis by a genetic algorithm with the γ -ray tracking detector MARS, Tech. rep., LNL Annual Report, Laboratori Nazionali di Legnaro, Padova (2001 ).
URL <http://www.lnl.infn.it/~annrep/>
- [80] M. Schlarb, Particle swarms and pulse shape analysis, AGATA week November 2005 (November 2005 ).
URL http://ireswww.in2p3.fr/ires/workshops/agata_week/
- [81] R. Venturelli, D. Bazzacco, Adaptive grid search as pulse shape analysis algorithm for γ -tracking and results, Tech. rep., LNL Annual Report, Laboratori Nazionali di Legnaro, Padova (2004 ).
URL <http://www.lnl.infn.it/~annrep/>
- [82] T. Beck, Haar wavelet transformation, AGATA week November 2005 (November 2005 ).
URL http://ireswww.in2p3.fr/ires/workshops/agata_week/
- [83] A. Olariu, Status of the matrix method, AGATA week November 2005 (November 2005 ).
URL http://ireswww.in2p3.fr/ires/workshops/agata_week/

- [84] E. Cepeda, K. Vetter, A. Kuhn, I. Y. Lee, R. M. Clark, M. Cromaz, M. A. Deleplanque, R. M. Diamond, P. Fallon, G. J. Lane, A. O. Machiavelli, F. S. Stephens, C. E. Svensson, Signal decomposition for GRETA, Tech. rep., lbl (1999 ).
URL <http://greta.lbl.gov/>
- [85] C. Doll, H. G. Börner, T. von Egidy, H. Fujimoto, M. Jentschel, H. Lehmann, Gams5, J. Res. Natl. Inst. Stan. 105 (2000 ) 167–171.
URL <http://www.nist.gov/jres>
- [86] E. G. Kessler Jr., M. S. Dewey, R. D. Deslattes, A. Henins, H. G. Börner, M. Jentschel, C. Doll, H. Lehmann, The deuteron binding energy and the neutron mass, Phys. Lett. A 255 (1999 ) 221–229.
- [87] J. Jolie, Gamma ray spectroscopy with ultra-high precision, Europhysics News 30 (2) (1999 ) 52–55.
- [88] J. Jolie, T. Materna, C. Albrecht, D. M. Sanchez-Cano, M. Jentschel, G. Simpson, A. Linnemann, ILL research proposal 30423: Towards more efficient and accurate GAMS4/5 spectrometers.
- [89] Y. Cauchois, Spectrographie des rayons X par transmission d’un faisceau non canalisé à travers un cristal courbé, J. de Physique VIII 3 (1932) 512–515.
- [90] J. W. M. DuMond, A high resolving power, curved-crystal focussing spectrometer for short wave-length x-rays and gamma-rays., Rev. Sci. Instr. 18 (1947) 626.
- [91] R. D. Deslattes, High resolution γ -ray spectroscopy: the first 85 years, J. Res. Natl. Inst. Stan. 105 (2000 ) 1.
URL <http://www.nist.gov/jres>
- [92] Center for adaptive optics.
URL <http://cfao.ucolick.org/>
- [93] T. Materna, H. G. Börner, B. Bruyneel, M. Jentschel, J. Jolie, A. Linnemann, P. Mutti, G. Simpson, N. Warr, Corrective optics for diffraction of gamma-rays, will be submitted to NIM.
- [94] T. Materna, B. Bruyneel, J. Jolie, A. Linnemann, N. Warr, M. Jentschel, H. G. Börner, P. Mutti, G. Simpson, Corrective imaging for gamma-rays, Tech. rep., ILL annual report (2005).
URL http://www.ill.fr/index_ill.html
- [95] Wikipedia: The multivariate normal distribution.
URL http://en.wikipedia.org/wiki/Multivariate_normal

- [96] Mathworld: Vector direct product.
URL <http://mathworld.wolfram.com/VectorDirectProduct.html>
- [97] Mathworld: The autocorrelation.
URL <http://mathworld.wolfram.com/Autocorrelation.html>
- [98] Mathworld: The pseudoinverse.
URL <http://mathworld.wolfram.com/Pseudoinverse.html>
- [99] Mathworld: The moore-penrose matrix inverse.
URL <http://mathworld.wolfram.com/>
- [100] J. Fox, Time-series regression and generalized least squares, Appendix to An R and S-PLUS Companion to Applied Regression (2002  1–8.
URL <http://cran.r-project.org/>
- [101] Wikipedia: Efficiency (statistics).
URL [http://en.wikipedia.org/wiki/Efficiency_\(statistics\)](http://en.wikipedia.org/wiki/Efficiency_(statistics))
- [102] A. Görgen, Position sensitivity of the AGATA prototype crystal analyzed using a database of calculated pulse shapes (2003  1–56.
URL <http://www-dapnia.cea.fr/Sphn/Deformes/Agata/local/>
- [103] M. Scheffe, The Cramer-Rao Bound for Parallel MRI: Optimum SNR, Minimum Error, and the g-Function, Second International Workshop on Parallel MRI (October 2004 ).
URL <http://www.mr.ethz.ch/parallelmri04/program.html>

Thank you!

First of all, I would like to thank Prof. Dr. Peter Reiter for the chance he offered me to start this work, his unlimited support and for the valuable discussions and guidance.

A special thanks goes to Dr. Astrid Imig, Dr. Antonella Scherillo, Drd. Tom Morgan and Drd. Gabriela-Elena Ilie for the careful reading of the manuscript, valuable comments and corrections.

I'm indebted to Prof. Dr. Jan Jolie for lending the 12-fold detector, Dr. Dirk Weißhaar and Dr. Heinz-Georg Thomas for teaching me to handle such detectors and Dr. Thomas Materna for the fruitful collaboration in the analysis of the GAMS5 experiment.

Thanks to all the group members, for their support during the long period of measurements. The group members at present: Florian, Herbert, Astrid, Astrid, Marijke, Michael, Tanja and Andreas as well as those who have left the group to seek their fortune elsewhere: Sven, Melissa, Chris, Thomas and Stefan.

I also would like to express my gratitude to the workshops for the brilliant job they perform and this on a daily basis. Dr. Gheorghe Pascovici, from which I learned a lot about electronics, and the electronic workshop: Gerd Breuer, Christoph Görden, Guido Richardt, Albert Wedel and Jan Sydow. Mr. Stefan Thiel and the mechanical workshop: Detlef Schieweck, Pierre Kempf, Steffen Krüger, Alexander Repke, Thomas Rolke, Achim Arzdorf, Tobias Hancke, David Kobersky, Lisa Lindenthal, Vera Przewloka, Manuel Schnitzler, Stefan Weinreich and Sebastian Zimmermann. Also to the tandem crew: Lothar Steinert, Otto Rudolph and Uwe Werner.

Thanks to all the colleagues and friends at IKP, especially Barbara, Gabriela-Elena, Thomas, Antonella and Nele for the time we spent together during lunches and coffee breaks.

And finally, a big thanks to my mother and sister, for their love, patience and support.

